

# MEASUREMENT OF THE NEUTRON LIFETIME USING TRAPPED ULTRACOLD NEUTRONS

Nathan Callahan

Submitted to the faculty of the University Graduate School  
in partial fulfillment of the requirements

for the degree

Doctor of Philosophy

in the Department of Physics,

Indiana University

September 2018

ProQuest Number: 10935522

All rights reserved

INFORMATION TO ALL USERS

The quality of this reproduction is dependent upon the quality of the copy submitted.

In the unlikely event that the author did not send a complete manuscript and there are missing pages, these will be noted. Also, if material had to be removed, a note will indicate the deletion.



ProQuest 10935522

Published by ProQuest LLC (2018). Copyright of the Dissertation is held by the Author.

All rights reserved.

This work is protected against unauthorized copying under Title 17, United States Code  
Microform Edition © ProQuest LLC.

ProQuest LLC.  
789 East Eisenhower Parkway  
P.O. Box 1346  
Ann Arbor, MI 48106 – 1346

Accepted by the Graduate Faculty, Indiana University, in partial fulfillment of the requirements  
for the degree of Doctor of Philosophy.

Doctoral Committee

---

Chen-Yu Liu, Ph.D. (Chair)

---

Michael Snow, Ph.D.

---

Chuck Horowitz, Ph.D.

---

John Salzer, Ph.D.

August 6, 2018

Copyright © 2018

Nathan Callahan

I'd like to thank my Parents, my Brother, my Cousin, and my Grandmother for all the support they've given me over the years. Their assistance helped me through college and always made me feel encouraged. I would not be here without them.

I'd like to thank Dr. Landy and Mrs. Bailey (my high school physics teachers) and all my other instructors as well. Their expert teaching and enthusiasm caused me to become a physicist.

I'd like to thank my colleagues at the University of Toledo REU. Although our friendship was only one summer long, it was dearly treasured.

I'd like to thank my good friend Chris. Studying for the Qualifying exam and living in Los Alamos would not have gone as well without him.

Finally I'd like to thank my girlfriend and partner in life Jamie. Without her steadfast devotion, endless patience, and good nature I'm not sure I could have finished my degree.

## ACKNOWLEDGMENTS

I'd like to acknowledge the help and experience of my collaborators on  $UCN\tau$  who have been helpful over the years.

This material is based upon work supported by the U.S. Department of Energy, Office of Science, Office of Workforce Development for Teachers and Scientists, Office of Science Graduate Student Research (SCGSR) program. The SCGSR program is administered by the Oak Ridge Institute for Science and Education for the DOE under contract number DESC0014664.

I acknowledge the Indiana University Pervasive Technology Institute [1] for providing High-Performance Computing (Big Red II) and storage resources that have contributed to the research results reported within this work. URL: <https://pti.iu.edu/>

This research was supported in part by Lilly Endowment, Inc., through its support for the Indiana University Pervasive Technology Institute, and in part by the Indiana METACyt Initiative. The Indiana METACyt Initiative at IU was also supported in part by Lilly Endowment, Inc.

Nathan Callahan

# MEASUREMENT OF THE NEUTRON LIFETIME USING TRAPPED ULTRACOLD NEUTRONS

The neutron lifetime is of interest in cosmology and searches for beyond the Standard Model physics. Measurements in the past 2 decades have disagreed significantly. Measurements using trapped ultracold neutrons (UCN) have been recently re-analyzed with new assessments of systematic effects, moving the average by  $6\sigma$ . Additionally, a second type of lifetime experiment measuring decay-in-flight protons in a cold neutron beam disagrees with bottle measurements by  $4\sigma$ . This tension motivates UCN $\tau$ , a bottle lifetime experiment that is not susceptible to the large corrections of previous bottle experiments. UCN $\tau$  uses a magnetic field from a Halbach array to levitate UCN of energy  $< 50$  neV. These neutrons are counted using a prompt *in situ* detector which is capable of gathering spectral information. In this work, analysis of a 0.7 s statistical uncertainty dataset is presented. The effects of pileup, deadtime, and backgrounds were investigated. Limits are placed on shifts due to depolarization during holding, position-dependent backgrounds, phase space evolution, and deadtime. A Monte Carlo model is developed which reproduces the short holding time dataset. This simulation uses 5 parameters to describe the spectrum of UCN in the experiment and the detector. The model is used to estimate the size of shifts due to uncleaned UCN and UCN heated by microphonic vibrations. Additionally, novel superconducting trap geometries are studied via Lyapunov exponents. A trap which is almost completely chaotic is sought, which has guaranteed cleaning behavior due to the ergodic nature of chaotic orbits. Using these methods, UCN $\tau$  has made a measurement of  $\tau_n=877.9 \pm 0.68 \text{ s(stat.)} \pm 0.3 \text{ s(sys.)}$ .

---

Chen-Yu Liu, Ph.D. (Chair)

---

Michael Snow, Ph.D.

---

Chuck Horowitz, Ph.D.

---

John Salzer, Ph.D.



# CONTENTS

<b>I</b>	<b>Introduction</b>	<b>1</b>
<b>1</b>	<b>The Neutron, Big Bang Nucleosynthesis, and the Standard Model</b>	<b>1</b>
1.1	About the Neutron . . . . .	1
1.2	History of the Neutron and its Lifetime . . . . .	1
1.3	Bottle Measurements . . . . .	3
1.4	Beam Measurements . . . . .	5
1.5	Magnetic Bottles . . . . .	6
1.6	$\tau_n$ and The Primordial Helium Abundance . . . . .	7
1.7	The Standard Model and Neutron $\beta$ Decay . . . . .	8
<b>2</b>	<b>UCN interactions</b>	<b>10</b>
2.1	UCN Overview . . . . .	10
2.2	UCN Interaction with Matter . . . . .	11
2.3	UCN Interaction with Magnetic Fields . . . . .	12
<b>II</b>	<b>Ultracold Neutrons</b>	<b>10</b>
<b>3</b>	<b>Sources of UCN</b>	<b>14</b>
3.1	Sources of UCN . . . . .	14
3.2	Los Alamos Neutron Science Center UCN Source . . . . .	15
<b>4</b>	<b>Hardware Overview</b>	<b>17</b>
<b>III</b>	<b>Hardware</b>	<b>17</b>
<b>5</b>	<b>Trapdoor</b>	<b>21</b>

5.1	Trapdoor Actuator System . . . . .	21
5.2	Trapdoor Software . . . . .	24
<b>6</b>	<b>Giant Cleaner</b>	<b>27</b>
<b>7</b>	<b>Overview of UCN<math>\tau</math> Analysis</b>	<b>30</b>
7.1	Systematic Effect Analysis . . . . .	30
7.2	Miscellaneous Tasks . . . . .	31
<b>IV</b>	<b>Analysis</b>	<b>30</b>
<b>8</b>	<b>UCN event reconstruction</b>	<b>32</b>
8.1	ZnS:Ag Scintillator . . . . .	32
8.2	Coincidence Identification . . . . .	33
8.3	Backgrounds . . . . .	35
8.4	Deadtime . . . . .	38
8.5	Rate Dependent Effects in Coincidence Analysis . . . . .	40
8.5.1	Rate Dependent Effect Simulation . . . . .	40
8.5.2	Rate Dependent Effect Simplification . . . . .	44
8.5.3	Identification of Optimal Cuts . . . . .	45
8.5.4	Investigation of Deadtime Effects . . . . .	46
<b>9</b>	<b>Normalization</b>	<b>49</b>
9.1	Introduction . . . . .	49
9.2	Description of Detectors . . . . .	49
9.3	Run Filtering . . . . .	50
9.4	Run Pairing . . . . .	53
9.5	Exponential Weighting . . . . .	54

9.6	Spectral Evolution . . . . .	55
9.7	Spectral Correction . . . . .	55
9.8	Source Parameters . . . . .	56
<b>10</b>	<b>Lifetime Calculation</b>	<b>65</b>
10.1	Exponential Decay . . . . .	65
10.2	Optimization of Holding Times . . . . .	67
10.3	Statistical Bias . . . . .	69
10.4	Final Calculation . . . . .	71
10.5	Results . . . . .	72
<b>11</b>	<b>Systematic Corrections</b>	<b>74</b>
11.1	Heated UCN Uncertainty Estimate and Uncleaned UCN Uncertainty Estimate . .	74
11.2	Discriminator Deadtime Uncertainty . . . . .	74
11.3	Spectral Correction . . . . .	75
11.4	Depolarization . . . . .	76
11.5	Phase Space Evolution Uncertainty . . . . .	78
11.6	Position Dependent Background . . . . .	80
11.7	Summary . . . . .	81
<b>12</b>	<b>UCN<math>\tau</math> Optimization</b>	<b>82</b>
12.1	Spin Flipper Tuning . . . . .	82
12.2	Filling Time Scan . . . . .	83
12.3	Detection Time Constant . . . . .	84
12.4	Cleaning Time Constant . . . . .	85
12.5	Phase Space Evolution . . . . .	86
12.6	Peak 1 Counting Time Constant . . . . .	87

<b>13 Overview of UCN<math>\tau</math> Simulations</b>	<b>90</b>
<b>V Simulations</b>	<b>90</b>
<b>14 Toy Models of the UCN<math>\tau</math> Trap</b>	<b>92</b>
14.1 Markov Chain Model of Heating . . . . .	92
14.2 Phase Space Evolution . . . . .	94
<b>15 UCN<math>\tau</math> Magnetic Field Expansion</b>	<b>96</b>
<b>16 Symplectic Integration</b>	<b>99</b>
16.1 Symplectic Integration Scheme . . . . .	99
16.2 Test of Symplectic Integrator on Field Expansion . . . . .	100
16.3 Convergence Studies . . . . .	100
<b>17 Simulation of 9-Step Data</b>	<b>105</b>
17.1 Simulation Schematic . . . . .	105
17.2 Detector Setup . . . . .	105
17.3 Spectrum Setup . . . . .	108
17.4 $\chi^2$ Comparison of Histograms . . . . .	109
<b>18 Simulation of Heating and Cleaning Effect on <math>\tau</math></b>	<b>114</b>
18.1 Lifetime Measurement Setup . . . . .	114
18.2 Heating Model . . . . .	115
18.3 Cleaning and Heating Results . . . . .	116
18.4 Heated UCN Detection Efficiency . . . . .	118
18.5 Arrival Location of UCN on Cleaner and Dagger . . . . .	121
<b>19 Simulation of Phase Space Evolution</b>	<b>125</b>

19.1 Phase Space Evolution Data . . . . .	125
19.2 Phase Space Evolution in Lifetime Data . . . . .	126
19.3 Counting Time Constant . . . . .	127
<b>20 Lyapunov Exponents</b>	<b>131</b>
20.1 Lyapunov Exponents . . . . .	131
20.2 Lyapunov Results . . . . .	132
<b>21 Superconducting UCN traps</b>	<b>136</b>
21.1 Superconducting Trap Geometry . . . . .	136
21.2 Superconducting Trap Results . . . . .	138
<b>VI Conclusion</b>	<b>142</b>
<b>22 Conclusion</b>	<b>142</b>
22.1 Summary of Methods and Results . . . . .	142
22.2 Implications of UCN $\tau$ Results for Precision $\beta$ Decay Measurements . . . . .	144
<b>BIBLIOGRAPHY</b>	<b>147</b>
<b>APPENDICES</b>	<b>153</b>
<b>A Uncleaned and Heated UCN Extrapolation</b>	<b>154</b>
A.1 Uncleaned UCN Correction . . . . .	154
A.2 Uncleaned UCN Uncertainty Estimate . . . . .	156
A.3 Heated UCN Uncertainty Estimate . . . . .	158
<b>Curriculum Vitae</b>	

## CHAPTER 1

# THE NEUTRON, BIG BANG NUCLEOSYNTHESIS, AND THE STANDARD MODEL

### 1.1 ABOUT THE NEUTRON

The neutron and its decay is a simple but powerful laboratory to study many scales of physics from the particle physics to cosmology. Neutron  $\beta$  decay gives access to two important parameters in the Standard Model:  $V_{ud}$  (which describes quark mixing via the CabibboKobayashiMaskawa matrix) and  $\lambda$  (or  $g_A/g_V$ ;  $g_V = 1$ , the zero-momentum axial vector form factor over the vector form factor which describes the interior of the neutron). Studying the neutron lifetime and decay correlations allows measurements of these parameters and verification of the Standard Model. These parameters can also be used to predict the primordial helium abundance after the Big Bang.

### 1.2 HISTORY OF THE NEUTRON AND ITS LIFETIME

The neutron was discovered by Chadwick in 1932 [2]. Chadwick discovered that a new type of highly penetrating radiation (neutrons) were produced in certain nuclear reactions. Initially, it was thought that the neutron could be a bound state of a proton and an electron. However, Chadwick further determined that the neutron mass was greater than the proton mass, which opened the possibility for it to decay. The first observation of the neutron lifetime was by Snell *et. al.* in 1948 [3] by observing proton decay-in-flight in a neutron beam. They measured  $\tau_n \sim 1800$  s (about 1000s too long). This began a long tradition of continually more precise  $\tau_n$  measurements.

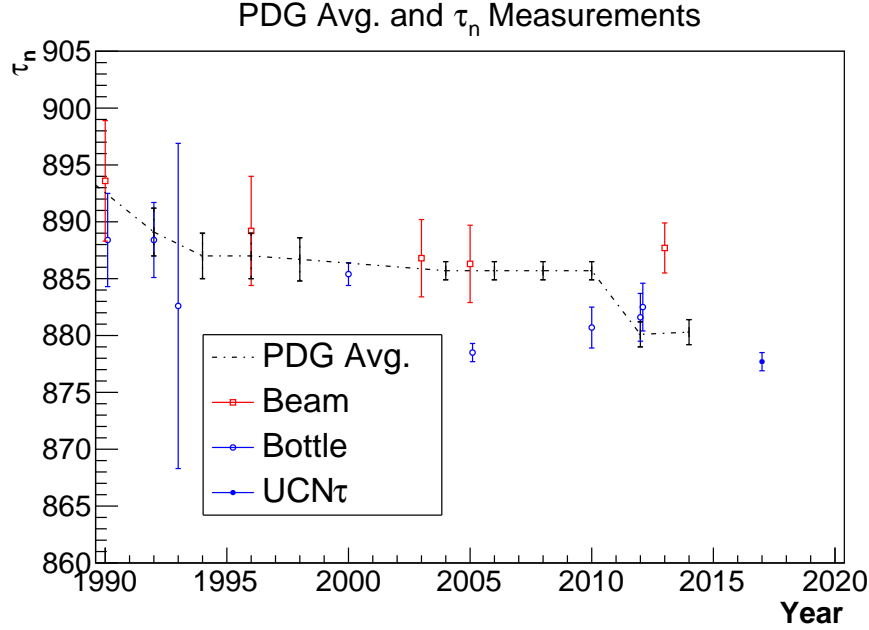


Figure 1.1: Lifetime Measurements through the ages.

Historically, two major methods have been used to measure the neutron lifetime, colloquially known as beam methods and bottle methods. Figure 1.1 shows the history of neutron lifetime measurements by year from 1990. Historically, the earlier measurements have tended towards higher lifetimes and have, through the years, gradually decreased.

There have been several significant changes in the average value calculated by the Particle Data Group (PDG). The most recent was a shift from  $\tau_n = 885.7 \pm 0.8$  s to  $880.1 \pm 0.1$  s between 2010 and 2012 (approximately  $6\sigma$ ) due to reassessment of the large corrections in bottle measurements [4].

The modern disagreement between beam ( $888.0 \pm 2$  s) and bottle ( $878.1 \pm 0.5$  s) measurements is  $4.4\sigma$ . The bottle measurements (weighted sum of bottle measurements used in the PDG value along with the measurement presented here) are on average lower than beam experiments (Yue’s and Byrne’s), which is the direction expected if there were unaccounted for loss mechanisms in bottle lifetime measurements.

The two different classes of experiments are also fundamentally different. Bottle experiments are disappearance experiments, where the deficit of neutrons is measured after storing samples for

differing time intervals. Beam experiments measure the appearance of protons in the beam, and are therefore only sensitive to the branching ratio to protons. In principle, a consistent and well-measured difference between the two experiment types could point to either a missing systematic effect, or new physics. The goal of this work is to study a bottle-type experiment and assess the systematic effects present.

### 1.3 BOTTLE MEASUREMENTS

Historically, bottle measurements were made using material bottles, where ultracold neutrons (UCN) are stored in a bottle and contained by interacting with the walls via the strong force [5]. The potential is on the order of 100 neV, so neutrons with low enough energy can live in the bottle for long periods of time. With careful bottle construction, the loss lifetime on the walls can exceed the  $\beta$  decay lifetime. However, the loss is energy and temperature dependent, leading to corrections to the measured trap lifetime.

A prototypical bottle experiment is given in Serebrov *et. al.* [5]. UCN are loaded into a trap via a neutron guide. The trap is rotated so that neutrons can enter via the open top. After saturation density is reached in the trap, the trap is rotated so that its open top is higher than the bottom and UCN can be trapped by the walls and gravity. High-energy UCN are allowed to escape and the UCN are then stored for varying holding times. The trap can be again rotated to be emptied into a detector below the trap that is obscured initially by a valve.

The lifetime in the trap can be measured using the ratio of UCN at 2 different holding times:  $\tau = \Delta t / \log(N_s/N_l)$  where  $\Delta t$  is the time difference between 2 population measurements,  $N_s$  is the number of UCN counted after a short holding time, and  $N_l$  is the number of UCN counted after a long holding time. A distinction is made between  $\tau$  and  $\tau_n$ . The former is the trap lifetime  $\tau^{-1} = \tau_n^{-1} + \tau_{\text{loss}}^{-1}$  and the latter is the free neutron lifetime. If the source is sufficiently stable, the ratio will cancel out the efficiency of counting and initial population sizes making bottle experiments relative measurements. Deviations in the flux of the neutron source can be accounted



Author	$\sigma_{\text{stat.}}$ [s]	$\Delta\tau_{\text{sys.}}$ [s]	Extrapolation [s]	Method
Arzumanov 2015 [6]	0.64	3.6	40-280	Bottle
Steyerl 2012 [7]	1.4	$\sim 7$	$>200$ s	Bottle
Pichlmaier 2010 [8]	1.3	1	110-300	Bottle
Serebrov 2005 [5]	0.7	0.4	10-20	Bottle
Yue 2013 [9]	1.2	1	2-15	Beam
Byrne 1996 [10]	3	5.9	-	Beam

Table 1.1: A selection of neutron Lifetime experiments with systematic corrections and approximate extrapolation scales

for by normalizing to the flux for  $N_s$  and  $N_l$ .

A key feature of material bottle traps is the ability to vary the collision rate,  $\gamma$ . The neutron lifetime can be measured by measuring the trap lifetime as a function of  $\gamma$  and extrapolating to zero collision rate. The Serebrov experiment used different sized traps as well as spectral preparation to vary the collision rate. By inserting a different trap geometry, the surface area to volume ratio is changed and therefore the total collision rate of UCN. Additionally, UCN are emptied from the top of the vessel by rotation. This allows spectral information to be extracted from the counts, so  $\tau$  can also be measured at different UCN energies. The final value of  $\tau_n$  is the extrapolation (whether via geometry or spectrum or both) to zero collision rate.

The trap lifetimes measured in the Serebrov experiment were between  $\sim 874$ - $863$  s, meaning an extrapolation of  $\sim 10$ s from the mean trap lifetime. Historically, this is a small correction; some bottle experiments had extrapolations higher by an order of magnitude. The extrapolation size and systematic corrections for the collection of  $\tau_n$  results appearing in the PDG can be found in Table 1.1. These are rough estimates of the sizes based on reported numbers.

The dominating systematic uncertainty is the extrapolation down to zero collision rate using calculated values of  $\gamma$  for the 2 traps.  $\gamma$  was calculated by assuming a spatial density and energy spectrum in the trap and integrating the flux onto the walls [11]. The uncertainty in the ex-

trapolation was estimated via simulations by doing the extrapolation on similar geometries to the experiment and measuring the ability of the extrapolation to reproduce the Monte Carlo lifetime  $\tau_{n,\text{MC}}$ . Their estimate for the accuracy of the extrapolation was 0.236 s. Additionally, the loss probability per bounce is energy dependent, which contributes about half as much uncertainty.

## 1.4 BEAM MEASUREMENTS

Beam measurements use neutron beams to measure  $\tau_n$ . A prototypical beam experiment is given in Nico *et. al.* [12]. In this experiment, a cold neutron beam passes through a proton trap. Some fraction of cold neutrons decay in flight into protons and are trapped. The neutron beam then passes through a flux monitor which measures the total number of neutrons per unit time. After a collection period, protons are allowed to exit the trap and are accelerated into a proton detector where they are counted. By comparing the proton detection rate to the neutron rate, the lifetime is obtained via  $\tau_n \sim \frac{\dot{N}_n}{\dot{N}_p}$ .

One problematic element of the experiment is that the edge of the trap is not well defined. To avoid this problem, the trap is made of several segments. By doing the experiment with differing number of segments, the proton rate as a function of trap length can be calculated instead. The change in trap length is then measured instead of the fiducial volume of the trap itself.

The quantities measured are also absolute: one needs to measure the neutrons with a known efficiency and the protons with a known efficiency. Large systematic uncertainties can come from calibration of the neutron and proton detectors. The initial measurements by Nico *et. al.* (refined in Yue [9]) had corrections of several seconds in positive and negative directions and a systematic uncertainty of 2.7 s due to the effects of beam shape on the neutron detector and the composition of the detector. An extrapolation of 2-15 s also has to be made for backscattering on the proton detector [12].

## 1.5 MAGNETIC BOTTLES

Magnetic bottles were initially proposed by Vladimiskii [13]. UCN also interact with magnetic fields and if their spin is properly aligned, will be repelled by high fields (so-called "Low Field Seekers"). Due to their low energy, UCN can adiabatically follow magnetic fields and maintain their polarization in the local field direction. Additionally, a neutron gains roughly one neV of energy per cm in Earth's gravitational field, allowing low-energy UCN to be totally confined inside a magnetic trap. Magnetic bottles allow neutrons to be stored without material losses, eliminating the need for extrapolation to zero collision rate.

The use of magnetic fields to trap UCN eliminates the wall loss, but also typically adds other systematic effects that need to be studied carefully. In magnetic bottles, it is possible for the UCN to depolarize during storage. A depolarized UCN will be lost into the magnetic walls as it is attracted to high fields. Typically, magnetic bottles are open on top; high-energy UCN can escape if not eliminated before storage. Elimination of high-energy UCN is difficult because wall reflections do not scatter diffusely into phase space unlike material bottles where there are substantial diffuse reflections. This causes slow equilibration in phase space and therefore slow removal of high-energy UCN. Finally, if UCN gain any energy during storage they can also leave the trap, lowering the lifetime.

A magnetic bottle experiment has already been conducted [14]. This experiment used cylindrically symmetric trap where neutrons were loaded from above via a cylindrical lift that eliminated untrappable neutrons during the filling procedure. The lift adiabatically lowers a neutron population into the trap for storage. This experiment measured  $\tau_n = 878.3 \text{ s} \pm 1.6 \text{ s (stat.)} \pm 1.0 \text{ s (sys.)}$ , in good agreement with previous bottle experiments. This experiment needed a correction of 3.7 s in order to correct for losses incurred due to spin flips during storage.

## 1.6 $\tau_n$ AND THE PRIMORDIAL HELIUM ABUNDANCE

The aim of Big Bang Nucleosynthesis theory (BBN) is to predict the conditions of the early universe using the Standard Model and statistical mechanics. BBN theory can predict the primordial helium abundance,  $Y_p$ .  $Y_p$  can be predicted in BBN theory as well as measured experimentally [15]. The neutron lifetime,  $\tau_n$  is used several places in the standard BBN model and the uncertainty in the  $Y_p$  prediction is dominated by the uncertainty in  $\tau_n$ . A sketch of the BBN theory is reproduced below to show schematically where  $\tau_n$  is important and how its uncertainty affects  $Y_p$ .

The beginning of the universe was hot and dense. Eventually, protons and neutrons formed out of the primordial soup. Their numbers were kept in equilibrium by several nuclear reactions ( $n + e^+ \leftrightarrow p + \bar{\nu}_e$ ,  $n + \nu_e \leftrightarrow p + e^-$ ,  $n \rightarrow p + e^- + \bar{\nu}_e$ ). The latter is neutron  $\beta$  decay and has a cross-section  $\propto 1/\tau_n$ . The other reactions are also proportional to  $1/\tau_n$ . Eventually, the universe will reach a temperature where the rate of the first 2 interactions will fall to a point where only one interaction is expected in the momentary age of the universe. This is the freezeout temperature, given in terms of the effective number of neutrino degrees of freedom,  $N_b$ , and the neutron lifetime  $\tau_n$  by [15]

$$T_f \propto (22 + 7N_b)^{1/6} \tau_n^{1/3}. \quad (1.1)$$

Neutrons and protons were, until this temperature is reached, in equilibrium. However, after this period the ratio of neutrons to protons is frozen, and only the last reaction (neutron decay) plays an important role. Initially after  $T_f$  is reached, the universe is too hot to form nuclei so the neutrons present will  $\beta$  decay freely. Eventually after a time  $t_d$ , nuclei are able to form and almost all neutrons are trapped in helium-4 atoms where they are stable. This gives the primordial helium abundance as

$$Y_p \sim \frac{2e^{-t_d/\tau_n}}{1 + e^{\Delta m/kT_f}}, \quad (1.2)$$

where  $t_d$  is the time where neutrons can freely decay before capture,  $\Delta m$  is the mass difference between the free neutron and free proton, and  $k$  is the Boltzmann constant.

This quick calculation gives  $Y_p \sim 0.22$  which compares to  $Y_p = 0.24709 \pm 0.00017$  in state-of-the-art calculations by Pitrou *et. al.* [16].

The sensitivity of  $Y_p$  to the neutron lifetime is found to be  $\sim +0.72\Delta\tau_n/\tau_n$  [17]. If the neutron lifetime were to shift by  $\sim 1\%$ , it would shift the prediction of  $Y_p$  by  $5\sigma$ . The beam-bottle discrepancy stands at roughly  $1\%$ , so making accurate predictions of  $Y_p$  needs accurate measurements of  $\tau_n$ .

Observational studies of  $Y_p$  can be made by extrapolating the helium abundance in low-metallicity H II regions down to zero metallicity [18]. H II regions are diffuse matter largely composed of hydrogen. Pitrou *et. al.* adopt a value of  $Y_p = 0.2449 \pm 0.0040$  [16] based on a regression of 16 objects including infrared lines [19]. If the beam lifetime is used in the results from Pitrou *et. al.* (via the  $\sim +0.72\Delta\tau_n/\tau_n$  sensitivity), the predicted  $Y_p$  is approximately  $1\sigma$  away from the observational abundances.

## 1.7 THE STANDARD MODEL AND NEUTRON $\beta$ DECAY

The free neutron in the Standard Model is subject to  $\beta$  decay via the weak force. Including the effects of radiative corrections,  $\tau_n$  is given by [20]

$$\tau_n = \frac{4908.7(1.9)}{|V_{ud}|^2(1 + 3g_A^2)}, \quad (1.3)$$

which involves the CKM matrix element  $V_{ud}$ , and the zero-momentum axial vector form factor  $g_A$ . The CKM matrix describes quark flavor mixing in the Standard Model.

Measuring  $V_{ud}$  is then possible by measuring both  $\tau_n$  and  $g_A$ . The latter can come from other  $\beta$  decay observables, for example  $A$ , the correlation between the neutron spin and electron momentum.  $V_{ud}$  is of interest in searches of physics beyond the Standard Model (BSM); combined with  $V_{us}$  and  $V_{ub}$  it measures unitarity of the CKM matrix

$$\Delta_{\text{CKM}} = |V_{ud}|^2 + |V_{us}|^2 + |V_{ub}|^2 - 1, \quad (1.4)$$

which is 0 in the Standard Model.  $\Delta_{\text{CKM}}$  is sensitive to BSM left and right-handed couplings [21], which can be seen in the effective field theory value for  $V_{ud}$  when considering free neutron decay:

$$|\bar{V}_{ud}|^2|_{n \rightarrow pe\bar{\nu}} = |V_{ud}|^2 \left[ 1 + 2\text{Re}(\epsilon_L + \epsilon_R - \epsilon_\mu) + \frac{1}{1 + 3\lambda^2} \left( g_S \text{Re} \epsilon_S - 12\lambda g_T \text{Re} \epsilon_T \right) \times \left( \frac{I_1(x_0)}{I_0(x_0)} - \frac{6\lambda^2}{1 + 3\lambda^2} c \right) \right], \quad (1.5)$$

where  $\epsilon_\alpha$  is the effective coupling beyond the standard model for  $\alpha = L, R, S, P, T$  for left-handed, right-handed, scalar, pseudo-scalar, and tensor interactions. Similarly,  $g_\alpha$  for  $\alpha = S, P, T, V, A$  is the zero-momentum form factor for the previously enumerated, vector, or axial vector interactions.  $I_0(x_0)$  and  $I_1(x_0)$  are phase space integrals. The constant  $c$  depends on how  $\lambda$  ( $= g_A/g_V$ ) is extracted (for example via  $A$ ).

Current precision determinations of  $\Delta_{\text{CKM}}$  constrain new physics at around 11 TeV energy scale. Low-energy searches for  $\epsilon_L + \epsilon_R + \epsilon_\mu$  are competitive with high-energy searches for this signal.

Measurements of  $V_{ud}$  using  $\tau_n$  and  $\lambda$  are currently not as precise as  $0^+ \rightarrow 0^+$  nuclear  $\beta$  decay measurements [22]. However, both are subject to similar radiative corrections as in Equation 1.3. Additionally, extraction of  $V_{ud}$  from superallowed  $\beta$  decay experiments are subject to nuclear structure uncertainties [20]. This makes measuring  $\tau_n$  and  $\lambda$  an attractive way to provide a second measurement of  $V_{ud}$ . In order to become competitive,  $\tau_n$  needs to be measured to  $\sim 0.3$  s precision and  $\delta A/A$  to about 0.1% precision [21].

## CHAPTER 2

### UCN INTERACTIONS

#### 2.1 UCN OVERVIEW

Ultracold neutrons (UCN) are neutrons with energies below a few hundred nanoelectronvolts (neV). UCN interact with matter via the strong force (giving rise to material potentials), with magnetic fields and gravitationally. Additionally, UCN undergo  $\beta$  decay via the weak force. In an interesting quirk of nature, these interactions all have similar magnitudes of  $U \sim E_{\text{UCN}}$ . The material interaction with bulk matter provides a potential of a few hundred neV. The potential of a UCN in a magnetic field in the adiabatic approximation is 60 neV per Tesla. A UCN in Earth's gravitational field loses about an neV per cm of height. Finally, the  $\beta$  decay lifetime is around 15 minutes, allowing storage of neutrons for tens of minutes and for measurements of their decays. This confluence of interactions allows UCN to be easily trapped inside material bottles or magnetic bottles, and to be guided from sources of UCN to experiments.<sup>1</sup>

The difficulty with UCN then becomes detection: they are uncharged so the best way to detect them is to destroy them via absorption and subsequent production of charged particles. UCN can only be tracked in detail by integrating their equations of motion in simulations and the only experimental information available is their time and place of death.

---

<sup>1</sup>The interested reader is guided to the book by Golub, Richardson and Lamoreaux, upon which this section and the next are based [23]. That text lays out the formulas I present here and gives more detail of their derivation, more examples, and a description of UCN experiments conducted at the time. I will give here only relevant results used in later chapters.

## 2.2 UCN INTERACTION WITH MATTER

Neutrons can interact with matter via the strong force. The scattering of a neutron on a single nucleus can be written using an effective potential (the Fermi potential):

$$U_{\text{F}} = \frac{2\pi\hbar^2 a}{\mu} \delta^{(3)}(\boldsymbol{\eta}), \quad (2.1)$$

where  $a$  is the scattering length of the nucleus,  $\mu$  is the reduced mass of the neutron nucleus system, and  $\boldsymbol{\eta} = \mathbf{r} - \mathbf{r}_n$ . Values of  $a$  are usually experimentally determined and can be positive or negative.

When dealing with an ensemble of nuclei where the nuclei can be assumed to not recoil instead of a single nucleus, the total effective potential can be written as

$$V(\mathbf{r}) = \frac{2\pi\hbar^2}{m} \sum_i a_i \delta(\mathbf{r} - \mathbf{r}_i). \quad (2.2)$$

Assuming an incident wave and treating multiple scattering gives an effective potential in the Schrödinger equation of

$$V(\mathbf{r}) = \frac{2\pi\hbar^2}{m} [an(\mathbf{r})], \quad (2.3)$$

where  $a$  is the bound coherent scattering length and  $n$  is the number density of nuclei.

Equation 2.3 gives a simple interaction of UCN with a wall; if a UCN comes from the vacuum and impinges on a material it will see a step function potential. The magnitude of this potential is a few hundred neV or less (and even negative for some materials). The interaction is easily treated by assuming a plane wave and by demanding continuity of the wavefunction and its derivative.

The amplitude of the reflected wave from the material boundary is

$$R = \frac{k - k'}{k + k'}, \quad (2.4)$$

where  $k, k'$  are the wavenumber before and after the potential.  $R$  is 1 in the case of a real potential and  $E_{\perp} < V$ .

In the case of absorption where the reverse process is not likely, Equation 2.3 can be replaced with a complex potential where the imaginary part describes the absorption in the material. Equa-



tion 2.4 will describe the reflection amplitude, taking into account complex  $k$  and  $U$ :

$$U = V + iW = V + i\frac{\hbar}{2} \sum_i N_i \sigma_l^{(i)} v, \quad (2.5)$$

where  $N_i$  is the number density of the absorber,  $\sigma_l$  is the loss cross section and  $v$  is the velocity of the neutron. For nuclear absorption, the loss probability is proportional to  $1/v$  and there is no energy dependence of the imaginary part of the potential.

This model can be amended for more complex surfaces such as thin films easily. In this case, the continuity of the wavefunction is imposed across all of the boundaries, giving a reflection amplitude  $R$  from the surface. The reflection amplitude is

$$R = \frac{-\bar{M}_{21}}{\bar{M}_{22}}, \quad (2.6)$$

where  $\bar{M} = \bar{M}_N \dots \bar{M}_2 \bar{M}_1$  and

$$\bar{M}_n = \frac{1}{2} \begin{bmatrix} (1 + \gamma_n) e^{i(k_{n-1} - k_n) z_n} & (1 - \gamma_n) e^{-i(k_{n-1} + k_n) z_n} \\ (1 - \gamma_n) e^{i(k_{n-1} + k_n) z_n} & (1 + \gamma_n) e^{-i(k_{n-1} - k_n) z_n} \end{bmatrix}, \quad (2.7)$$

where  $\gamma = k_{n-1}/k_n$ , and  $z_n$  is the position of the  $n$ th barrier.

If the real potential is known and the loss cross section is also known, the reflection probability is then easily obtained.

### 2.3 UCN INTERACTION WITH MAGNETIC FIELDS

Neutrons are spin 1/2 particles and see a potential from magnetic fields of

$$V = -\boldsymbol{\mu} \cdot \mathbf{B}, \quad (2.8)$$

where  $\boldsymbol{\mu}$  is the neutron's magnetic moment.

For UCN, their motion is so slow that the precession frequency is much faster than the rate of change of the  $B$  field. In this adiabatic condition, the spin tends to keep aligned (or anti-aligned) with the local field and the interaction then becomes

$$V = \pm \mu |B|, \quad (2.9)$$

where the  $+$  or  $-$  is given by anti-alignment or alignment of the field and the neutron's spin.

While UCN tend to remain polarized with or against the local field, this is not always the case. Special field configurations can induce UCN to flip their polarization (between attraction towards high fields to repulsion towards high fields), or lose their polarization during normal storage conditions. The former is useful for conditioning of UCN and the latter is a potential source of loss in magnetic traps.

## CHAPTER 3

### SOURCES OF UCN

#### 3.1 SOURCES OF UCN

The spectral density of neutrons in thermal equilibrium in a moderator will be given by a Maxwell distribution:

$$\rho(v)dv = \frac{2\Phi_0}{\alpha} \frac{v^2}{\alpha^2} \exp(-v^2/\alpha^2) \frac{dv}{\alpha}, \quad (3.1)$$

where  $\Phi_0$  is the input flux to the moderator,  $\alpha = \sqrt{2k_B T/m}$ , and  $v$  is the velocity.

The density in phase space peaks at low values of  $v$  and declines as  $v$  gets higher. As a consequence of Liouville's Theorem, in a conservative potential the phase space density for a group of particles cannot be increased. Therefore, the concentration of UCN cannot be increased by raising an ensemble of neutrons in height or by reflections from moving objects. In equilibrium, the only way to increase the density of low energy neutrons is to decrease temperature.

Loss mechanisms can affect extraction as well. Neutrons exiting a material will gain energy, and there are loss processes inside the moderator which affect the extraction efficiency of UCN. In these cases, it can be more efficient to extract a higher energy group of neutrons from a moderator and cool them in a controlled way into an experiment [23].

Gains in phase space density can be made if the neutrons are not in thermal equilibrium with the moderator. In this case, the density can be enhanced above thermal equilibrium density. Take, for example, a 2-level system with ground state  $E_{\text{UCN}}$  and an excited state  $E_{\text{UCN}} + \Delta$ . In this system, neutrons of energy  $E_{\text{UCN}} + \Delta$  can lose  $\Delta$  in energy and become UCN, or UCN can interact

and gain  $\Delta$  in energy and leave the UCN range. Using the principle of detailed balance, the up-scattering (leaving UCN energies) cross section is given by

$$\sigma(E_{\text{UCN}} \rightarrow E_{\text{UCN}} + \Delta) = \frac{E_{\text{UCN}} + \Delta}{E_{\text{UCN}}} \exp(-\Delta/k_{\text{B}}T) \sigma(E_{\text{UCN}} + \Delta \rightarrow E_{\text{UCN}}). \quad (3.2)$$

If the down-scattering cross section does not depend on temperature, then the upscattering cross-section will be suppressed exponentially with lowering temperature. The rate of UCN production will be higher than the rate of UCN loss and the saturation density will be increased significantly compared to steady-state moderation only.

Deuterium can be used as a superthermal source [24]. In the case of deuterium, the system has more than 2 levels, but the same idea that the down-scattering production rate can be enhanced at low temperatures applies. The production rate can be calculated with knowledge of the phonon spectrum of deuterium for example in [25].

The lifetime in deuterium is relatively short (a few hundred ms), limiting the saturation density at constant input flux. However, if the input flux is pulsed at higher intensities and lower duty cycles, this can be mitigated [26]. In such a source, UCN can be produced from deuterium during an intense beam pulse. These UCN are then sent to the experimental volume where the lifetime is significantly longer than in the deuterium. During periods where no UCN are produced, the deuterium is closed off from the experiment; the UCN now are lost with the lifetime of the experiment and not the deuterium. Pokotilovski estimated that a source built this way could see an order of magnitude or more improvement over UCN sources that were currently in operation.

### 3.2 LOS ALAMOS NEUTRON SCIENCE CENTER UCN SOURCE

The ultracold neutron Source currently installed at the Los Alamos Neutron Science Center (LAN-SCE) is a superthermal solid deuterium source using spallation neutrons. Data taken in the 2016-2017 run cycle uses the most recent source upgrade [27]. Data taken in the 2015-2016 run cycle uses a previous source iteration [28]. Spallation neutrons are produced from an 800 MeV

pulsed proton beam at  $\sim 9 \mu\text{A}$  average current impinging on a tungsten target. These neutrons are moderated by a polyethylene moderator at  $\sim 45 \text{ K}$ . Cooled neutrons then interact with a solid deuterium crystal of about  $\sim 1.5 \text{ L}$  in volume to create UCN.

During a beam pulse ( $\sim 1 \text{ s}$ ), UCN are guided out of the source past a butterfly valve. After the proton pulse is turned off for  $\sim 10 \text{ s}$ , the butterfly valve is closed and the UCN only interact with the guides out of the source. The guide system consists of a vertical extraction guide of height  $1 \text{ m}$  coated in  $^{58}\text{Ni}$ , which has a material potential of  $335 \text{ neV}$ . UCN are then guided horizontally out of the biological shield via a  $6 \text{ m}$  guide coated with Nickel Phosphorus with a material potential of  $213 \text{ neV}$  [29]. Neutrons are then passed through a gate valve (GV) which can separate the source from the downstream experiments.

UCN are then guided through a pre-polarizing magnet (PPM). The PPM is a  $6 \text{ T}$  superconducting magnet inline with the beam. UCN which are in a high-field seeking spin state will be accelerated through the magnetic field and are typically passed through a foil that separates the source vacuum from the experimental vacuum. UCN in a low-field seeking spin state do not have enough energy to penetrate the  $6 \text{ T}$  magnetic field so do not pass into the experimental volume.

The upgraded UCN source was capable of producing  $39 \text{ UCN/cc}$  in a prototype cell coupled after the polarizing magnet. Densities in the Los Alamos UCN lifetime experiment are significantly reduced from this (approximately  $0.05 \text{ UCN/cc}$  inside the trap) due to spectral conditioning and additional guiding of UCN.

## CHAPTER 4

### HARDWARE OVERVIEW

UCN $\tau$  is a neutron lifetime experiment using magnetically and gravitationally trapped ultracold neutrons. A schematic drawing of the UCN $\tau$  apparatus is given in Figure 4.1.

UCN exit the biological shield in a horizontal guide coming from the source. UCN can interact with several pinhole detectors for monitoring. During the 2016-2017 run cycle there were 3 such monitors: the first-generation  $^{10}\text{B}$  coated ZnS:Ag UCN monitor (called the old monitor or OL), and 2 paired  $^{10}\text{B}$  coated ZnS:Ag monitors. The characteristics of  $^{10}\text{B}$  coated ZnS:Ag UCN monitors are detailed in Section 8.1. An aluminum foil is placed in the pinhole of one of the paired detectors. The foil monitor is abbreviated AL, and its twin is the bare monitor or BA. These 3 monitors are called gate valve monitors. These monitors count hundreds UCN per second during UCN production and have a background on the order of mHz.

UCN can then pass through a gate valve. This gate valve can open or close the guide exiting the biological shield. The gate valve is operated via compressed air and is typically only open during the UCN filling procedure.

After the gate valve, UCN pass through the pre-polarizing magnet (PPM) described in Section 3.2.

After passage through the PPM the UCN are polarized in a high-field seeking state (since only UCN attracted to high fields can pass through the 6T magnetic field). The spins need to be flipped in order to be trapped inside the magnetic bottle. Spin flipping is done via an adiabatic fast passage

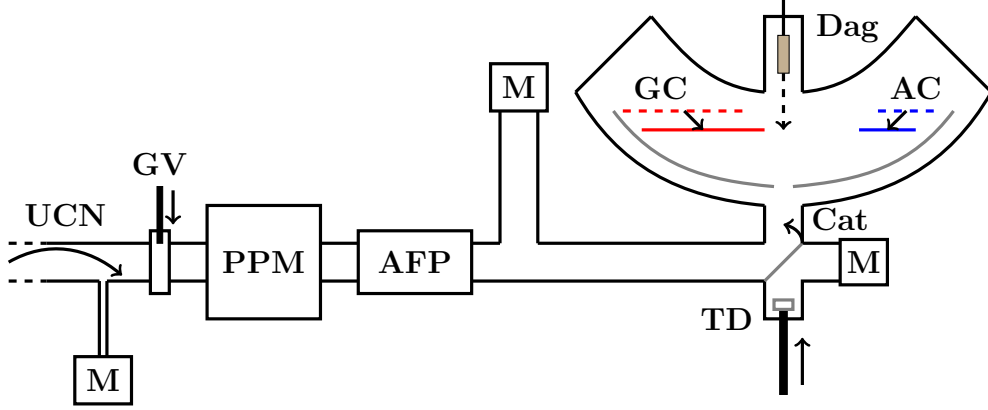


Figure 4.1: Block Diagram of UCN $\tau$ . Key: **M**: Monitor Detector, **GV**: UCN Gate Valve, **PPM**: Pre-Polarizing Magnet, **AFP**: Adiabatic Fast Passage Spin Flipper, **TD**: Trapdoor, **Cat**: Catdoor, **GC**: Giant Cleaner, **AC**: Active Cleaner, **Dag**: Dagger Detector

spin flipper (AFP). The AFP uses an RF field in addition to a monotonically decreasing magnetic field to reverse the polarization of UCN [30]. In a rotating frame at the RF frequency  $\omega$  about the beam direction, the magnetic field sweeps from aligned along the beam in one direction to being aligned in the opposite direction. The UCN spin will follow this change in direction adiabatically going from being aligned to anti-aligned with the beam. In the lab frame, the UCN will go from being aligned to anti-aligned with the monotonically decreasing field.

The AFP needs to be tuned such that the combination of RF field and magnetic field gives the resonant condition. In the 2015-2016 and 2016-2017 datacycle, the spin flipper was tuned by fixing the frequency at  $\omega=372$  kHz and tuning the current in the monotonically decreasing  $B_0$  coil. The rate is monitored in either a detector which passes only high-field seeking UCN (via an iron foil) or by monitoring the rate of the dagger detector inside the trap which acts as a large spin filter. Tuning is discussed further in Section 12.1.

After flipping in the AFP, UCN then enter a tee in the guide system. A monitor is placed on the upper portion of the vertical guide at a position above the top of the trap. The height ensures that only UCN above the trapping potential are counted (and therefore lost). The vertical monitor, or the standpipe (SP), is a large area detector with the same cross-section as the guide. This monitor

uses the same  $^{10}\text{B}$  coated ZnS:Ag technology as the gate valve monitors. The standpipe counts significantly more UCN than the pinhole monitors and is used as one of the main monitor detectors in normalization. The standpipe monitor counts a few thousand UCN per second.

The other direction of the tee guides UCN to a 3-way transition junction. The transition region consists of a copper box with a copper plate (the catdoor) that can rotate and select the direction for UCN to travel. The plate can be in 3 positions: at  $45^\circ$  which allows UCN to be guided with limited losses into the trap, horizontally which allows UCN to view a 5th detector, and vertically which allows the bottom portion of the Halbach array (the trapdoor) to move into position. A 5th  $^{10}\text{B}$  coated ZnS:Ag UCN monitor is placed at the downstream termination of the guide system and is called the downstream monitor. The downstream monitor counts approximately an order of magnitude fewer UCN than the gate valve monitors, except when the copper plate is actuated where UCN are freely able to be counted during transition.

UCN are guided into the trap through a copper box and past a transition region where a  $\sim 15$  cm square piece of the Halbach array is removed. During the filling procedure, UCN are free to enter or leave the trap and build up to a saturation density determined by the draining time of the trap, approximately 70 s.

There are 2 spectral cleaners inside the trap: A large-area cleaner (approximately half of the trap) with a polyethylene surface and an active cleaner made of a  $^{10}\text{B}$  coated ZnS:Ag UCN monitor. The former is known as the giant cleaner and the latter the active cleaner. Polyethylene has a negative UCN potential and a high cross-section for upscattering UCN and is therefore effective at eliminating UCN which impinge on its surface.

Both the giant and active cleaners can be retracted; the giant cleaner can be retracted by approximately 5 cm. The height of the giant cleaner was determined by lowering the dagger detector to match the height of the cleaner. The height was compared using a laser level and was determined to be approximately 38 cm from the bottom of the trap. The height of the active and giant cleaners were also checked in the same way and were found to be matching.



The dagger detector is a slab of plastic covered with  $^{10}\text{B}$  coated ZnS:Ag UCN monitors on either side. The profile of the bottom is matched to the profile of the Halbach array so that it can be inserted into the bottom of the trap. The detector can be raised or lowered between 1 cm to 49 cm from the bottom of the array. In the lowest position the detector drains the trap population with a time constant of  $\sim 7$  s.

## CHAPTER 5

### TRAPDOOR

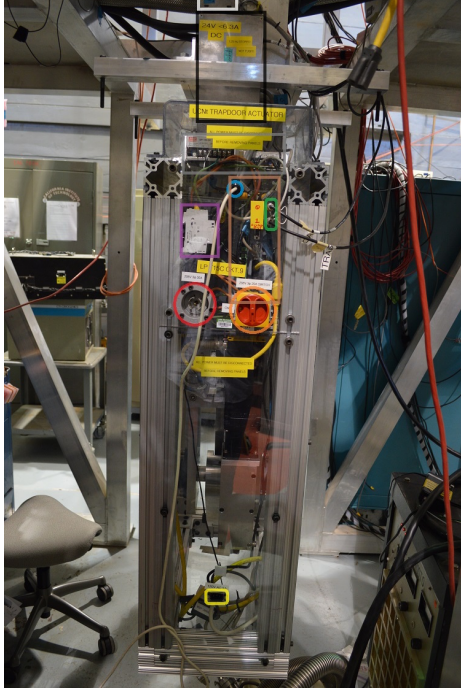
#### 5.1 TRAPDOOR ACTUATOR SYSTEM

The trapdoor actuator system can be seen in Figure 5.1a. Shown is the electronics portion of the assembly consisting of a servo motor, several drives, power supplies, and an electronics box. The main gear assembly can be seen in Figure 5.1b. A worm rotates the large gear and the rotation is turned into linear actuation via 2 arms in a reciprocating motion. The trapdoor only needs to travel between completely plugging the array and completely withdrawn from the UCN volume. The worm drive only rotates between limited angles and up and down motion is obtained by running forwards or backwards. Cutouts prevent the shaft from being driven too far in either direction.

A Parker Compax3S drive controls the servo motor. The drive was programmed using the IEC61131-3 standard.

The trapdoor system also controls and actuates a copper plate (called the catdoor) which selects the geometry of the UCN transition region. UCN enter into a copper transition region at beam height and are either directed upward towards the trap, into a downstream detector and upwards, or back to the source. In the first 2 configurations, the plate forms a geometry where UCN do not see the trapdoor. The copper plate is actuated via a stepper motor and monitored using hardware switches at the 3 positions.

The catdoor stepper motor is driven by a discrete logic box. Microswitches were placed so that



(a) Trapdoor control electronics



(b) Trapdoor gear mechanism

Figure 5.1: Trapdoor as installed at Los Alamos National Laboratory

they were pressed when the catdoor was at its filling, dump, or up positions. The electronics reacts to the state of the microswitches and state of the Compax3S controller to drive the catdoor. A simplified block diagram of the catdoor electronics is given in Figure 5.2.

The catdoor electronics box takes 6 inputs: 3 switches (fill, dump, up), travel direction, latch reset, and enable. The travel direction, latch reset, and enable are digital outputs from the Compax3S and controlled in software. The box outputs either a square wave or LOW. The square wave causes the stepper motor to advance one step per pulse.

When the Compax3S resets the latch,  $\overline{Q}$  goes HIGH. If the enable is also HIGH, the AND evaluates to TRUE and the square wave is passed through the second AND gate. If the enable were to be driven low, the AND gate would evaluate to false, and no square wave would be generated.

When any one of the switches is pressed, the final OR output will be driven HIGH. The step

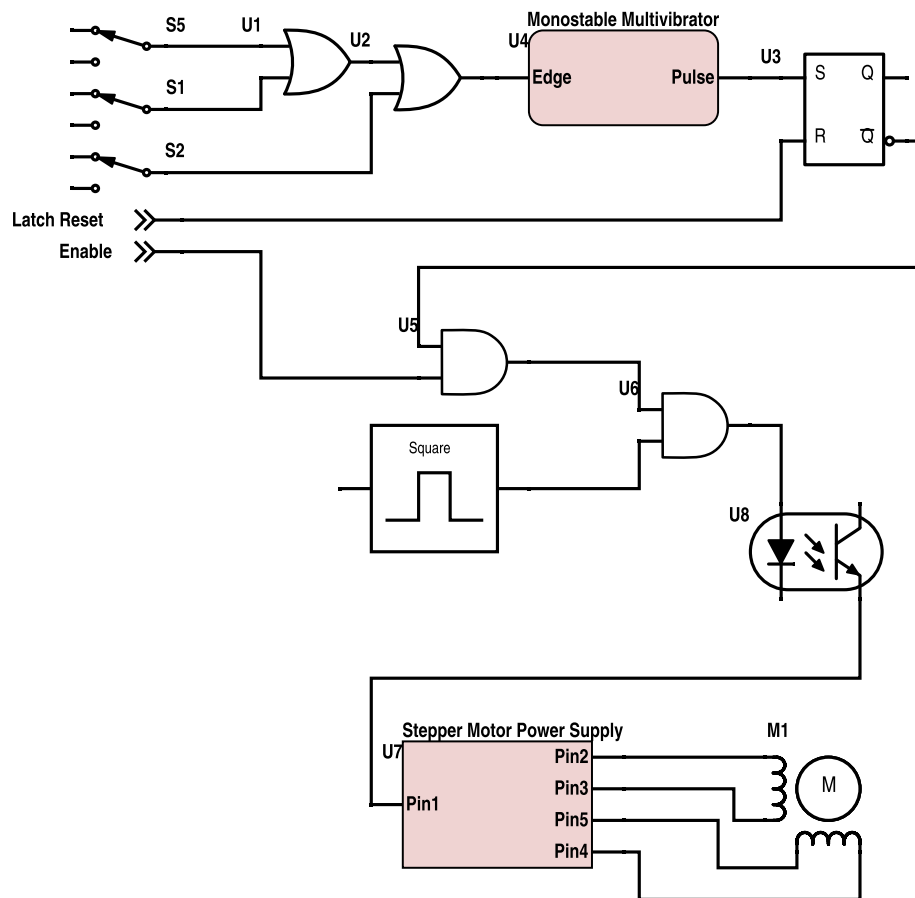


Figure 5.2: Block diagram of catdoor electronics

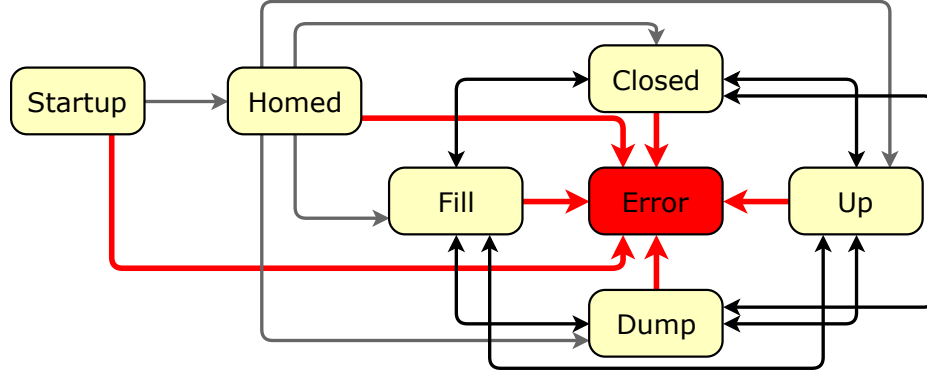


Figure 5.3: State diagram of the trapdoor software

pulse triggers the monostable multivibrator to create a single timed pulse into the set pin of the latch, driving  $\overline{Q}$  LOW. When  $\overline{Q}$  is LOW, the first AND is evaluated as FALSE and no square wave is generated.

The Compax3S can then enable the catdoor to rotate until it hits a switch at which point it stops. The system is moved into the desired state by commanding the catdoor to move until the correct switch is pressed.

## 5.2 TRAPDOOR SOFTWARE

The Compax3S controller was programmed as a state machine. The state diagram is given in Figure 5.3.

The software consists of several transitional initialization states, four configurational states (catdoor up/down/fill and trapdoor down or catdoor up trapdoor up), and a single absorbing error state. Once in the error state the unit will not respond to further transition requests until it is power-cycled.

When the unit is powered on, it is in the default state. The program can only transition into a homed or error state. The apparatus can be homed via a manual homing program. The homing finds a set position in the trapdoor travel by locating the edge of a switch. Once in the homed state it can proceed to one of the 4 main states or to the error state.

Cat	Trap	Error
1	1	The catdoor engaged at the up position but has fallen off the switch
1	0	One of the limit switches has been pressed
0	1	There was a following error (slipping in gears or coupler)
0	0	The error was none of the above

Table 5.1: Compax3 digital output error table

Once in a main state, the apparatus can only transition to other main states or the error state. The software is notified of a transition request via RS232 communication or hardware signals. The software determines how to move the catdoor and trapdoor to safely transition the system into the new state. If an error occurs during transition the system will go to the error state.

Errors occur from the firmware (power conditions, servo performance, temperature, etc.) or in software (inconsistencies in the state or status of switches). The former are part of the Compax3S firmware and are not controlled or modified in any way. The latter are programmed in software.

The software is able to stably operate for several days or weeks after successful homing. The most common cause of failure was degradation of the worm/wheel interface causing servo tracking errors. Periodic lubrication (approximately monthly) mitigates the servo tracking problems.

The Compax3 was also configured to generate 2 signals that indicate catdoor or trapdoor movement respectively. These signals are sent to the DAQ and recorded during the run so that the times when the actuator moves is known. In the event of an error, the outputs encode some information, given in Table 5.1. Additionally, 2 inputs to the unit were used to allow hardware signals to request transitions. Three unique combinations (low/high, high/low, high/high) are used to command the trapdoor to 3 unique states. This feature was unused at the time of writing.

The trapdoor is commanded from a Linux PC. A server program runs on the PC independently of the UCN $\tau$  experiment control program. The control program sends requests to the server program which communicates directly with the trapdoor controller via RS232. Because the Compax3S

software acts as a state machine, the server program does not need to do any error checking or keeping of state.

## CHAPTER 6

### GIANT CLEANER

The giant cleaner is the primary way in which high-energy UCN are removed from the experiment. A rendering of the giant cleaner hardware can be seen in Figure 6.1. The hardware was designed by Walt Fox and was first installed during the end of the 2015-2016 run cycle. The height was discovered to mismatch with the original small cleaner; the cleaning height was lowered to be approximately 38 cm from the bottom of the trap during the subsequent shutdown period. Small standoffs were machined (not pictured in rendering) and attached to the aluminum structure that holds the polyethylene at the 3 mounting points. The cleaner was designed to move at least 5 cm upwards at the end of the cleaning time to avoid cleaning during storage time.

The actuator is a Nook Industries CC Series Compact Cylinder screw drive. The stock motor was replaced with a stepping motor so that the actuation could be controlled more easily. The screw has a lead distance of 0.2" per revolution, the Nook drive has an 18:1 gear ratio, the stepper motor has a 4000 count per revolution encoder, and the stepper motor travels 1690000 encoder counts between the raised and lowered position. This moves the shaft 4.69" which should correspond to moving the giant cleaner approximately >5 cm up and down.

The Nook drive was configured from the factory to be used with a DC motor. The limit switches were factory configured to bypass a diode such that the circuit path is interrupted when a limit switch is pressed. The limit switches were instead taken out of the diode circuit and act as limit switches only.



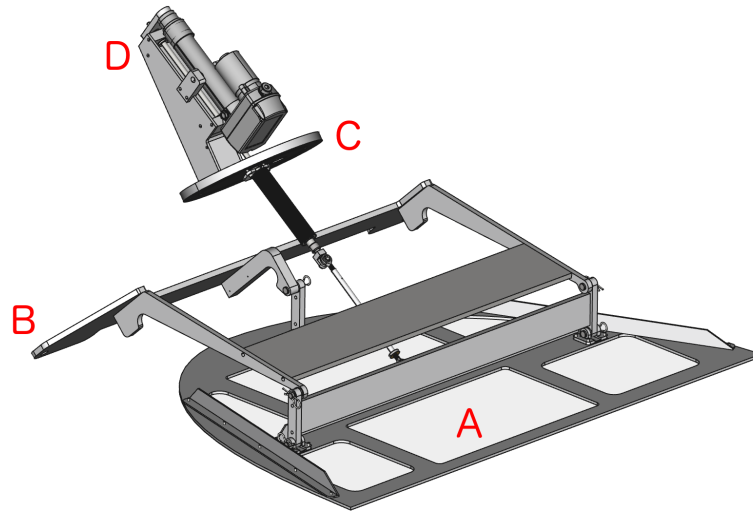


Figure 6.1: Rendering of the giant cleaner. A: Polyethylene surface, B: Mounting bracket, C: Vacuum break, D: Linear actuator

The bottom limit switch was chosen to act as a homing position. During startup, the drive will move until the switch is pressed. Software limits of 1% on either end were chosen so that the limit switches were not pressed during normal running.

Repeatability was only measured with the stepper motor encoder. The limit switch was reached with an error of approximately half a percent which would correspond to  $20\text{ }\mu\text{m}$  difference if the coupling was direct. Friction may cause a larger difference in the cleaner height, but the cleaner height repeatability was not measured directly.

The cleaner software consists of a Python server which accepts commands from the control system and forwards them to the giant cleaner. The software uses the Applied Motion SCL command language. Initially, the drives were commanded to actuate by the number of steps only and did not use the encoder. Future versions of the software were programmed to use the encoder to check the final position.

Movement commands were programmed to immediately take effect. The drive is also capable of queueing commands and popping off the queue on external triggers. A software position limit

is imposed in the Python server, but is not enforced on the drive. The Python software keeps a persistent state so that it knows where to command the cleaner.

## CHAPTER 7

### OVERVIEW OF UCN $\tau$ ANALYSIS

The following analysis is a detailed account of one of the three independent analyses performed on the data taken in 2016-2017 in the UCN $\tau$  experiment [31]. The lifetime can be measured in one simple equation, only needing the sum of counts in long and short runs. The difficulty of analysis lies in ensuring that the sum of UCN in long and short runs are compared on equal footing with sufficient accuracy. Loss of just 20 UCN out of 30000 over 1400 s can lead to a shift in lifetime of 0.4 s, which is an unacceptable shift in  $\tau$ . The effects of normalization and counting efficiencies also need to not perturb the sum of UCN to similar precision.

The lifetime will be measured by taking the sum of UCN in paired short and long runs. A lifetime will be calculated for each pair taking into account the source strength, counting efficiencies, and backgrounds. The sums will come from either identification of individual UCN events or by integration in current mode where each UCN is represented by tens of individual photons. These individual lifetime values will then be averaged for a lifetime value for each run condition. These averaged lifetime values will again be averaged for a final, high-precision measurement of  $\tau_n$ .

#### 7.1 SYSTEMATIC EFFECT ANALYSIS

Systematic effects come in one of 2 flavors: direct loss of UCN during storage or distortions in the sums. Loss mechanisms will be either measured via the data or simulated to place limits on the shift in  $\tau$ . UCN loss during storage can come from uncleaned overthreshold orbits, microphonic

heating, depolarization, and residual gas upscattering.

Effects which distort the sums include normalization of the source flux, background subtraction, pileup, deadtime, and phase space evolution. These effects will be studied and limits placed on them.

## 7.2 MISCELLANEOUS TASKS

Most of the running time is dedicated to production runs to measure  $\tau_n$ . However, some portion of runs were conducted to explore the operation of the UCN $\tau$  apparatus and to investigate systematic effects such as phase space evolution or detection efficiency. These miscellaneous run types are investigated and interpreted. These runs typically do not yield a quantitative effect on the lifetime.

## CHAPTER 8

### UCN EVENT RECONSTRUCTION

#### 8.1 ZNS:AG SCINTILLATOR

In the UCN $\tau$  apparatus, UCN are detected via an *in situ* scintillator-based detector [32]. The UCN detectors used in the experiment consist of a ZnS:Ag screen prepared by Eljen Technology with  $3.25 \pm 0.25$  mg/cm<sup>2</sup> of phosphor coated in a thin ( $< 20$  nm) layer of <sup>10</sup>B. The ZnS:Ag thickness corresponds to 8  $\mu$ m if it were a pure crystal, but due to the polycrystalline nature would be thicker. The ZnS:Ag is coupled to a PMT either directly in the case of monitor detectors, or via wavelength shifting fibers in a PMMA slab [33]. In the latter case, the fibers were fed into 2 separate PMTs so that coincidence events could be constructed between them. UCN incident on the coated boron surface easily penetrate due to the low material potential of <sup>10</sup>B and have a high probability of capture (<sup>10</sup>B has a 3835 barn cross section for thermal neutrons - compared to 1.1 barn for Zn nuclei and 0.53 barn for S nuclei [34]) - in the <sup>10</sup>B( $n, \alpha$ )<sup>7</sup>Li reaction. The absorption length of UCN in the <sup>10</sup>B layer is  $\sim 40$  nm, which was chosen as a tradeoff between absorption efficiency and light collection efficiency. The decay products - either the  $\alpha$ , <sup>7</sup>Li ion, or both - penetrate the <sup>10</sup>B layer and create scintillation light in the ZnS:Ag layer. The decay is back-to-back, so one particle is guaranteed to be emitted towards the scintillator. In 96% of the decays, a  $\gamma$  is also produced, but is neglected because the probability of interaction in the ZnS:Ag layer is small. Each UCN that is absorbed on the surface then produces a burst of light that can be detected.

Initially,  $\sim 7.5$  to  $9 \times 10^4$  photons are yielded from the ZnS scintillator isotropically during a

UCN event [32]. Half escape and half have a chance of entering the PMMA slab and interact with the wavelength shifting fibers. Photons that are absorbed in the fibers are re-emitted isotropically and conducted to one of 2 PMTs. In the end, roughly 20 photons are measured in the two PMTs per UCN, meaning the collection efficiency is on the order of 1 per two thousand.

The light from the scintillation events in the detector can be measured by either summing the total number of photons (called "singles" analysis), or by finding coincidence events to determine the number of UCN counted. In the former case, the number of UCN counted is never used. The singles analysis is susceptible to large backgrounds which need to be measured for each run; the coincidence analysis is less sensitive to backgrounds but needs deadtime and pileup corrections due to the long emission time constant of the ZnS:Ag scintillation light.

The individual photons from the scintillation light are discriminated and counted in a Multi-Channel Scaler unit which records the event times of each pulse it receives.

The light from ZnS:Ag has several time components: a short time constant and several longer time constants. The scintillation time constant is commonly stated as 200 ns [35] [36, p. 238]. However, in our detector the ZnS:Ag also has long time components up to several microseconds as can be seen in Figure 8.6.

## 8.2 COINCIDENCE IDENTIFICATION

Coincidence identification can improve the signal to noise ratio observed from UCN counting. When the total sum of photons is measured, the backgrounds are around 1 kHz with a total number of counts around  $1 \times 10^6$ . Measurement time is at least 100s, giving a signal to background of around 9:1. For coincidences, the background is around 100 mHz and the number of events is around 20000, giving a signal to background of around 2000:1. Due to the clumped nature of photons, the statistical precision is equivalent between the two methods. However, the coincidence method is superior when the expected signal is small (when looking for uncleaned UCN for example).

The large light output from the ZnS:Ag allows the creation of coincidence events to reduce

background rate. Charged heavy ions produce about 1.3 times higher shaped pulses compared to NaI:Tl crystals when viewed with a PMT directly [36, p 238]. NaI:Tl produces 38000 photons/MeV for comparison. Coincidence between the 2 PMTs (a count in PMT 1 followed by a count in PMT 2 within some window) has high backgrounds from non-UCN particle events. A secondary cut on the sum of photons in the tail is used to discriminate UCN events from backgrounds even further.

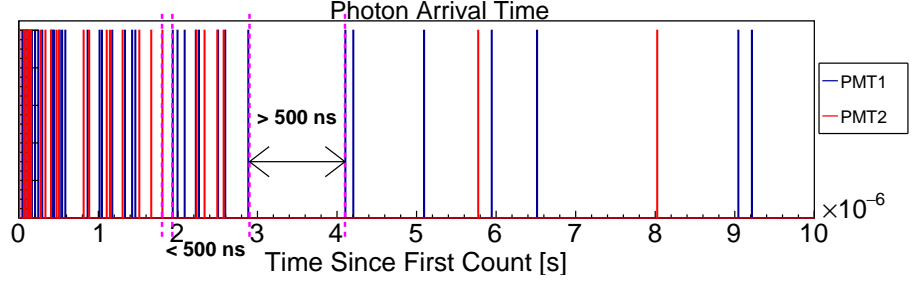
The algorithm used to identify UCN events is as follows:

- Search for a coincidence between PMT 1 and PMT 2 within 50 ns
- Sum the first two counts plus all subsequent counts in PMT 1 and PMT 2 while the interarrival time is  $< 500$  ns
- Take events where the sum is  $\geq 8$
- If the event does not pass cuts, continue with the count after the first count in PMT 1 or PMT 2 that started the coincidence search

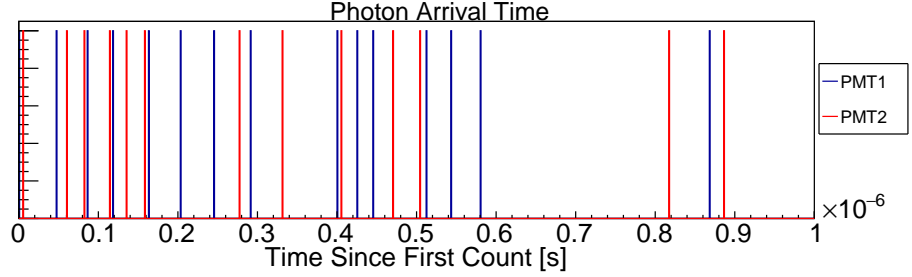
A variant can be done where instead of the "telescoping" window based on interarrival times, a prescribed window is used. Step 2 is replaced by summing while the arrival time is  $< 4000$  ns since the first PMT 1 or PMT 2 event.

A coincidence event is displayed in Figure 8.1; each photon count is a vertical line. Figure 8.1a shows the long tail (tens of photon counts out to  $10 \mu\text{s}$ ). The initial burst of short time constant photons can be easily seen. Figure 8.1b shows a further zoomed in view of photon events. It can be seen that this event satisfies both coincidence algorithms. Two counts are found within 50 ns of each other, and the sum where the interarrival time is less than 500 ns is easily more than 8. In this case, the integration for the telescoping coincidence would end after  $3 \mu\text{s}$  because the next count in PMT 1 or PMT 2 is  $> 500$  ns. The interarrival time is the time from a PMT 1 or PMT 2 event to the next PMT 1 or PMT 2 event.

A rough estimate of efficiency can be taken by measuring the coincidences between the main UCN dagger detector and a separate cleaning detector which also views light from UCN events in the dagger detector. The efficiency is estimated by dividing the coincidence rate between the



(a) Photon counts zoomed to 10  $\mu\text{s}$  after first count



(b) Photon counts zoomed to 1  $\mu\text{s}$  after first count

Figure 8.1: Photon arrival times for a single UCN event

dagger and the cleaner by the rate in the cleaner.

This estimates the efficiency at  $\sim 95\%$ . That is, 95% of  $^{11}\text{B}$  decays that produce significant amount of light are detected by the dagger. This does not account for UCN interactions with  $^{10}\text{B}$  which can further reduce efficiency of UCN counting.

### 8.3 BACKGROUNDS

Major sources of backgrounds in the PMT are PMT dark noise, non-UCN particle events, and detector actuation. PMT dark noise is caused by thermionic emission of electrons which are subsequently accelerated and counted; this is temperature dependent and  $\sim 500$  Hz per tube at 290 K. Non-UCN particle events come from muons,  $\alpha$  particles, etc. which create scintillation light in the ZnS. Alternatively, particles could create Čerenkov light when passing through the PMMA plastic which embeds the fibers or through the fibers themselves. The detector is actuated using a stepper motor which has a switching power supply at 20 kHz [37] which can broadcast EMI



(electromagnetic interference) noise and cause triggering in the electronics chain.

Only particle events contribute significantly to coincidence backgrounds. Because the dark noise has a low rate, there is very little probability that there would be an accidental coincidence in the 2 PMTs (the dark noise is independent), in addition to 6 extra events within the integration windows. This can be modeled simply with a Poisson process: the probability of a dark count arriving within 50 ns of a previous one is  $1 - \exp(-500 \text{ Hz} \times t)$  or about 25 ppm. The probability of 6 or more extra events could be approximated with a Poisson distribution with an expectation of  $1 \text{ kHz} \times 4000 \text{ ns}$  (the sum of the 2 rates over  $4 \mu\text{s}$ ), or  $1 - \frac{\Gamma(5+1, 1000 \text{ Hz} \times 4000 \text{ ns})}{5!}$  or 6 parts in  $10^{18}$ . The combined probability is 1.5 parts in  $10^{22}$  for each 4050 ns; we could expect one event per terasecond. The same is true for the 20 kHz noise; it could create initial coincidences because the PMTs see the same source, but the interarrival time for 20 kHz noise is  $50 \mu\text{s}$  so it will not contribute enough counts to pass the threshold.

The dark noise is time dependent from both ambient temperature fluctuations and internal fluctuations due to heating of the PMTs during operation in the vacuum. Figure 8.2 shows the time dependence of the dark rate. Due to the fluctuations it is important to assess singles backgrounds on a run-by-run basis. In the 2016-2017 data, the singles backgrounds were taken for each run at either the end of the run (when available), or with the dagger at the cleaning height (where there were no observable counts). The background counts were assigned Poisson uncertainties.

Backgrounds from particle events are position dependent. Figure 8.3 shows position dependence of background singles. For each run, the rate at different heights is subtracted from the rate at a reference height (chosen to be the cleaning height of 380 mm). Some runs did not have background segments at 10 mm and some runs did not have a cleaning check step. Additionally, a set of background runs were taken in 2016 where the dagger was placed in 4 positions; another set of background runs were taken in 2017 where the dagger was placed in 9 positions. The position dependence could be caused by extra background particle events at higher heights. The rate differences were fit to

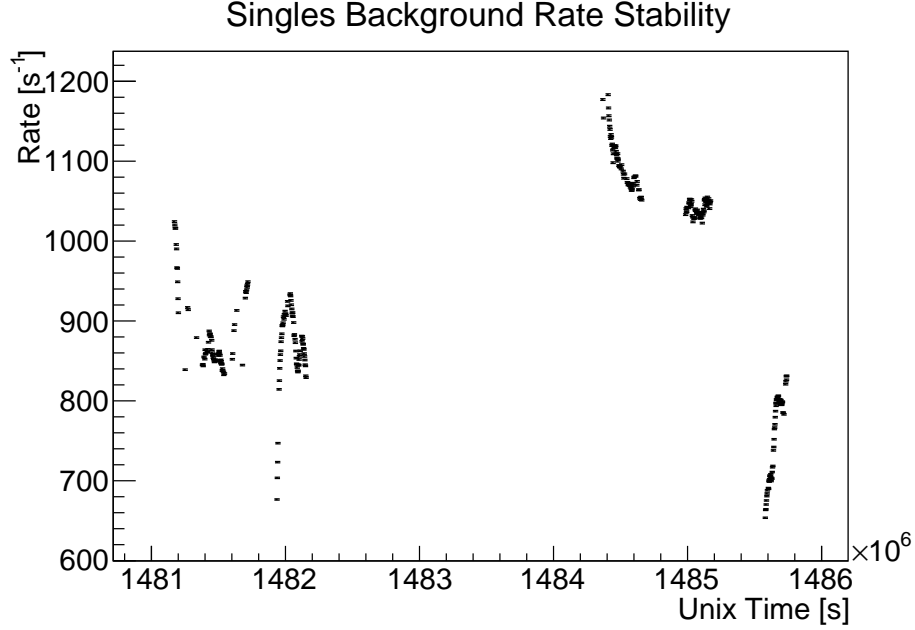


Figure 8.2: Dark rate as a function of time in the experimental area. Runs come from several months of data taking and several cycles of the vacuum system/detector electronics

$$\Delta R(h) = Ah^2 - A380^2, \quad (8.1)$$

where  $A$  is the fitted parameter, and  $h$  is the height of the dagger in mm. This forces the difference to be 0 at 380 mm. The  $\frac{\chi^2}{\text{NDF}}$  was 3 for the fit to all data points below 380 mm. The errors in the fit were estimated by the MINUIT package via the ROOT data analysis framework.

Points above 380 mm were discarded for the fit. Above the height of the cleaning check, the geometry is significantly more complicated which could lead to a departure from the simple fit function. Additionally, the background at 490 mm is never used in the extrapolation for the singles analysis so the fit does not need to be accurate in that regime. For  $h < 380$  mm,  $A = 8.0\text{E-}5 \pm 2.3\text{E-}6 \text{ s}^{-1}\text{mm}^{-2}$ .

Coincidence backgrounds were observed to be stable throughout run segments. The first data set taken has a slightly lower background. For coincidence data, backgrounds were measured during the long holding time for each pair and corrected for position dependence in the same way as the

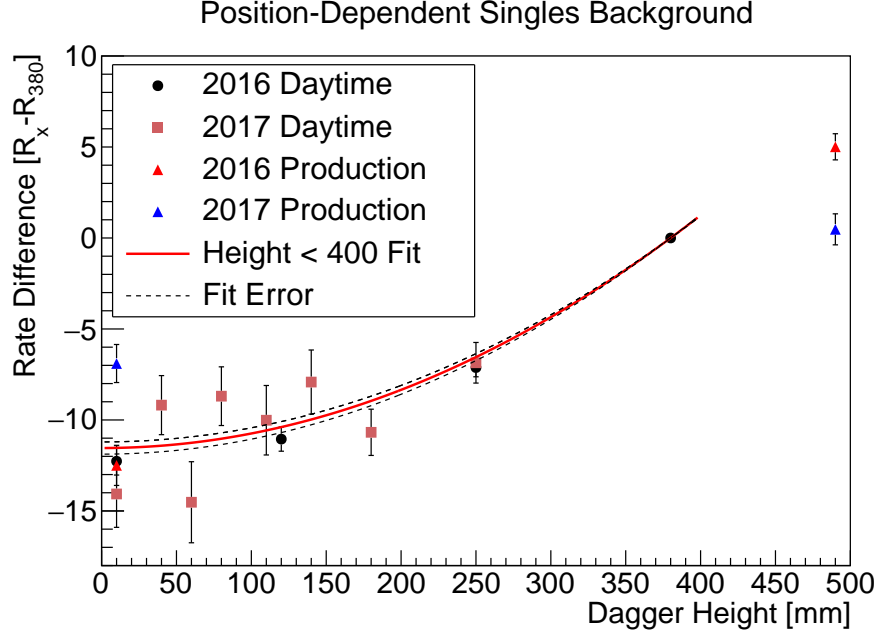


Figure 8.3: Position Dependence of singles background. Data comes from 4 sets - either dedicated background runs or production runs in either 2016 or 2017.

singles data. Figure 8.5 shows the coincidence background from the holding time as a function of time in the experimental area.

Coincidence backgrounds also were position dependent. To evaluate the position dependence, the 4 step background runs were combined with backgrounds measured at the holding height during long storage runs and at the bottom of the trap. Coincidence background rates showed an opposite trend: background rates were higher at the bottom of the trap. A linear function was used to fit this data. Figure 8.4 shows the fit. The slope was found to be  $-5.1\text{E-}5 \pm 7.3\text{E-}6 \text{ s}^{-1}\text{mm}^{-1}$ .

## 8.4 DEADTIME

Due to finite discriminator width, deadtime exists in the detector for singles events. A nonparalyzable deadtime correction is made [36, p. 122]:

$$n = \frac{m}{1 - m\tau}, \quad (8.2)$$

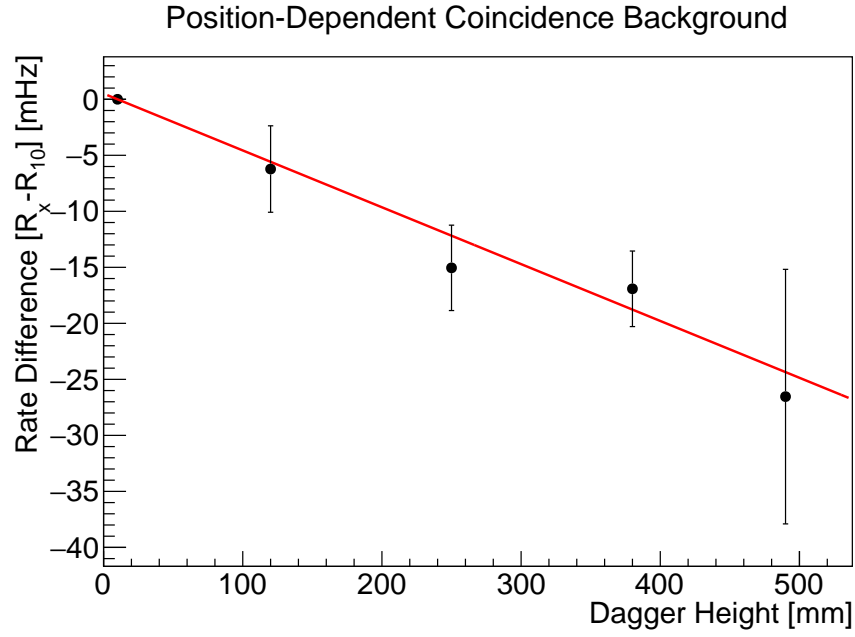


Figure 8.4: Position Dependence of coincidence background. Data comes from 2 sets - 4 step dedicated background run or production runs in 2017 and 2016.

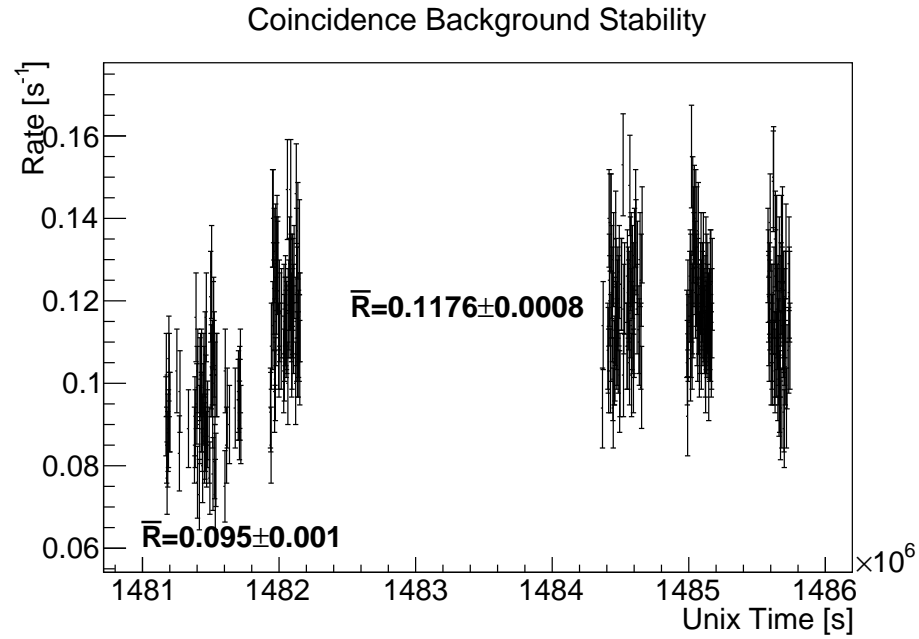


Figure 8.5: Coincidence Background Rate as a function of time.

where  $n$  is the corrected rate,  $m$  is the recorded rate, and  $\tau$  is the fixed deadtime. An uncertainty of 20% is given to  $\tau$  based on investigations of the gate width using an oscilloscope.

## 8.5 RATE DEPENDENT EFFECTS IN COINCIDENCE ANALYSIS

The coincidence finding routine combined with the long time constants of the ZnS:Ag light cause rate dependent counting effects. Deadtime effects come from the several  $\mu\text{s}$  integration windows. Pileup effects come from the long tail of light in the scintillator. The efficiency of counting UCN is higher at higher rates because there is more light and therefore a higher chance to exceed the threshold.

Standard deadtime corrections as described above do not work with the coincidence algorithm. This is due to deadtime corrections assuming no counts can be detected inside the deadtime of the system. In the detection system for UCN, this is not true; an event can begin inside of a summing window, but still be counted after the window has ended. Events that fall inside of the deadtime aren't "dead" but just have a reduced probability of detection.

The pileup causes additional UCN to be counted at high rates. When rates are high, if a candidate UCN event is preceded by a UCN event, photons from the tail of the first event can be measured in the second. The extra photons add to the sum and bring some events over threshold where they would not have been overthreshold otherwise. Additionally, there is extra probability of double counting events on the tails due to the same effect.

### 8.5.1 RATE DEPENDENT EFFECT SIMULATION

Due to the inability to make standard deadtime corrections and the pileup effect, Monte Carlo simulations can be used to correct measured lifetimes when using coincidences.

The Monte Carlo simulation is based on resampled data from the 2016-2017 run cycle. A summed waveform and pulse height distribution was compiled for both foreground and background counts. In each case, coincidences were identified and only coincidences without other coincidences

preceding or following within  $40 \mu\text{s}$  were used. For foreground counts, a cut of 4 photons was used with 50 ns initial coincidence and 500 ns telescoping integration window. For background counts, this cut was lowered to 2 photons with the same windows. The arrival time of photons for each selected coincidence were compiled into a histogram with a length of  $40 \mu\text{s}$  and the number of photons in each PMT were compiled into a pulse height histogram. A separate arrival time histogram was generated for each PMT and a separate histogram was generated for when PMT 1 was the first event or PMT 2 was the first event for a total of 4 arrival time histograms. The fraction of coincidences that began in PMT 1 was also recorded. Additionally, the average background rate was recorded so that background coincidences could be injected into the data. Figure 8.6 shows the arrival time histograms used for the Monte Carlo simulation. Figure 8.7 shows the Pulse Height Spectrum for the foreground used in the simulation. Figure 8.8 shows the Pulse Height Spectrum for the background.

For the foreground data, the two 3-step run segments were used. Data was taken from the beginning of the 2nd dip to 20 s into the last dip. For background runs, data was taken from 750 s of the holding time 100 s before the first dagger step in the counting period. All long runs taken from every run segment analyzed were used for the background measurement.

To generate a coincidence, a random pulse height for PMT 1 ( $N_1$ ) and PMT 2 ( $N_2$ ) is drawn from the PHS histogram. Then a coin is flipped to determine whether PMT 1 or PMT 2 is the start coincidence. One count is generated at  $t_{\text{coinc}} = 0$  (time relative to the coincidence start) for the PMT which starts the coincidence and the pulse height is decremented. Then ( $N_1$ ) arrival times are pulled from the appropriate PMT 1 histogram and ( $N_2$ ) arrival times are pulled from the appropriate PMT 2 histogram. These are inserted into the data. The hardware discriminator deadtime is not emulated, because the timing histograms and pulse height spectra already have that information because they were taken from real data. The interarrival time in the simulation can be less than the discriminator deadtime.

The time profile of coincidence events is generated with a nonhomogeneous Poisson process.

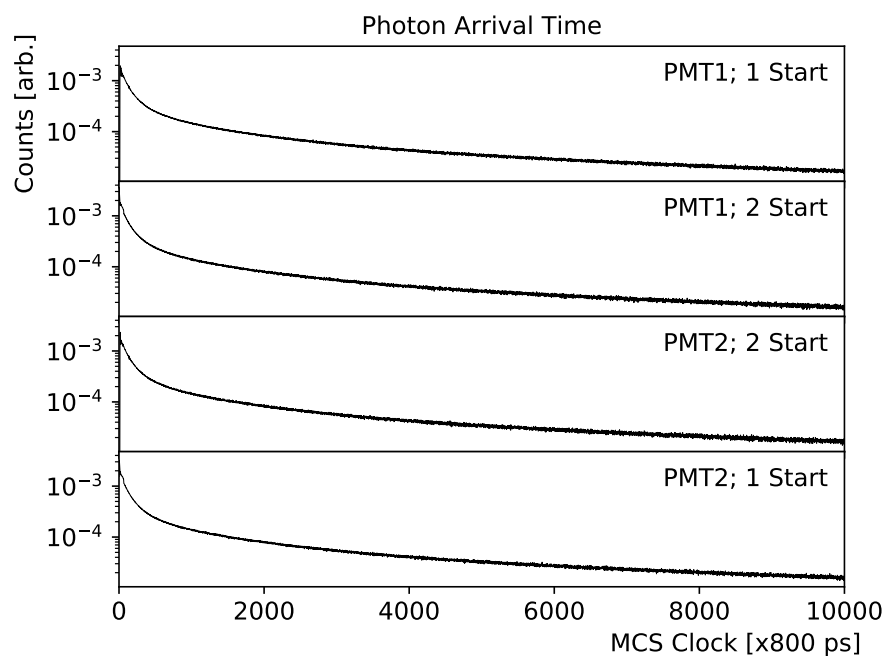


Figure 8.6: Arrival time histograms for ZnS:Ag light. From top to bottom: arrival time in PMT 1 when PMT 1 starts coincidence, PMT 1 when PMT 2 starts, PMT 2 when PMT 2 starts, and PMT 2 when PMT 1 starts.

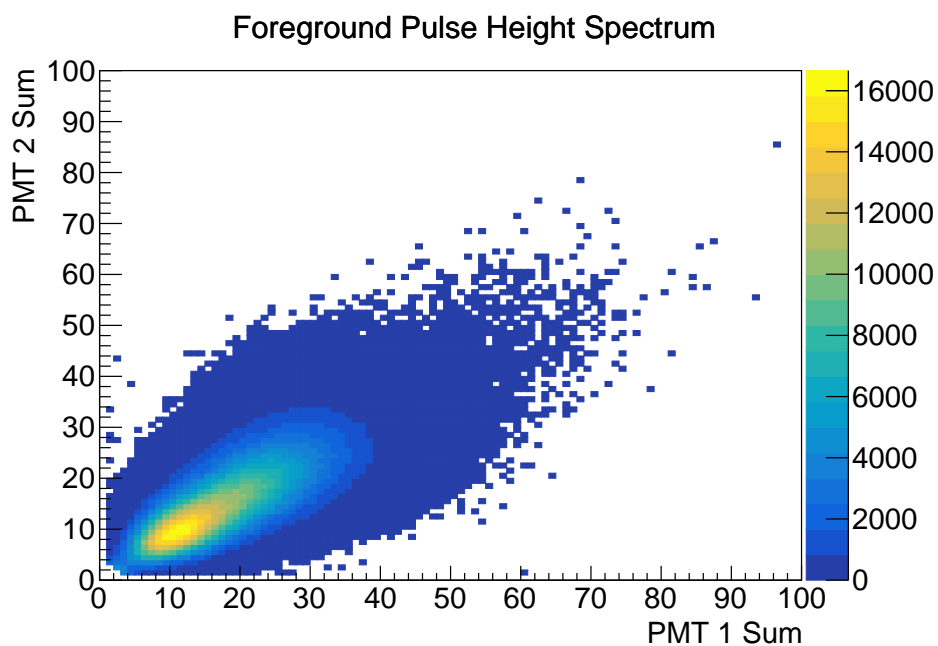


Figure 8.7: Pulse Height Spectrum for Foreground counts.

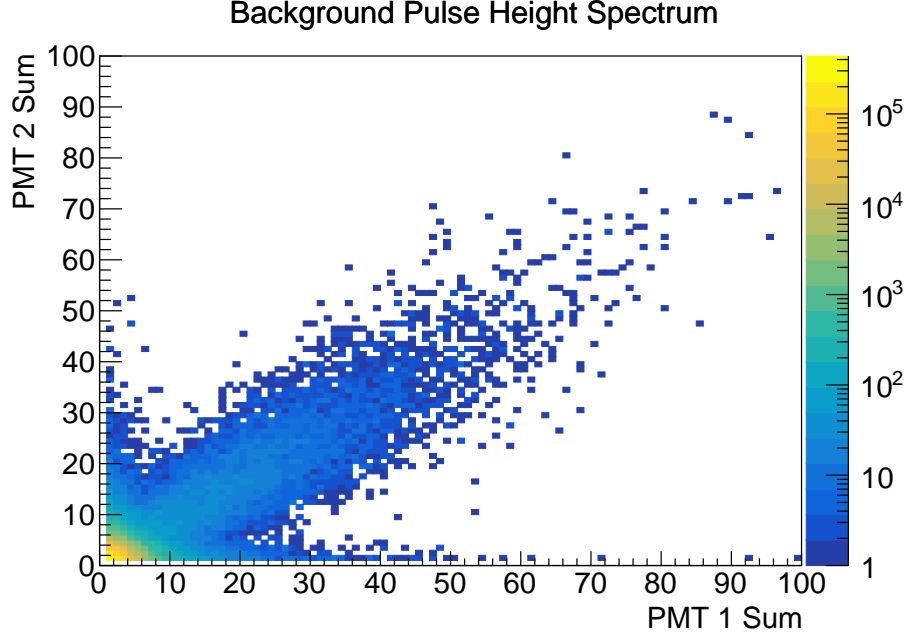


Figure 8.8: Pulse Height Spectrum for Background counts.

A nonhomogeneous Poisson process is described by a time-dependent rate function  $\lambda(t)$  [38]. One simple way to simulate a nonhomogeneous Poisson process is by thinning. The following algorithm from Lewis and Shedler describes the thinning process of a nonhomogeneous Poisson process:

#### Nonhomogeneous Poisson Process

---

$t = t_0, R > \lambda(t) \forall t > t_0$   
**While**  $t < t_{\text{end}}$ :  
 $U_1, U_2 \sim U(0, 1)$   
 $t = t - \log(U_1)/R$   
**If**  $t > t_{\text{end}}$ : **Exit**  
**If**  $U_2 < \lambda(t)/R$ : **Record Event**

Table 8.1: Prescription for Thinning Algorithm

Additionally, a homogeneous Poisson process is used for both background coincidences and dark counts. In the homogeneous case, exponential interarrival times are generated but there is no limiting rate  $R$  to compare to.



The arrival time distribution of coincidences in the counting phase of the experiment is measured from the data. The UCN counting profile is fit to single exponentials and these single exponentials give the limiting rate  $R$  in the algorithm given above.

At the end of event generation, the counts are time-ordered and given to the same coincidence routine as used in the production data.

To measure the shift in the lifetime, synthetic long and short runs are generated and analyzed as in the production data. Short runs are created with  $N_{\text{short}}$  UCN events on average, and long runs are given  $N_{\text{long}} = N_{\text{short}} e^{-T_{\text{hold}}/\tau_{\text{synth}}}$  events on average where  $T_{\text{hold}}$  is the synthetic holding time, and  $\tau_n$  is the synthetic lifetime. Comparison of the measured  $\tau_{\text{analyzed}}$  to  $\tau_{\text{synth}}$  give the predicted shift in lifetime as a function of  $N_s$  and the cuts.

### 8.5.2 RATE DEPENDENT EFFECT SIMPLIFICATION

A simplification can be made in order to speed up execution. The efficiency closely matches a linear function of time,  $\epsilon = A + BR$  where  $R$  is the rate. Given a time profile of UCN counts,  $\Phi(t)$ , the expected number of counts would be

$$N_{\text{counted}} = \int_0^{\text{end}} \epsilon(t) \Phi(t) dt = \int_0^{\text{end}} \alpha \Phi(t) + \beta \Phi(t)^2 dt. \quad (8.3)$$

The arrival time profile of UCN during counting is exponential:  $\Phi(t) = \frac{N}{\kappa} e^{-\frac{t}{\kappa}}$ , where  $\kappa$  is the time constant of counting on the main detector. Using exponential arrival time, the expected counts will be

$$N_{\text{counted}}(T_{\text{hold}}) = \sum_{\text{dips}} \alpha \left[ \frac{N e^{-T_{\text{hold}}/\tau}}{\kappa} \right] \kappa \left( 1 - e^{-\frac{L}{\kappa}} \right) + \beta \left[ \frac{N e^{-T_{\text{hold}}/\tau}}{\kappa} \right]^2 \frac{\kappa}{2} \left( 1 - e^{-\frac{2L}{\kappa}} \right), \quad (8.4)$$

where  $T_{\text{hold}}$  is the holding time,  $\tau$  is the lifetime, and  $L$  is the length of counting in a given dip.

The lifetime expected to be measured is then given by

$$\tau = \frac{T_{\text{hold}}}{\log\left(\frac{N_{\text{counted}}(0)}{N_{\text{counted}}(T_{\text{hold}})}\right)}, \quad (8.5)$$

where the error is estimated by Gaussian propagation of the errors in  $\alpha$  and  $\beta$ .

Comparison of the full Monte Carlo simulation to the simplified model shows agreement within 0.013 s. The average of differences between the full simulation and the simplified model is  $0.013 \pm 0.006$  s with the largest disagreements at high rates where nonlinear effects on the rate dependent efficiency may become more important. For rates comparable to the average rates seen in the experiment, the shift is  $0.0078 \pm 0.0055$  s with the largest deviation being 0.038 s. In the case of 9 dagger steps, the full Monte Carlo simulation and simplified simulation agree within 0.004 s.

### 8.5.3 IDENTIFICATION OF OPTIMAL CUTS

An optimal cut where  $\Delta\tau = 0$  can be identified by using Equation 8.5. Because the deadtime and pileup pull the lifetime in opposite directions, there should be points where there is no predicted rate-dependent correction. Qualitatively, the longer the integration window is, the larger the deadtime contribution is. The cut on photon number has a valley - The pileup effect is minimized for some choice of number of photons. At lower thresholds, the effect of counting extra UCN become more important and at higher thresholds, the effect of boosted efficiency due to extra photons from previous events is more important.

The point of minimum pileup effect is chosen and the window is tuned so that the shifts due to pileup and deadtime are canceled. For this analysis, the 1 dip scenario is investigated, but the point of zero  $\Delta\tau_n$  should be the same for all counting profiles because it depends on the rate dependent efficiency. Wherever the rate dependent efficiency is flat,  $\Delta\tau$  should be zero.

Figure 8.9 shows the shift in lifetime as a function of the coincidence cuts. Figure 8.10 shows the shift in lifetime as a function of the integration window for the optimal photon sum cut. A sum of 7 photons was chosen because it minimizes the derivative in the number of photons dimension. In this case, the optimum is found to be at 408.96 ns for a 7 photon cut; rounding this to the

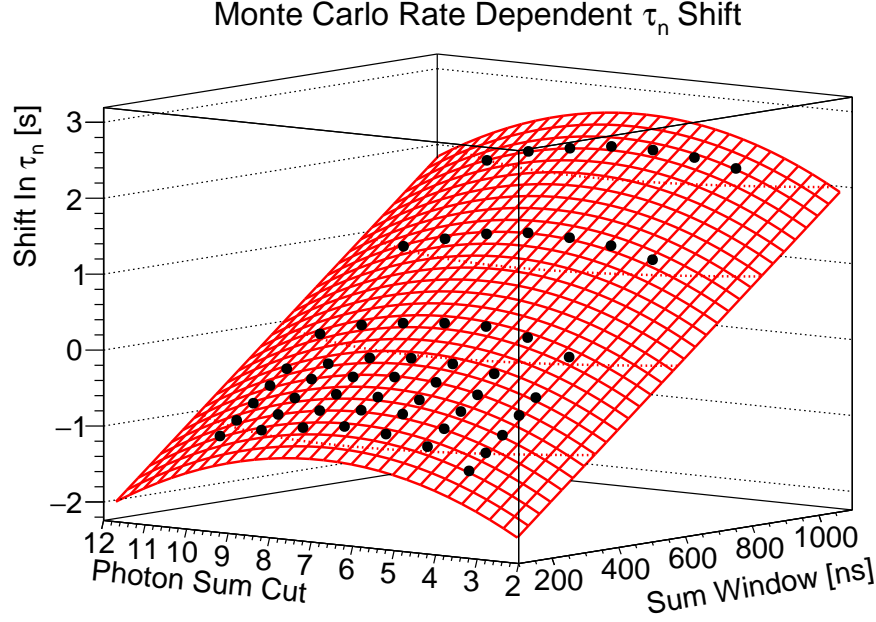


Figure 8.9: The rate dependent shift in  $\tau_n$  as a function of the photon sum threshold, and the integration window. Data was fit to  $\Delta\tau_n = \alpha + \beta N_{\text{ph}} + \lambda(T_{\text{sum}} - \mu)$  for illustrative purposes.

nearest 800 ps timestamp would give an integration window of 408.8 ns.

#### 8.5.4 INVESTIGATION OF DEADTIME EFFECTS

The deadtime correction given by Equation 8.2 is unable to properly correct for deadtime. This can be investigated by using a modified version of the simulation and analysis. To investigate the deadtime only, the pileup effect was "turned off" by tagging UCN events (the events generated by the Poisson process) with unique identification numbers. Additionally, the variable-sized integration window is replaced by a fixed-length window to simplify the deadtime calculation.

The coincidence finding routine is modified to only sum photons from one ID at a time. Because the pileup effect is caused by counting neutrons in the tail of a previous event, counting only photons from a single event will remove the effect. Simulations show that the deadtime correction overcorrects and leads to residual rate dependent effects. When the pileup is disabled and a similar cut to the optimal cut is used (7 sum threshold and a  $1500\mu\text{s}$  fixed length window), the deadtime

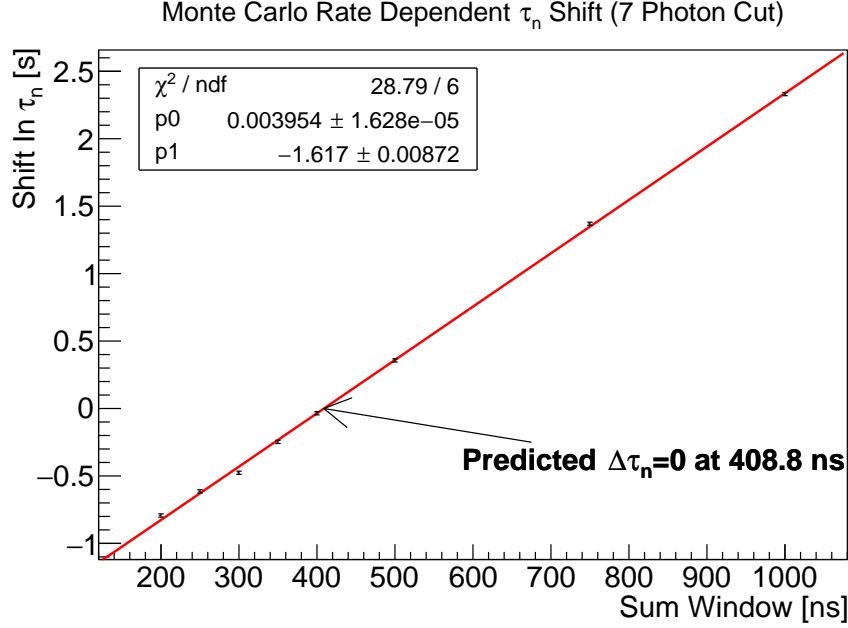


Figure 8.10: The rate dependent shift in  $\tau_n$  as a function of the integration window. Data was fit to a linear function and the fit was used to predict where  $\Delta\tau_n = 0$ .

correction given by Equation 8.2 overcorrects by  $0.22 \pm 0.01$  s.

This is caused by UCN events that begin inside the integration window of a previous event, but are still able to be counted due to photons in its tail. The deadtime correction assumes that the system is 'dead' for that time and any event that begins inside the deadtime cannot be counted, and so over-estimates the correction. This phenomenon can be turned off in the simulation by keeping a list of UCN event IDs that begin inside of the deadtime of a previous event and ignoring subsequent photons from that UCN event. In that way, the system guarantees that the deadtime is truly dead. Using the same cuts and this scheme, the deadtime undercorrects by  $0.07 \pm 0.01$  s, showing that the deadtime correction given by Equation 8.2 does not work without knowledge of which pulse came from which UCN.

Due to the inability for Equation 8.2 to correct for deadtime in the detector system, only the simulation can disentangle the effects of deadtime and pileup. When coincidences are used for analysis, the optimal cuts identified in the previous section are used and no correction is made for

rate-dependent effects. Coincidence analysis is not used to measure the lifetime because of the size of corrections possible when using coincidences.

## CHAPTER 9

### NORMALIZATION

#### 9.1 INTRODUCTION

The bottle method of measuring the neutron lifetime does not need absolute measurements of the detector efficiencies or the populations; however, a relative measurement of the initial population is needed. Between a short and a long run, the source production can change dramatically both in strength and energy distribution. The source flux degrades over time. The deuterium crystal accumulates cracks, contamination, and layers of low-density snow which cause reduced output and spectral distortions.

Several monitor detectors are installed on UCN $\tau$  to monitor both the flux and the spectrum coming from the source. These monitor detectors are  $^{10}\text{B}$  coated ZnS:Ag detectors viewed directly by a PMT. The signal is integrated, shaped, and discriminated by analog electronics and counted in the same MCS unit that measures the main *in situ* detector.

The counts from the detectors are used for normalization of the relative UCN densities, spectral correction, and filtering of "bad" runs.

#### 9.2 DESCRIPTION OF DETECTORS

The UCN $\tau$  system has the following monitor detectors:

- "old monitor" - A pinhole monitor before the UCN gate valve
- "bare monitor" - A smaller pinhole monitor before the UCN gate valve

- "foil monitor" - A monitor built to be identical to the bare monitor, but with an aluminum window to block low energy UCN
- "standpipe monitor" - A monitor on the guide system after the adiabatic fast-passage spin flipper; set to a height above the cleaner to monitor high-energy UCN
- 3 addition standpipe monitors which are pinholes in the standpipe guide
- "downstream monitor" - A monitor behind the UCN loading door

The standpipe monitor (SP) gives the highest rate and is always used to measure the trap population. One of either the bare (BA) or old (OL) monitor is used as well. The additional standpipe monitors have low rate and are unused in this analysis. The downstream monitor also has a low rate and is thus unused. The downstream monitor is interesting as a check for drained UCN after the trapdoor is opened at the end of a run.

Several detectors had multiple pulses per UCN. In the standpipe detector, the contamination of errant pulses was as high as 20%. A uniform 20  $\mu$ s deadtime was imposed on the monitor detectors to eliminate multiple pulsing. The same deadtime correction used for individual photon counts in the main detector was used to correct the monitor counts.

### 9.3 RUN FILTERING

Occasionally, runs have filling periods where the flux from the source drops unexpectedly. This can be due to dropped proton pulses from the accelerator, or unexpected increases of the pressure near the source. These runs can be filtered out so that only runs with similar filling conditions are used.

The arrival time of UCN on the standpipe monitor is used to measure run quality. The arrival time is fit to the function

$$\Phi(t) = \sum_i \phi_i (1 - e^{-(t-T_i)/\kappa_1}) e^{-(t-T_i)/\kappa_2}, \quad (9.1)$$

where  $\phi_i$  is the strength of an individual pulse,  $T_i$  is the time offset for a given pulse,  $\kappa_1$  is the saturation time constant, and  $\kappa_2$  is the decay time constant.  $\kappa_1$  and  $\kappa_2$  are measured by fitting Equation 9.1 and keeping them as free parameters; in 2016-2017  $\kappa_1 = 0.4$  s and  $\kappa_2 = 24.75$  s. The time offsets were given by  $T_i = T_{\text{H-GX}} + 3$  s where  $T_{\text{H-GX}}$  is the arrival time of proton pulses on the tungsten target and the additional 3s accounts for travel time from the source to the monitor. Figure 9.1 shows an example of a fitted arrival time histogram from a single run.

The beam was run in 2 different patterns. Approximately the first half of the 2016-2017 data was taken with 10 proton pulses every 5 s. Subsequent runs used 18 or 19 pulses every 10 s. This affects the total number of pulses during the 150 s filling period and the spacings between bursts of UCN seen in the monitors.

Bad runs are filtered out by looking at the distribution of  $\phi_i$  for the fill. Because of the small number of observations, a test based on medians was chosen. The test uses a modified Z-score test statistic to determine the presence of outliers [39, §1.3.5.17]. The test statistic is

$$M_i = \frac{0.6745(x_i - \tilde{x})}{\text{MAD}} \quad (9.2)$$

$$\text{MAD} = \text{median}(|x_i - \tilde{x}|),$$

where tilde denotes the median and MAD is the median absolute deviation [from the median].

For a given run, the  $M_i$  was calculated for each  $\phi_i$ , and the maximal  $M_i$  was used to test the farthest outlying pulse. Exceptions were made where the MAD was more than 10% of the median; in some runs the dispersion in pulse heights was so high that it affected the use of MAD in normalizing the test statistic.

The first UCN pulse was observed to have a systematically stronger  $\phi$  than subsequent pulses. To avoid the early pulses causing false positive outliers, the maximal  $M_i$  was calculated separately for all  $i$  and again for  $i > 2$  (when using 10 s beam spacing) or  $i > 4$  (when using 5 s beam spacing).

Visual inspection of the distribution of  $M_i$  led to imposing cuts of 20 for every pulse and 7 for the tail; these cuts did not change during the analysis. Figure 9.2 shows the distribution of  $M_i$  for



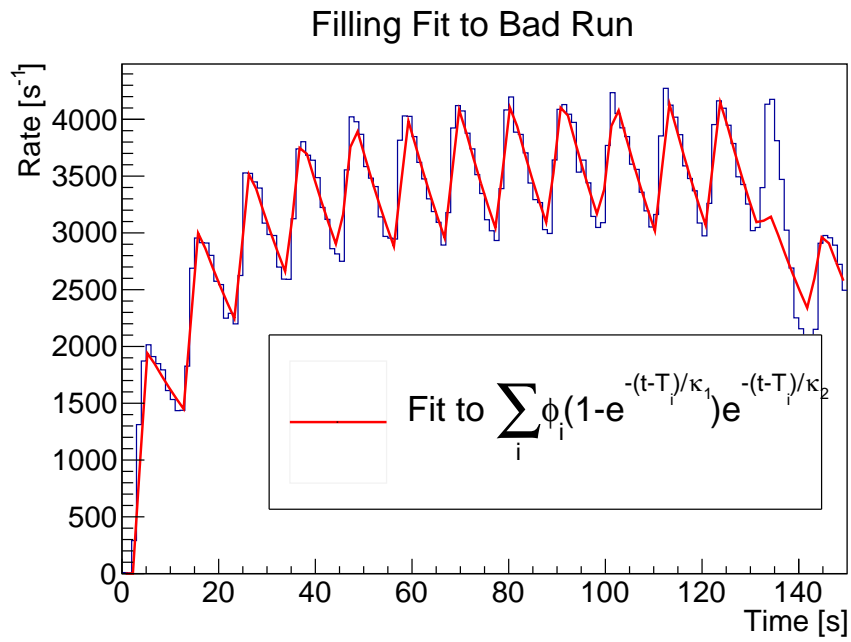
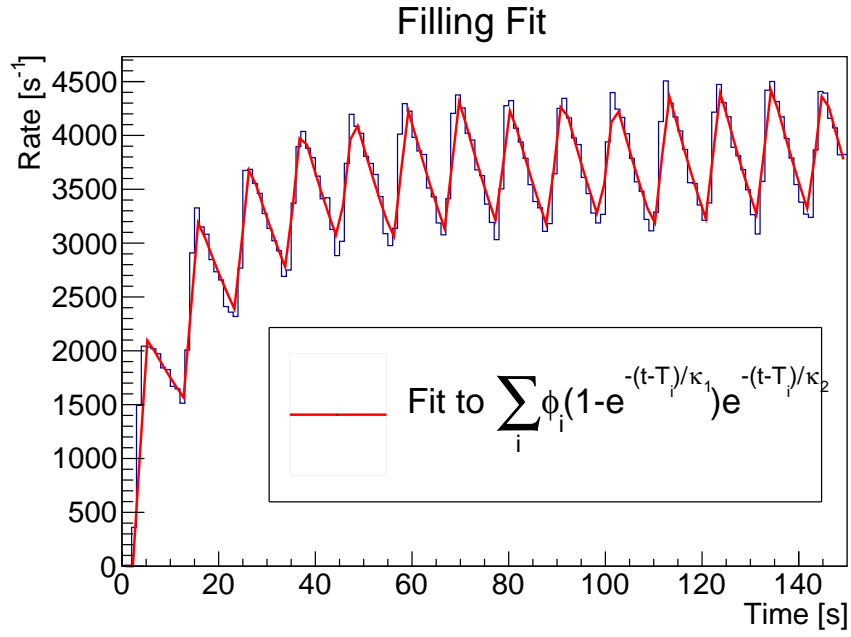


Figure 9.1: Filling fits to Equation 9.1.

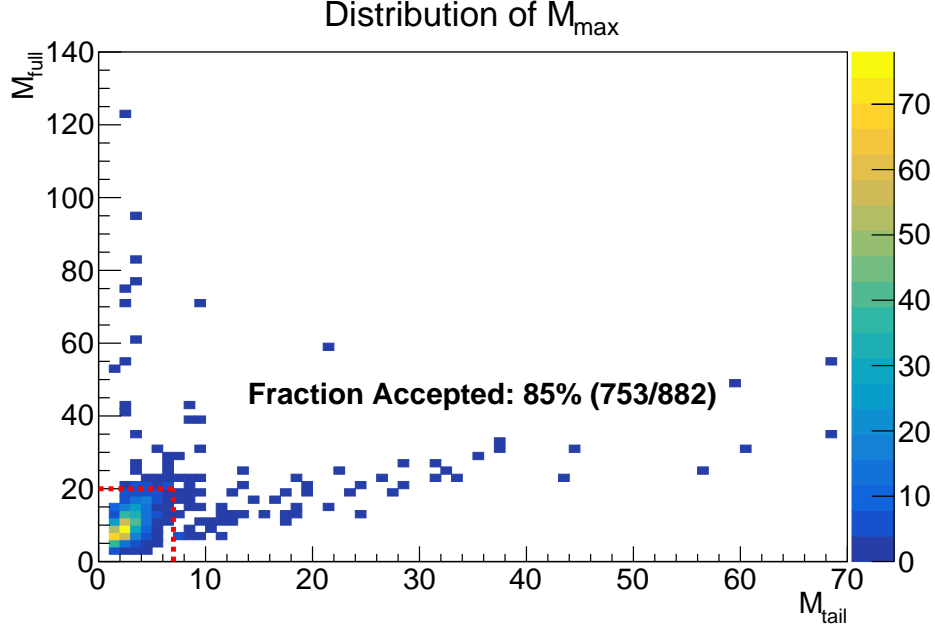


Figure 9.2: Distribution of  $M_i$  in the tail and the full fill for production runs. Red line shows acceptance cuts. Acceptance was 85%.

all production runs.

## 9.4 RUN PAIRING

The source output fluctuates significantly over the course of days as seen in Figure 9.3a. To mitigate the effects of changing source conditions, the lifetime was measured in separate trials where the short and long runs were taken close in time. Runs were paired with an automatic pairer. The algorithm is given below:

$M$  is the maximal  $M$  score,  $SP$  is the standpipe rate,  $\Delta T$  is the holding time, and  $T$  is the start time of the run in unix time. A time difference test was added to avoid pairing runs that are far apart in time; evolution of the source may cause problems in normalization if they are separated by too long. Runs were only paired if they were taken within 4 hours. The flux is also compared and if the rate is too different, the runs are not paired. If the ratio of  $\frac{M_1}{M_2}$  or  $\frac{M_2}{M_1}$  (defined later) is less than 0.9 the pairing is rejected.

---

**Algorithm 9.1** Prescription for Run Pairing.

---

**procedure** RUN PAIRING

**for all**  $i < N$  **do**

**if**  $(M_{\text{tail},i} < 7) \ \& \ (M_{\text{full},i} < 20)$  **then**

**for all**  $j \neq i$  **do**

**if**  $(M_{\text{tail},j} < 7) \ \& \ (M_{\text{full},j} < 20) \ \& \ (|\Delta T_i - \Delta T_j| > 500) \ \& \ \left(\frac{\text{SP}_i}{\text{SP}_j} \not\prec 0.9\right) \ \& \ \left(\frac{\text{SP}_j}{\text{SP}_i} \not\prec 0.9\right) \ \& \ |T_i - T_j| < 14400$  **then**

                    Pair  $i, j$  and remove

---

## 9.5 EXPONENTIAL WEIGHTING

UCN bursts from the source that arrive closer to the time when the trapdoor is closed are more important in the normalization. A UCN pulse that arrives long before the trapdoor is closed will eventually drain from the trap. Over many pulses, the density inside the trap trends toward saturation, and the most recent pulses contain the most information about the density inside the trap. The trapped number of UCN tends to follow

$$N_{\text{trapped}} = N_{\text{max}} \left(1 - e^{-t/\kappa}\right), \quad (9.3)$$

where  $N_{\text{max}}$  is the saturated population, and  $\kappa$  is the saturation time constant.

The normalization needs to estimate the density in the trap,  $\hat{N}_{\text{trapped}}$ . When integrating the monitor rates Equation 9.3 needs to be recovered. If a constant flux  $\Phi$  is considered, then one density estimate is

$$\hat{N}_{\text{trapped}} = \gamma \int_0^T \Phi e^{(t-T_{\text{end}})/\kappa}, \quad (9.4)$$

where  $\Phi$  is the UCN flux,  $\gamma$  is some constant that determines the proportionality between a flux measurement and a number measurement, and  $T_{\text{end}}$  is the length of the filling period during which UCN can enter or exit the trap through the entrance. This recovers the expected saturation

behavior from a uniform UCN flux. For the data,  $\Phi$  is replaced by the counts seen in monitor detectors and a sum is taken over each count instead of an integral:

$$\hat{N}_{\text{trapped}} = \gamma \sum_i \frac{1}{\kappa} e^{(t_i - T_{\text{end}})/\kappa} = M, \quad (9.5)$$

where  $M$  is a weighted monitor signal, e.g.,  $M_{\text{SP}}$  is the weighted signal from the standpipe.

The time constant,  $\kappa$ , was determined experimentally in 2014 by fitting the loading time constant of the trap. The time constant  $\kappa$  was found to be 70 s.

## 9.6 SPECTRAL EVOLUTION

The spectrum of UCN exiting the source varies substantially from the initial freeze-in of the deuterium crystal to the last production run before remaking the source. Additionally, the spectrum is different between builds of the source. Changes in deuterium shape, source gas pressure and composition, defects in the deuterium crystal, or contaminants can affect the spectrum.

For a perfect normalizer, the quantity  $N_{\text{UCN}}/M_{\text{SP}}$  (the normalized UCN counted after storage over the weighted monitor) should fluctuate around a central value and not be correlated to source conditions. However, because the trap selects only part of the UCN spectrum from the source and the spectral acceptance of the monitors and the trap is different,  $N_{\text{UCN}}/M_{\text{SP}}$  correlates with source conditions and affects the ability to properly normalize the data. This can be seen in Figure 9.3a.

## 9.7 SPECTRAL CORRECTION

Some corrections can be made to improve the normalization performance. Because several monitor detectors are used, they can be added so that their sum can balance out the spectral drift. The normalization then becomes

$$M = \alpha \times M_{\text{SP}} + \beta \times M_{[\text{OL/BA}]}, \quad (9.6)$$

where  $\alpha$  and  $\beta$  are constants determined by a linear regression where  $N_{\text{counted}} = \alpha \times M_{\text{SP}} + \beta \times M_{[\text{OL/BA}]}$ .

The linear regression is done using the scipy scientific computing framework independently for each running condition. A cross-segment regression is not done because each run segment could have a different spectral dependence due to the counting and cleaning conditions. Figure 9.3b shows the result of applying this normalization to the data from Figure 9.3a.

The correction is not perfect - the trap population cannot be predicted sufficiently from the monitor detectors to give the expected distribution in most run segments. However, the correction does improve the normalization and in some cases is sufficient. Table 9.1 shows the  $\frac{\chi^2}{\text{NDF}}$  for the run sets analyzed in 2015-2016 and 2016-2017. The token "GC" is the usage of the giant cleaner, "AC" the active cleaner, "DC" is deep cleaning with the dagger detector, and the full/half field is the holding field.

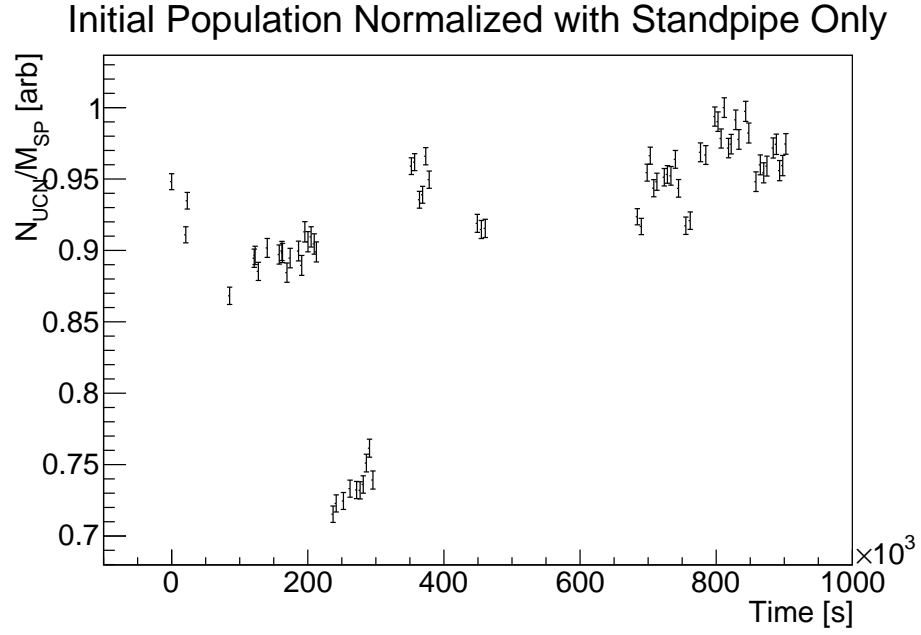
## 9.8 SOURCE PARAMETERS

Conditions in the source may affect normalization. For example, the temperature of the solid deuterium crystal may affect the production in a way which is not captured by the spectral correction applied from Equation 9.6.

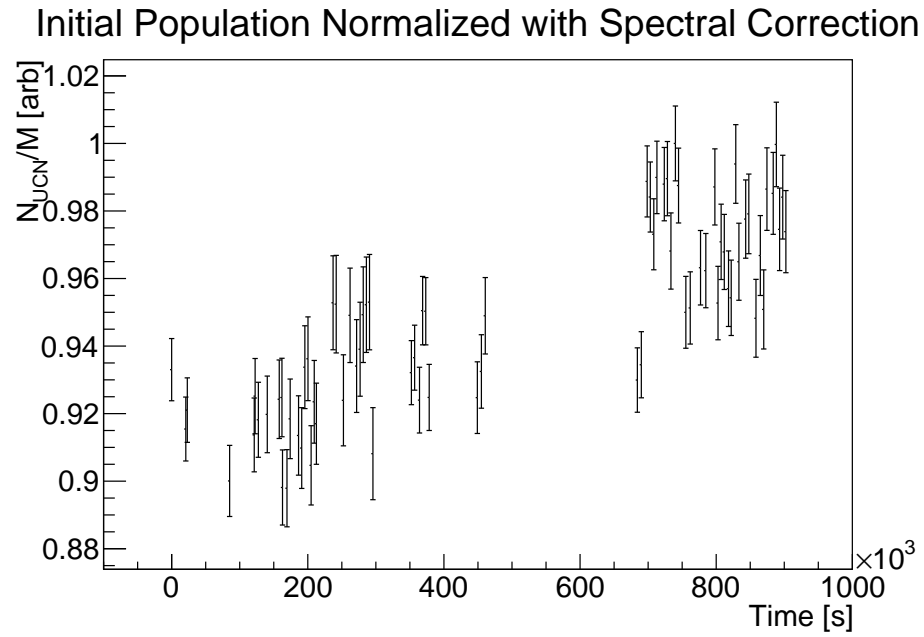
In the 2016-2017 dataset, a large number of source parameters were recorded into a MySQL database. Each measurement was taken roughly every few seconds, up to every 10s depending on sensor equipment limitations. The measurements of most interest to UCN production are listed in Table 9.2.

For the target temperature, deuterium temperature, moderator temperature, and source pressure both the average value during the filling time when beam was on target, and the maximum value during the run are reported. For the trap pressure, the average pressure during the run is reported.

Figure 9.3b shows some residual correlation of the normalization which is unexplained by the



(a) Spectral variation in normalized trap population as a function of time.



(b) Corrected normalized trap population as a function of time.

Figure 9.3: Comparison of no spectral correction to the correction in Equation 9.6

Run Set	$\frac{\chi^2}{\text{NDF}}$	NDF
<b>2015-2016</b>		
300s Clean 4 Dip NoGC AC DC	1.6	81
100s Clean 1 Dip NoGC AC DC	4.1	34
100s Clean 1 Dip NoGC AC DC	2.5	72
100s Clean 1 Dip NoGC AC DC	1.0	35
100s Clean 1 Dip NoGC AC DC 200s Hold	1.1	23
100s Clean 4 Dip GC AC NoDC	1.4	28
100s Clean 4 Dip GC AC DC	1.0	12
200s Clean 4 Dip GC AC NoDC	1.9	23
<b>2016-2017</b>		
200s Clean/1 Dip	6.1	72
200s Clean/9 Dip	7.4	53
300s Clean/9 Dip	2.1	55
50s Clean/Full Field	1.6	67
50s Clean/Half Field	1.6	60

Table 9.1:  $\frac{\chi^2}{\text{NDF}}$  of the Normalization, assuming that  $N_{UCN}/M$  should be normally distributed about its mean

Measurement	Description
Normalized UCN detected	Sum of UCN normalized with 2 monitors
Target temperature	Average of sensors near tungsten target
Deuterium temperature	Average of sensors on cryostat
Moderator temperature	Average of sensors near polyethylene beads
Source pressure	Pressure inside deuterium volume
Trap pressure	Average pressure inside trap
Time	Time and date that run was taken

Table 9.2: Description of peripheral source measurements

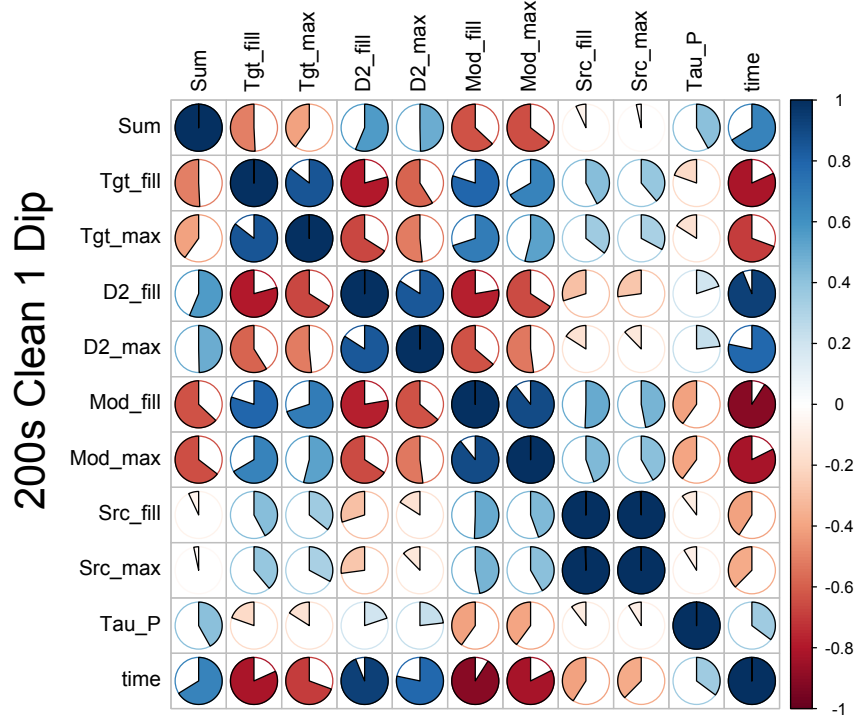


Figure 9.4: Correlation matrix for 200s Clean/1 Dip set.

monitor detectors. The correlation between the normalized number of UCN and each of the source parameters can be investigated to determine if a significant relationship exists.

Figures 9.4 to 9.8 show the correlation matrix of the described parameters.

These plots show the correlation between any 2 of the described measurements. Going from one row to one column shows the correlation between those measurements. Blue represents positive and red represents negative; the amount of circle filled in is the correlation coefficient.

The most important row is the first, which shows the correlation between the normalized sum and various source parameters. The final column shows the correlation of source parameters with time.

There is no consistent and strong correlation between the normalized population and any source parameter. The first dataset contains high correlation coefficients, but the highest is with time. Additionally, all of the parameters are correlated strongly with time.

The correlation present in the most number of datasets is the correlation between the normalized



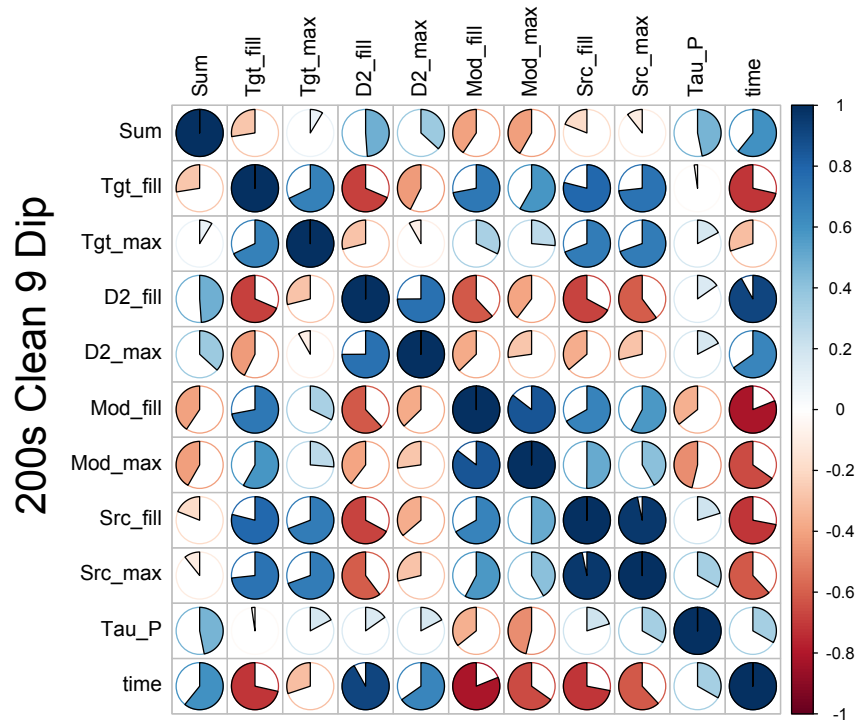


Figure 9.5: Correlation matrix for 200s Clean/9 Dip set.

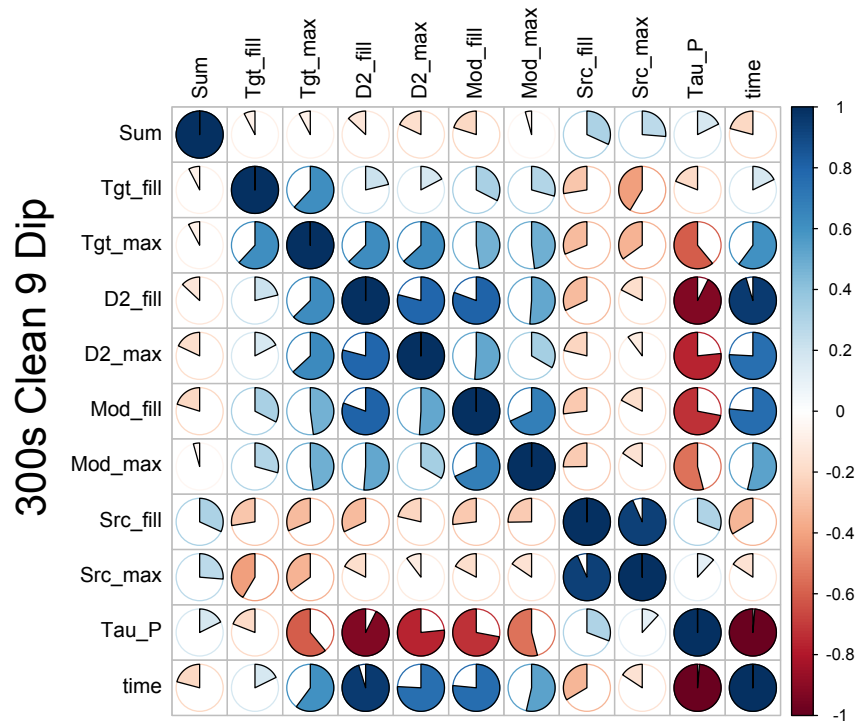


Figure 9.6: Correlation matrix for 300s Clean/9 Dip set.

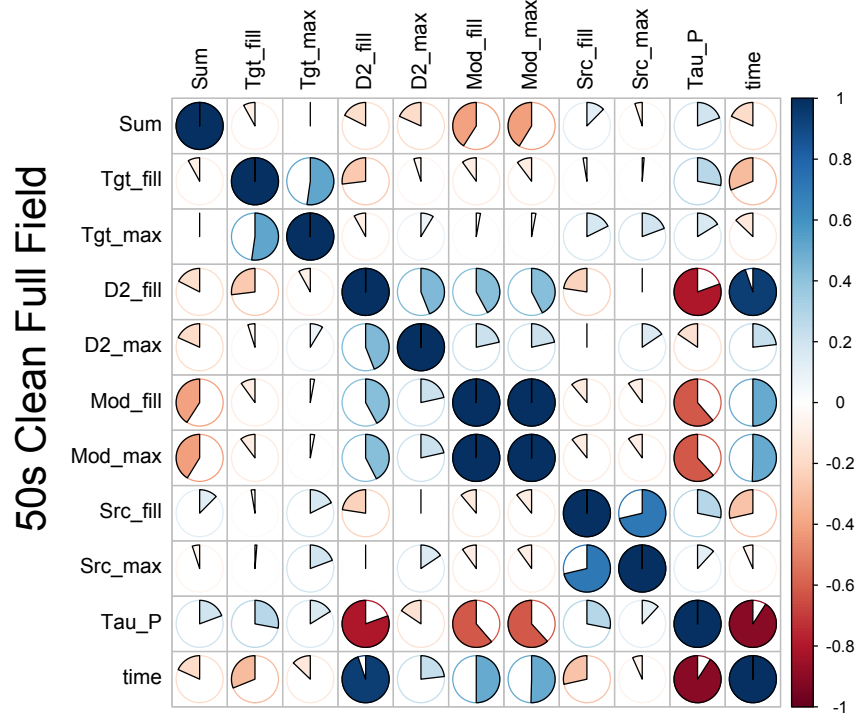


Figure 9.7: Correlation matrix for 50s Clean/Full Field set.

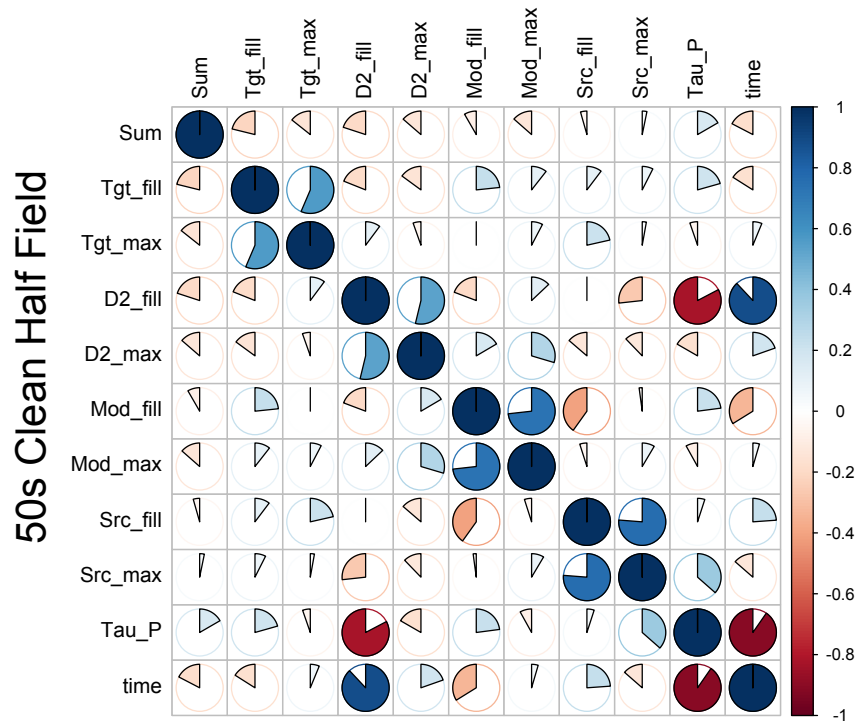


Figure 9.8: Correlation matrix for 50s Clean/Half Field set.

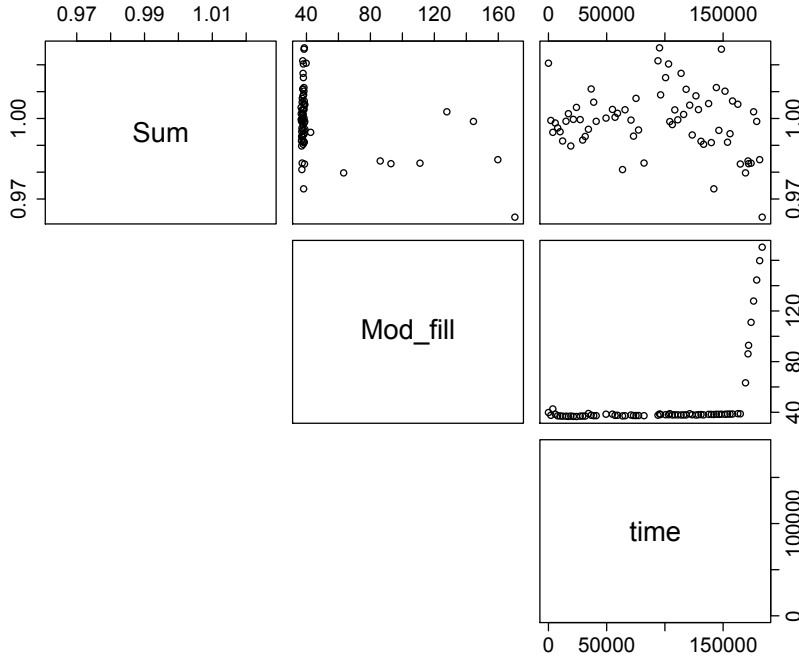


Figure 9.9: Scatter plot of normalized number, moderator temperature, and time for 50s Clean/Full Field set.

number and moderator parameters. However, in 2 run sets that relationship does not show up. In the 50s cleaning full field dataset (which did contain this correlation), the moderator temperatures were consistent until the end of the run set, where the temperature increased over several runs by 400%. Figure 9.9 shows scatter plots of the normalized number, moderator temperature during filling, and time. The increase in temperature did not have a strong effect on the normalization, so there may not be a significant relationship.

The relationship between the normalized population, moderator temperature, and time in the 200s cleaning 1 step dataset show a significantly larger correlation than the 50s cleaning dataset. This is shown in Figure 9.10. The average temperature of the moderator is significantly lower, but the large correlation in this dataset and the lack of it in the 50s cleaning dataset suggests that the correlations may just be accidental.

The correlation in the first two datasets may be related to aging of the new source. These

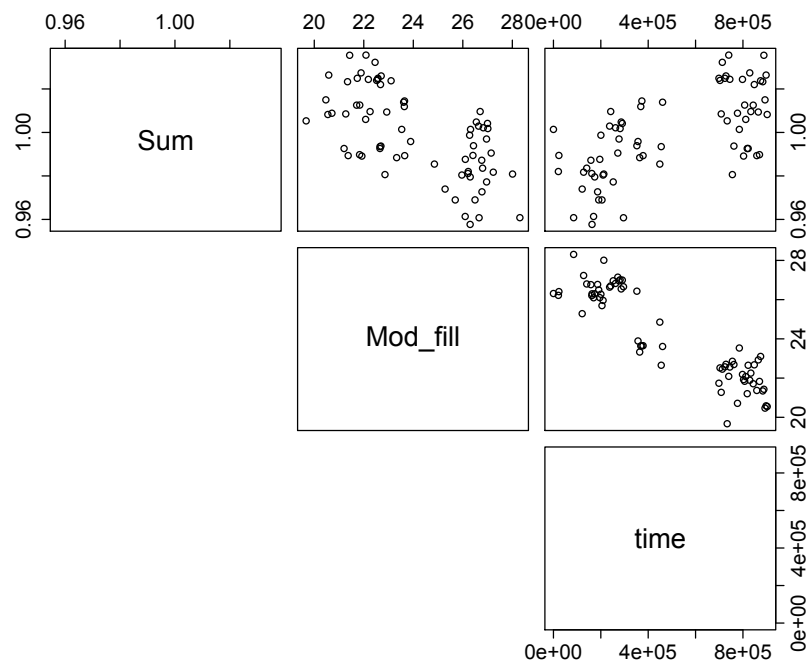


Figure 9.10: Scatter plot of normalized number, moderator temperature, and time for 200s Clean/1 Dip set.

datasets were taken after an initial short dataset and were the first major datasets taken with the new source in production. Gas species in the guide being pumped out, contamination of the deuterium, or para/ortho fraction may cause changes in the production, but were not tracked. The learning period of using the new source may also contribute significant correlations with time.

Later datasets show no large trends in normalization as a function of source parameters, so these parameters are not used in the analysis. Only monitor detector counts are used to correct for spectral changes in the source production.

## CHAPTER 10

### LIFETIME CALCULATION

#### 10.1 EXPONENTIAL DECAY

Neutrons decay with a mean lifetime,  $\tau_n$ :

$$N_n(t) = N_{n,0}\exp(-t/\tau_n). \quad (10.1)$$

One convenient way to extract  $\tau_n$  is to take pairs of observations at different points in the exponential decay curve:

$$\begin{aligned} N_{n,l} &= N_{n,0}\exp(-T_l/\tau_n) \\ N_{n,s} &= N_{n,0}\exp(-T_s/\tau_n) \end{aligned} \quad (10.2)$$
$$\tau_n = \frac{\Delta T}{\log(N_{n,s}/N_{n,l})},$$

where  $N_{n,l}$  is the number of neutrons (or a signal proportional to the number) in a 'long' run where UCN are held on the order of 1000 s,  $N_{n,s}$  is the number of neutrons in a 'short' run where UCN are held for less time,  $T_l$  and  $T_s$  are the long and short holding times, and  $N_{n,0}$  is the initial population.

$N_{n,0}$  could fluctuate before each measurement, so  $N_{n,l}$  and  $N_{n,s}$  are normalized by measuring the production of the UCN source

$$\tau_n = \frac{\Delta T}{\log(\frac{N_{n,s}}{M_s} / \frac{N_{n,l}}{M_l})}, \quad (10.3)$$

where  $M_s$  and  $M_l$  are normalization quantities measured with UCN monitors while the trap is filling.  $M_s$  and  $M_l$  are described in detail in Section 9.7 and are given by

$$M = \alpha \times M_{\text{SP}} + \beta \times M_{[\text{OL/BA}]}, \quad (10.4)$$

where  $M_{\text{SP}}$ , is the weighted standpipe monitor sum during filling,  $M_{[\text{OL/BA}]}$  is either the weighted sum of the old or bare monitor, depending on which monitor was operating correctly,  $\alpha$  and  $\beta$  are coefficients determined by linear regression between  $M_{\text{SP}}$ ,  $M_{[\text{OL/BA}]}$ , and  $N_{n,[l/s]}$ . The first two datasets are normalized with the bare detector because there were some inconsistencies in the old detector. The remaining 3 datasets (300s cleaning and 50s cleaning) were normalized with the old monitor.

The number of neutrons,  $N_{n,[l/s]}$ , is determined as follows:

$$N_n = \sum_{i=1}^{N_{\text{dip}}} \left( \sum_{t=T1_i}^{t=T2_i} + \text{DT}_i - (T2_i - T1_i) \times (R_{\text{BKG}} + \Delta R_{\text{BKG}}(h_i)) \right), \quad (10.5)$$

where the outer sum is taken over the number of dips in the run (1, 2, or 8 where the cleaning check dip is ignored).  $T1$  and  $T2$  are the beginning and ending times of the dip, the inner sum is the integral of counts in the dip,  $\text{DT}_i$  is the deadtime correction,  $R_{\text{BKG}}$  is the background measured either at the end of the run or at the cleaning check step (for 300s cleaning data),  $\Delta R_{\text{BKG}}(h_i)$  is the background rate difference due to height, and  $h_i$  is the height of the  $i$ th step. The deadtime correction and background subtraction are described in detail in Section 8.4 and Section 8.3 respectively.

$\Delta T$  is given by

$$\Delta T = \bar{T}_s - \bar{T}_l, \quad (10.6)$$

where  $\bar{T}_s$  and  $\bar{T}_l$  are the mean arrival time of counts for the long and short run.

The mean arrival times are measured by taking the average arrival time of UCN events during the counting phase of the experiment and subtracting off the average arrival time of the expected background signal. This is described in detail in Section 11.5.  $T_s$  and  $T_l$  are defined by the time between the last proton pulse from the source before the end of filling to the mean arrival time of the UCN detection after the holding time has expired ( $\bar{t}_{\text{count}} - T_{\text{End}}$ ). This is to help correct for any variations in timing and phase space evolution which may cause a shift in the mean arrival time. Coincidence counts are used for this calculation.

## 10.2 OPTIMIZATION OF HOLDING TIMES

There exists an optimal holding time, in terms of the statistical uncertainty on the final lifetime value given a fixed running time of the experiment. For simplicity, the total number of UCN from all short runs and the total number of UCN from all long runs are summed up into two quantities

$$N_l = \frac{\sum_i N_{l,i}/M_i}{\#_l} \quad N_s = \frac{\sum_i N_{s,i}/M_i}{\#_s}. \quad (10.7)$$

The lifetime is given by Equation 10.2 where  $N_{n,s}$  and  $N_{n,l}$  are replaced by  $N_s$  and  $N_l$ , which are normalized and averaged over the number of runs  $\#_s$  or  $\#_l$ .  $N_{s,i}$ ,  $M_i$ , and  $N_{l,i}$  obey Poisson statistics. The central limit theorem allows the uncertainty in  $N_s$  and  $N_l$  to be treated as Gaussian because they are sums over many runs. Short holding time runs will take a fraction,  $f_s$ , of the total running time  $T$ . Each short run will take  $t_0$  seconds, which represents filling, cleaning, and counting. Each long run will take  $t_0 + \Delta t$  seconds, where  $\Delta t$  is the holding time. Equation 10.2 can be written as

$$\tau = \frac{-\Delta t}{\ln(R \pm \delta R)}, \quad (10.8)$$

where  $R$  is the ratio of  $N_s$  to  $N_l$ . Using Gaussian error propagation for the log and simplifying, it becomes



$$\tau = \tau \pm \frac{\tau^2}{\Delta t} \frac{\delta R}{R}. \quad (10.9)$$

The number of long and short runs are given by

$$\#_l = \frac{T \times (1 - f_s)}{t_0 + \Delta t} \quad \#_s = \frac{T \times f_s}{t_0}. \quad (10.10)$$

Assuming the mean number of UCN counted are the same across runs,  $N_s$  and  $N_l$  are (approximating with Gaussian statistics) given by

$$N_l = \frac{N_{l,i}}{M_i} \pm \frac{N_{l,i}}{M_i} \sqrt{\frac{(1/N_{l,i} + 1/M_i)}{\#_l}} \quad N_s = \frac{N_{s,i}}{M_i} \pm \frac{N_{s,i}}{M_i} \sqrt{\frac{(1/N_{s,i} + 1/M_i)}{\#_s}}; \quad (10.11)$$

combining,

$$\frac{\delta R}{R} = \sqrt{\frac{1/N_{l,i} + 1/M_i}{\#_l} + \frac{1/N_{s,i} + 1/M_i}{\#_s}}; \quad (10.12)$$

substituting in  $N_{l,i} = N_{s,i} \exp(-\Delta t/\tau)$  and simplifying,

$$\delta \tau = \tau^2 / \sqrt{T} * 1/\Delta t \sqrt{\frac{\frac{1}{N_{s,i} \exp(-\Delta t/\tau)} + \frac{1}{M_i}}{\frac{1-f_s}{t_0 + \Delta t}} + \frac{\frac{1}{N_{s,i}} + \frac{1}{M_i}}{\frac{f_s}{t_0}}}, \quad (10.13)$$

which can be optimized in terms of the fraction of time allotted to short runs,  $f_s$ , and the holding time  $\Delta t$ .

The following values are assumed to be representative of ordinary running conditions:

- $\tau = 880$
- $T = 350000$  (4x24 hr run periods)
- $N_{s,i} = 20000$  (20000 UCN counts)
- $M_i = 100000$  (100000 counts in a normalizing detector)
- $t_0 = 460$  (450 s for filling(150), cleaning(100), detection(200) + 10s of waiting)

The optimal conditions are then  $f_s = 0.195$  and  $\Delta t = 1846$  s. A contour plot can be seen in Figure 10.1. This corresponds to about 20% more short runs than long runs. The amount of statistics given up for doing equal numbers is fairly small; The 2-dimensional scenario gives a minimum of  $\delta\tau = 0.953$  s whereas assuming equal numbers and only minimizing in  $\Delta t$  gives  $\delta\tau = 0.956$  s at  $\Delta t = 1869$  s. Taking runs in equal numbers is simpler logistically and allows for calculating lifetime values using adjacent pairs. Calculating  $\tau_n$  with adjacent pairs may help account for source spectral fluctuations; in the time between two paired runs the normalization will be more stable than across the entire set of runs.

Unfortunately due to problems with the data acquisition hardware, runs were limited to 1759 s ( $2^{41}$  clock cycles at 800 ps per clock). Therefore the long runs were made as long as possible given the timing limitations and the desired run structure. This typically meant that holding times were 1000 to 1400 s.

### 10.3 STATISTICAL BIAS

Averaging a large number of low statistics data can lead to biases, especially when the average is weighted. The statistics of Equation 10.3 can be modeled as a ratio of two binomial processes. The UCN source produces some large population, and each of those UCN has a small probability of reaching the trap. Then each of those UCN has some probability of decaying inside the trap and then being detected. Confidence intervals for the ratio of two binomial numbers has been studied extensively. A large number of estimates for confidence intervals exist, but they are not exact and in some places over or underestimate the uncertainty [40] [41]. Additionally, no unbiased estimator for the ratio of two Poisson numbers exists [42].

Due to the difficulty in evaluating uncertainty and the lack of unbiased estimates, final lifetime values are calculated by measuring a lifetime for each short/long pair, taking the mean of the lifetimes for each cleaning condition, and taking  $\sigma/\sqrt{N}$  for the uncertainty of each cleaning condition.

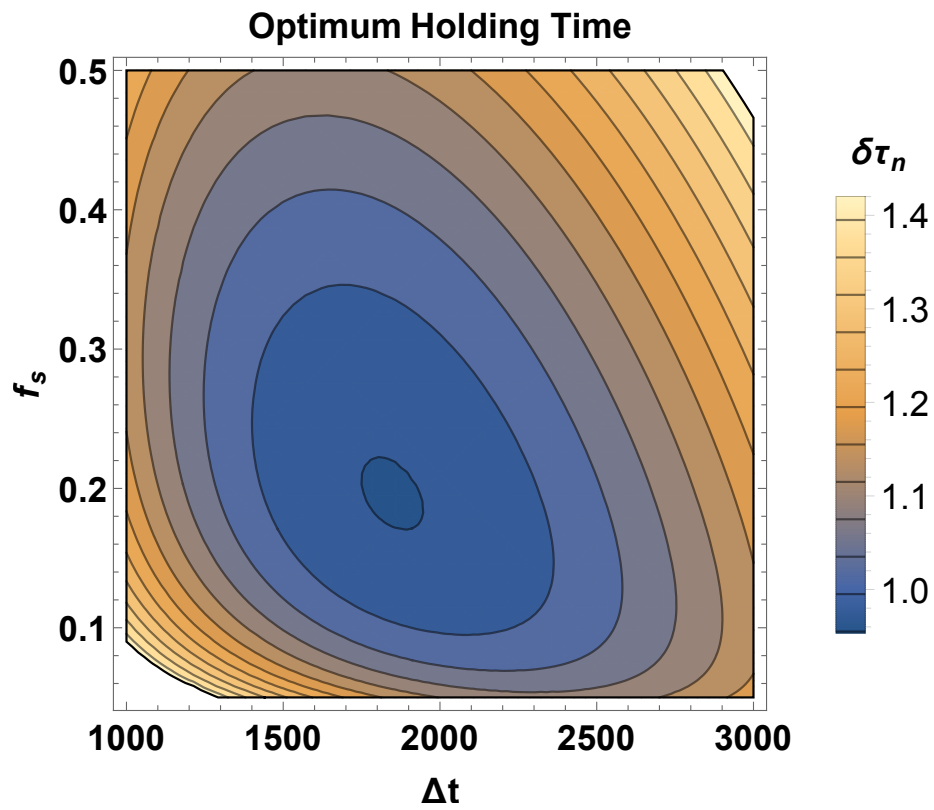


Figure 10.1: Statistical uncertainty in  $\tau_n$  given an assumed number of UCN measured per run and an assumed run length

Monte Carlo simulations show that the bias from taking weighted means assuming Gaussian statistics can be significant. Assuming a model where the initial population is given by a Poisson distributed number (this assumes the rate of UCN filling the trap is constant) and  $\beta$  decay is modeled by the binomial distribution where the number of trials is the initial population and the probability of success (survival) is  $e^{-T_h/\tau}$ . Then the lifetime is calculated in 3 ways: independently summing the number of UCN in the long and short holding times and calculating a single lifetime, calculating an average lifetime from the set of Monte Carlo runs, and calculating a weighted average from the set of Monte Carlo runs weighted by  $1/\delta\tau^2$ . The first method is free from bias because it is a sum of many numbers. Due to the central limit theorem, the sums are normally distributed and the ratio is therefore simple to handle. The first method reproduces the input lifetime within statistics.

The results can be seen in Figure 10.2. The bias in using the unweighted average is significantly less. At 20,000 UCN counted the effect is around 0.1 s whereas for the weighted average it is around 0.3 s. Historically, 10,000 to 20,000 UCN have been trapped per short run. The ultimate statistical uncertainty of our result is around 0.7 s

## 10.4 FINAL CALCULATION

The average lifetimes are calculated as follows:

- Calculate  $\tau_i$  using Equation 10.3
- For each cleaning and running condition, calculate  $\bar{\tau} = \sum \tau_i / N$
- For each cleaning and running condition, measure uncertainty as  $\delta\bar{\tau} = \sigma / \sqrt{N}$
- Calculate a final, weighted average  $\tau_{\text{trap}} = \sum \frac{\bar{\tau}}{\delta\bar{\tau}^2} / \sum \frac{1}{\delta\bar{\tau}^2}$
- Calculate a final average uncertainty  $\delta\tau_{\text{trap}} = \sqrt{1 / \sum \frac{1}{\delta\bar{\tau}^2}}$

The final weighted average is the most efficient use of the statistics. Each run set has hundreds of thousands of UCN so a weighted average over high-precision results should not be significantly affected by the statistical bias.

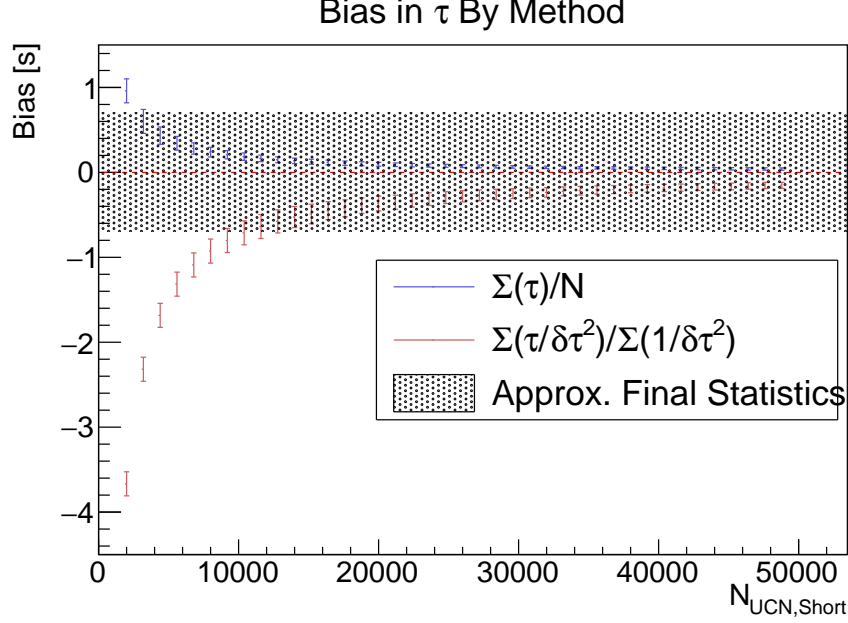


Figure 10.2: Statistical bias as a function of number of UCN unloaded per short run. Blue points are the unweighted average and red points are the weighted average. The gray band represents the statistical reach in the 2016-2017 run cycle.

## 10.5 RESULTS

The results of the analysis are given below. Table 10.1 gives the lifetimes from the singles analysis, which are the central value for the final lifetime result. It also gives the size of corrections for background subtraction and deadtime correction. These are calculated by comparing the central value with and without the correction.

Table 10.2 gives the lifetimes from the coincidence analysis. Because of the difficulty in assessing the deadtime and pileup corrections, this value serves as a check on the central value from the singles analysis. The size of the background correction is given.

The two analysis styles agree. The analyses are subject to different corrections. The singles analysis suffers from large background corrections (around 100 s), whereas the coincidence analysis suffers from potentially large deadtime or pileup corrections (up to several seconds), and significantly smaller background subtraction (up to several seconds).

<b>2016-2017 Singles</b>				
Run Set	$\tau$ [s]	Correction [s]		$\chi^2$
		Background	Deadtime	
200s Clean/1 Dip	878.4 $\pm$ 1.9	-82	-0.3	0.23
200s Clean/9 Dip	877.3 $\pm$ 2.1	-389	-0.03	0.01
300s Clean/9 Dip	876.6 $\pm$ 2.2	-376	-0.03	0.17
50s Clean/Full Field	879.5 $\pm$ 1.2	-165	-0.3	2.6
50s Clean/Half Field	875.8 $\pm$ 1.1	-121	-0.3	2.3
				$\frac{\chi^2}{\text{NDF}}$
<b>Average</b>	<b>877.5<math>\pm</math>0.68</b>			<b>1.3</b>

Table 10.1: Lifetime by set for the 2016-2017 Singles Analysis

2016-2017 Coincidence				
Run Set	$\tau$ [s]	Background [s]	$\chi^2$	
200s Clean/1 Dip	877.7±1.8	-1.3	0.04	
200s Clean/9 Dip	878.1±2.2	-4.4	0.13	
300s Clean/9 Dip	877.0±1.9	-3.6	0.03	
50s Clean/Full Field	879.4±1.3	-2.2	2.4	
50s Clean/Half Field	875.3±1.2	-2.1	2.8	
			$\frac{\chi^2}{\text{NDF}}$	
Average	877.4±0.69			1.3

Table 10.2: Lifetime by set for the 2016-2017 Coincidence Analysis

## CHAPTER 11

### SYSTEMATIC CORRECTIONS

#### 11.1 HEATED UCN UNCERTAINTY ESTIMATE AND UNCLEANED UCN UNCERTAINTY ESTIMATE

Originally, a data-driven method was used to estimate the uncertainty due to the presence of microphonic heating or uncleaned neutrons. This method relied on counting the population above the cleaning height and extrapolating that population to form an upper bound on the shift in  $\tau_n$  [33] and estimated the effect to be  $<0.24$  s in the case of heating and  $<0.07$  s for uncleaned UCN [31]. However, subsequent simulation work detailed in Chapter 13 has raised legitimate concerns about the accuracy of this analysis. In particular, the simulations show that the assumption of high efficiency counting of high-energy UCN may be incorrect. Nonetheless, a full Monte Carlo simulation of these effects estimates the size of combined heating and insufficient cleaning at 0.03 s with an uncertainty of 0.16 s.

The justification, details of the correction, and results are presented in Appendix A.1 for posterity. However, the author no longer endorses the conclusions reached therein.

#### 11.2 DISCRIMINATOR DEADTIME UNCERTAINTY

The discriminator counts individual photon signals from the detectors. A discriminator is subject to deadtime: due to finite logic pulse width, 2 incoming PMT signals can arrive during an output discriminator pulse. Any variation in the width of the output pulse could cause a systematic shift

in the lifetime. By visual inspection, the discriminator which counted individual photon events in the dagger had a width of  $10 \text{ ns} \pm 20\%$ . To first order, this uncertainty affects the estimated deadtime correction linearly (that is, the number of counts added to account for deadtime is first order linear in the deadtime).

The deadtime correction is described in Section 8.4. The Monte Carlo method detailed in Appendix A.2 is used to estimate the size of the effect given the uncertainty observed. To estimate the systematic uncertainty, a scaling factor for the deadtime counts is generated using a normal distribution centered at 1 with  $\sigma = 0.2$ . The lifetime was measured for each sample of the scaling factor. Using this error propagation method, the systematic uncertainty from the deadtime correction is estimated to be 0.05 s.

### 11.3 SPECTRAL CORRECTION

Uncertainty due to normalization is not explicitly accounted for in this analysis. In principle, using different normalization schemes can give some indication of the uncertainty involved. Due to the paired nature of runs, the source is close to being the same between short and long holding times. Adding in the spectral correction from Section 9.7 affects the stability of the population size, but does not affect the lifetime significantly. Table 11.1 shows a comparison of a handful of different normalization styles.

Style	$\tau_n$ [s]
SP + BA or OL	$877.37 \pm 0.69$
SP only	$877.57 \pm 0.67$
BA or OL only	$877.45 \pm 0.65$

Table 11.1: Comparison of  $\tau_n$  obtained using different normalization schemes. The standpipe monitor (SP) views UCN above the trap height, the bare (BA) and old (OL) monitors view all UCN at beam height.



A rough estimate of 0.2 s uncertainty will be added, which is the worst case scenario of doing or not doing the spectral correction.

## 11.4 DEPOLARIZATION

Ultracold neutrons can spontaneously depolarize during storage. This event causes a loss of neutrons; upon depolarization UCN are immediately attracted to the Halbach array and quickly scattered or absorbed. An insufficiently strong holding field can allow large amounts of depolarization. The effect of depolarization is estimated by varying the holding field inside the apparatus. The adiabatic assumption is slightly violated for UCN inside the trap; a small part of their wavefunction is in the opposite spin state. There is a small probability for a UCN to spontaneously flip spins during tracking. An estimate for the functional form of the depolarization rate due to this effect is [43]

$$\frac{1}{\tau_{\text{dep}}} \sim B_{\perp}^{-2} \quad (11.1)$$

$$\tau_{\text{trap}} \sim 1 / \left( \frac{1}{\tau_n} + \frac{\lambda_{\text{depol}} B_0^2}{B_{\perp}^2} \right), \quad (11.2)$$

which comes from tracking spins in a simulation of a magnetic trap.

Equation 11.1 does not take into account depolarization due to field zeros. At low fields, field zeros are expected to dominate the loss. Steyerl [43] recommends use of this form above 5 mT in holding field strength. Below this, the depolarization rate was simulated to be lower than suggested from Equation 11.1. Using this form is then expected to give an upper limit. The lifetime in the trap was measured as a function of holding field, at various field strengths between 0 and full strength (approximately 6.8 mT). Lifetime values with field strengths at least 0.68 mT were fit to Equation 11.2.

The fit was performed using both  $\chi^2$  minimization and using Bayesian techniques with Markov chain Monte Carlo with consistent results. The central value is used to estimate the size of the

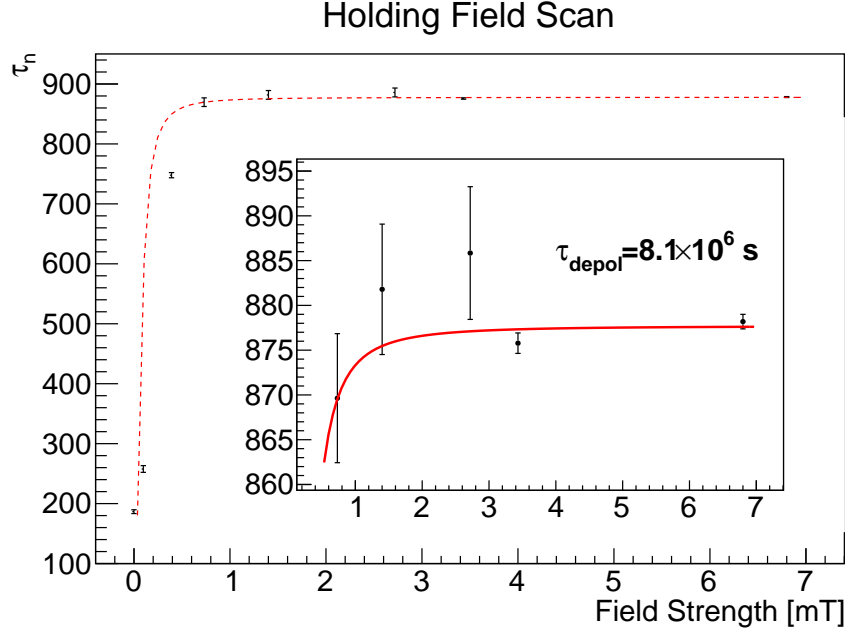


Figure 11.1: Lifetime in the trap as a function of holding field. Insert shows points which were fit to Equation 11.2. Only data  $\geq 0.68$  mT were fit.

correction and the uncertainty on the fit is used to measure the systematic uncertainty. The spectral dependence on depolarization is not measured, so the average depolarization rate,  $\lambda_{\text{depol}}$  is used to correct the lifetime as follows:

$$\frac{1}{\tau_n} = \frac{1}{\tau_{\text{trap}}} - \frac{B_{\text{full}}^2}{B_{\text{set}}^2} \lambda_{\text{depol}}. \quad (11.3)$$

The average lifetime of all 5 run sets is then

$$\bar{\tau}_n = \left( \frac{\sum \frac{\tau_n}{\delta \tau_{\text{trap}}^2}}{\sum \frac{1}{\delta \tau_{\text{trap}}^2}} \right). \quad (11.4)$$

Assuming Gaussian errors, the derivative can be taken and the error in the fit propagated through. The large effect from the half field data contributes significant uncertainty to the correction. Had the final data set been taken at full field, the expected uncertainty would be roughly halved.

Fitting estimates the depolarization rate to be  $1.2 \times 10^{-7} \pm 1.1 \times 10^{-7} \text{ s}^{-1}$ . This corresponds to

a depolarization lifetime of  $8.1 \times 10^6$  s. Using these values with Equation 11.4 and its derivative, the estimated effect from depolarization is  $-0.17 \pm 0.15$  s.

## 11.5 PHASE SPACE EVOLUTION UNCERTAINTY

The distribution of UCN positions and velocities inside the trap can drift over time. This effect is called phase space evolution. If a part of the UCN phase space is depleted, the other orbits inside the trap can eventually re-fill it. This is especially noticeable when using the dagger detector to clean halfway into the trap. The orbits that quickly reach the dagger are rapidly cleaned. However, there are a large number of other orbits which take a longer time to be detected. If the trap is only partially cleaned this way, then the undetected UCN can eventually re-populate the depleted region of phase space. This re-population will cause a shift in the mean counting time of UCN and therefore affect the storage time.

The mean arrival time is used to measure the storage time during each run. The lifetime is linear in the storage time, so it is important to accurately determine it and estimate the uncertainty of using the mean arrival time.

Phase space evolution could also occur when the UCN filling routine does not uniformly populate phase space. Over the storage time, UCN will slowly populate initially difficult to reach areas of the trap. This, too, can cause a shift in the mean counting time.

Backgrounds can also shift the mean arrival time. Because the backgrounds are constant, they tend to shift the mean counting time towards the segments of data which have low signal. For example, if there were 100s of counting before detecting UCN, the long runs would be expected to have a lower mean arrival time than short runs because the mean arrival time of the backgrounds contributes more significantly.

The background contribution can be corrected by subtracting off the expected mean arrival times of a constant background process. The expected mean arrival time in Equation 11.5 for a constant process would be halfway between the start and the end of the counting period.

$$\begin{aligned}
\bar{T} &= \sum_{i=1}^N t_i / N \\
\mathbb{E}(\bar{T}_{\text{bkg}}) &= \frac{\Delta T}{2} + T_s \\
\mathbb{E}\left(\sum_{\text{bkg}} t_i\right) &= \mathbb{E}(\bar{T}_{\text{bkg}}) \times N = \frac{\Delta T}{2} \times R\Delta T + T_s \times R\Delta T,
\end{aligned} \tag{11.5}$$

where  $t_i$  is the arrival time of an event,  $N$  is the total number of events,  $\Delta T$  is the length of the counting period,  $T_s$  is the start of the counting period,  $R$  is the background rate, and  $\sum_{\text{bkg}} t_i$  represents the sum of arrival times for the background process. The background subtracted mean arrival time is then given by

$$\bar{T} = \left( \sum_{i=1}^N t_i - \frac{\Delta T}{2} \times R\Delta T - T_s \times R\Delta T \right) / (N - R\Delta T). \tag{11.6}$$

This effect was investigated by measuring the background subtracted mean arrival times for short and long storage runs and comparing to the programmed storage times:

$$\delta\bar{T} = (\bar{T}_l - \bar{T}_s) - \Delta T_{\text{program}}. \tag{11.7}$$

Significant deviations from zero indicate the possible presence of phase space evolution. Averages of  $\delta\bar{T}$  over the 5 run segments are presented in Table 11.2.

There is weak evidence at  $\sim 4\sigma$  that the mean arrival times show phase space evolution. The worst case scenario of an unknown systematic shift in  $\Delta\bar{T}$  of 0.076 s is used to estimate the size of the systematic uncertainty:

$$\tau_i = \text{Avg} \left( \sum \frac{(\Delta\bar{T}_i \pm \epsilon)}{\ln(N_s/N_l)} \right), \tag{11.8}$$

where  $\Delta\bar{T}_i$  is the holding time in the  $i$ th set using the mean arrival times,  $\epsilon$  is the uncertainty in measuring phase space evolution using the mean arrival times,  $N_s$  is the short population in each run and  $N_l$  is the long population in each run.

Run Set	$\overline{\delta T}$ [s]	$\sigma/\sqrt{N}$ [s]
200s Clean/1 Dip	-0.005	0.014
200s Clean/9 Dip	-0.107	0.076
300s Clean/9 Dip	-0.038	0.068
50s Clean/Full Field	0.009	0.016
50s Clean/Half Field	-0.016	0.018
<b>Average</b>	-0.037	0.009

Table 11.2: Measured difference between programmed and mean storage times

The average lifetime is given by the weighted average of  $\tau_i$ . Using Gaussian error propagation gives

$$\delta\tau = \epsilon \times \frac{\sum \left( \frac{\tau_i}{\Delta T_i \delta\tau_i^2} \right)}{\sum \left( \frac{1}{\delta\tau_i^2} \right)} = \epsilon \times \bar{\tau}. \quad (11.9)$$

Inserting the values of  $\tau_i$ ,  $\delta\tau_i$ ,  $\Delta\bar{T}_i$ , and  $\epsilon$  gives an uncertainty of 0.06 s. Note that the shift in  $\tau$  is approximately 0.03 s, and is already included in the reported values from Section 10.5.

## 11.6 POSITION DEPENDENT BACKGROUND

The evaluation of the position-dependent background for the singles analysis can also contribute uncertainty in the lifetime evaluation. This is especially true for the 9-step data because its signal to background is much lower than the single step data.

Monte Carlo methods were used to estimate the uncertainty from position dependent background evaluation. The background fit was described in Section 8.3. The difference in the background rate at each height and at 380 mm was fit to a cubic function set to be zero at 380 mm. The extracted parameter and its uncertainty was  $A = 8.0\text{E-}5 \pm 2.3\text{E-}6 \text{ s}^{-1}\text{mm}^{-2}$ .

This parameter is sampled as a Gaussian with  $\sigma$  given by the uncertainty in the fit. For each sampled value of  $A$ , a final  $\tau_n$  is calculated; the distribution of  $\tau_n$  gives the uncertainty due to the

Systematic	Correction [s]	Uncertainty [s]	Method
Discriminator deadtime	-	0.05	Data
Normalization	-	0.2	Data
Depolarization	+0.17	0.15	Data
Phase space evolution	-	0.06	Data
Position dependent background	-	0.005	Data
Residual gas upscattering [31] [44] [45]	+0.16	0.03	Data
Insufficient cleaning and heating §18.1	+0.03	0.05, 0.15	Monte Carlo

Table 11.3: Summary table of systematic effects

uncertainty in  $A$ .

The estimated uncertainty from the position dependent background was  $\pm 0.005$  s.

## 11.7 SUMMARY

UCN $\tau$  measured a raw lifetime value of  $877.5 \pm 0.68$  s. A systematic shift of  $+0.17$  s due to depolarization is needed and detailed in Section 11.4. An additional shift of  $+0.03$  s due to insufficient cleaning and heating is estimated via the simulation in the subsequent Section 18.3. A final shift of  $+0.16$  s [31] [44] [45] due to upscattering on residual gases is needed, but not detailed in this work. Adding these corrections and summing their uncertainties in quadrature gives a final measurement of  $\tau_n = 877.9 \text{ s} \pm 0.68 \text{ s(stat.)} \pm 0.3 \text{ s(sys.)}$ .

## CHAPTER 12

### UCN $\tau$ OPTIMIZATION

#### 12.1 SPIN FLIPPER TUNING

The UCN which exit the source are polarized such that they seek high fields. This is because they pass through the PPM - a 7 T magnet which polarizes the UCN. Only UCN that gain energy when moving into high field regions (High-field seekers) can pass through the PPM and its foil membrane. High field seeking UCN cannot be trapped in UCN $\tau$  because these UCN would be attracted to the walls and would quickly be absorbed or scattered. An adiabatic fast passage spin flipper is used to flip the spins of UCN before entering the trap [30].

The AFP spin flipper produces a combination of radio frequency (RF) and static magnetic fields. The static magnetic field (called the  $B0$  field) is monotonically decreasing towards the trap volume. The RF field has a frequency  $\omega$  and is perpendicular to the  $B0$  field. In a rotating reference frame about the  $B0$  axis rotating at  $\omega$ , the observed field's angle with the  $B0$  axis goes through a change of  $\pi$  radians. This slow change adiabatically flips the spins [46].

Both the  $B0$  field and  $\omega$  need to be at a resonance point to flip spins of UCN passing through the spin flipper. In the 2015-2016 and 2016-2017 cycles, the  $B0$  field was tuned at a fixed  $\omega$  to optimize spin flip efficiency. The current in the coil is stepped by hand and the rate in a spin-sensitive detector is manually measured. The turning points of the spin flipper efficiency plateau are identified and the final current for the run cycle is set at their midpoint. The *in situ* detector can serve as a spin-sensitive detector by lowering it partway into the trap. The large magnetic

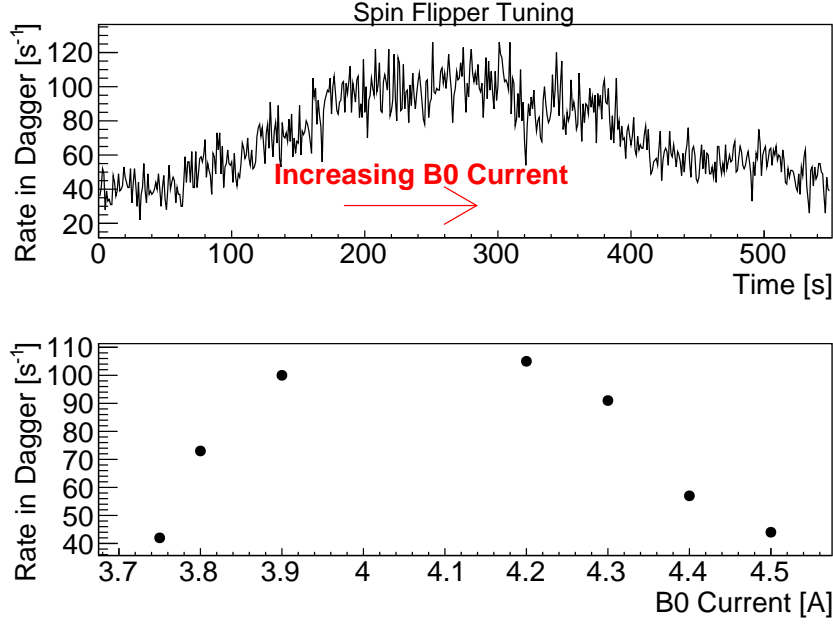


Figure 12.1: Top: Rate in the main detector during tuning. Bottom: Rate in the main detector as a function of  $B0$  coil current.

trapping surface will act as a spin analyzer by consuming wrong-spin UCN. High field seeking UCN will be attracted to the trap surface and will be removed. If spins are flipped, the detector will measure a higher rate. The time constant for counting UCN at that height is tens of seconds, so an equilibrium rate is reached relatively quickly. Figure 12.1 demonstrates a tuning run of the UCN $\tau$  apparatus. The operating point was set at 4.1 A (the current monitor on the  $B0$  coil only has 0.1 A precision).

## 12.2 FILLING TIME SCAN

During loading, the trapdoor hole is the final restriction into the trap. Due to its small size compared to the surface area of the Halbach array, filling the trap with UCN to saturation takes several minutes.

The time constant was studied by filling the trap for a varying amount of time and measuring the density as a function of filling time. Normalization is more difficult here because the shortest



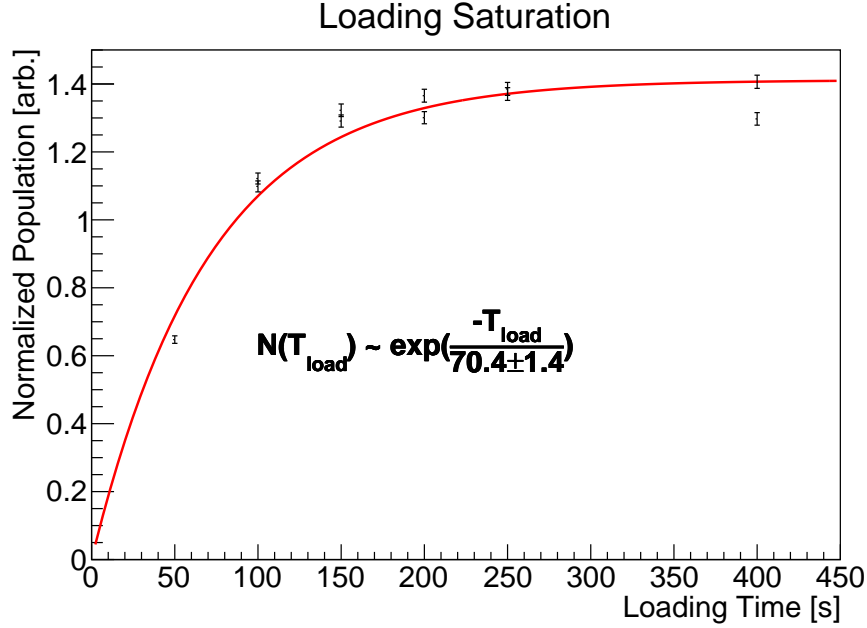


Figure 12.2: Filling time scan. Data was fit to a saturating exponential function

fills are 50 s, which is not sufficient to saturate the guide density and perform a normalization using the monitor rates. Instead, the performance of the source is measured by taking the first 50 s of each fill. This assumes the source output does not change drastically from the beginning to the end and is therefore only a rough normalization. Figure 12.2 shows data from 2016-2017; the time constant was measured to be 70 s. We chose 150s of filling which was judged to be a good tradeoff between density and time. This also matches the filling time in previous years' running.

### 12.3 DETECTION TIME CONSTANT

The counting process is approximately exponential, meaning the rate in the dagger is proportional to the population. At higher heights, the cross-sectional area of the detector is smaller compared to the size of the trap. This causes the detection time constant to be significantly higher at higher heights. At the cleaning height, the time constant is more than an order of magnitude slower than at the bottom of the trap.

Detection time constants were measured by initially filling the trap with UCN, then counting

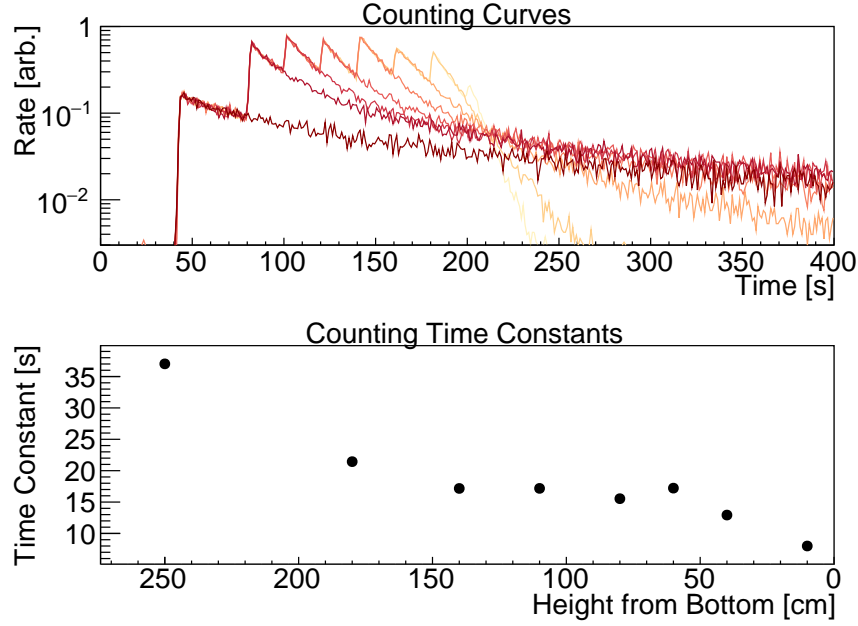


Figure 12.3: Top: Time series of rate in detector as a function of time. Bottom: Time constant as a function of height.

the population as if it were a normal run but stopping at a given height for several hundred seconds to tens of seconds. At the end, the detector was dipped to the bottom to measure the remaining UCN.

Figure 12.3 shows the curves superimposed on one another, as well as the time constant as a function of height. The data was normalized so that counting curves overlap. The curves were fit with double exponential functions, and only the short time constant is reported.

## 12.4 CLEANING TIME CONSTANT

The cleaning time constant for the 2016-2017 data was measured directly using the instrumented cleaner. The cleaner detector and the giant cleaner were at equal heights as measured by a laser level in situ. The cleaner detector had 4 PMTs, which were put into 2 channels of 2 each. Coincidences were made with the same algorithm as the dagger detector, but with different cuts. Here, a 100 ns initial coincidence window, a 10000  $\mu$ s integration time of fixed length, and a cut of 2 PE is used.

The data from the cleaner was not used to measure the lifetime, so no work was done to optimize the cuts or study rate-dependent effects.

A time series of UCN events during cleaning is fit with a single exponential to measure the cleaning time. The background rate of the detector was different when the detector was in cleaning position and away, so data was only taken during the cleaning phase. Additionally, a group of UCN is pushed by the trapdoor as it closes during the beginning of the storage period. This cuts out a significant portion of the cleaning time constant measurement.

Figure 12.4 shows the fits and the data for the cleaning time constant. The time constant is relatively short at 2.5 s. Cleaning time varied between 300 s to 50 s, all of which are at least 20 cleaning lifetimes. The surface area of the instrumented cleaner is relatively small compared to the rest of the trap ( $\sim 10\%$ ). The giant cleaner covered roughly half the trap. The mismatch in size puts uncertainty on how the time constant observed matches the actual cleaning time constant. Because of the small size, its orbits may be cleaned preferentially and therefore bias it towards shorter cleaning time constants. However, the short time constant and lack of UCN at longer times suggests that the trap is effectively cleaned within the cleaning times used.

## 12.5 PHASE SPACE EVOLUTION

UCN orbits inside the trap can be non-ergodic and have long time constants to visit a given area of the trap. This is especially evident when cleaning is enhanced by using the dagger detector. Orbits that easily access the dagger are quickly counted, but a large number of orbits remain uncleaned at the dagger's level. This shows up as phase space evolution, where the absorption time for a given spectral population is enhanced after storage for long periods of time.

This phenomenon was investigated using a cleaning condition where the dagger detector was lowered halfway into the trap (25 cm from the bottom). This is lower than the nominal cleaning height of the cleaners (approximately 38 cm). The dagger quickly depletes trappable UCN in the energy band between 25 cm and 38 cm that can reach it, but leaves a large fraction of them

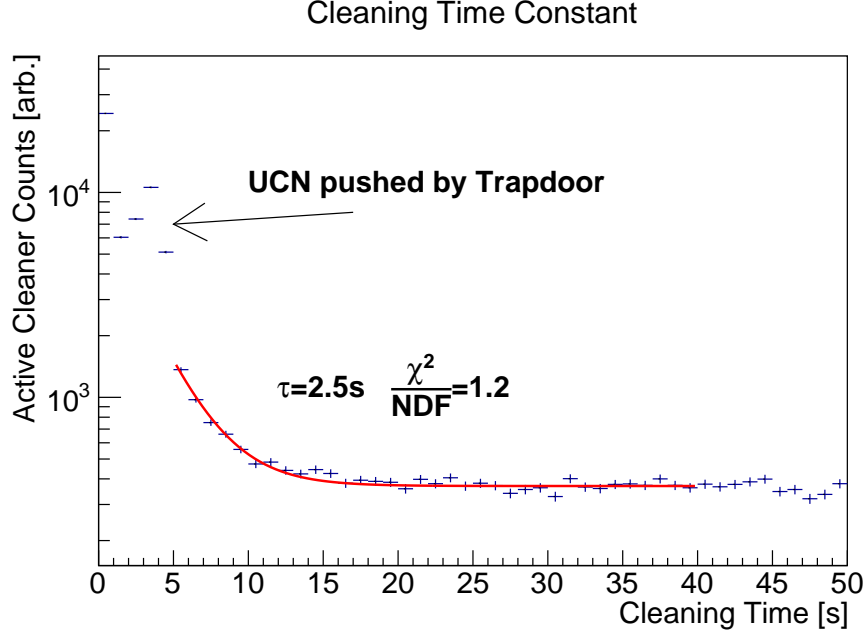


Figure 12.4: Cleaning time constant as observed by instrumented cleaner. Fit to single exponential with background.

untouched. During storage, the UCN in this energy band re-fill phase space uniformly which allows them to be counted faster during a long holding run.

Figure 12.5 shows this effect. The data consists of runs with 200s of combined dagger and absorber and a variable holding time between 20 s and 1000 s. The population at 25 cm is normalized to the population in the whole trap and this ratio is plotted as a function of holding time. As holding time increases, the number of UCN observed in the topmost counting position increases as UCN slowly refill phase space.

In normal running, this is avoided by not using the dagger to clean.

## 12.6 PEAK 1 COUNTING TIME CONSTANT

The efficiency for counting UCN above the cleaning height using the dagger detector needs to be known in order to perform the estimates in Section A.1. During normal running, no or very few UCN are expected to be above the cleaning height. It is difficult to measure the counting time

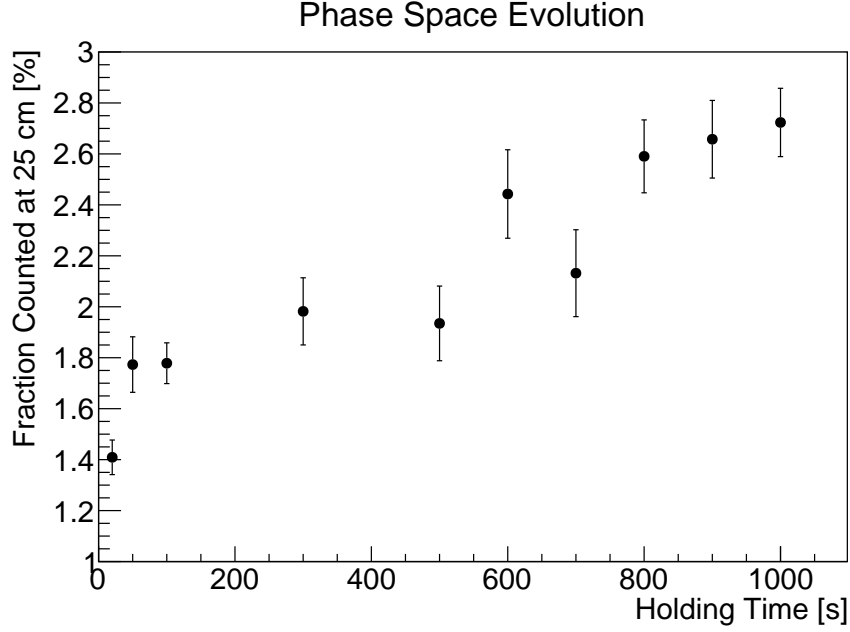


Figure 12.5: Population at 25 cm as a function of holding time.

constant of this population. However, taking runs where the cleaner is not inserted fully populates this region so that the detection characteristics of UCN in Peak 1 can be measured.

Runs were taken where the trap was filled for 150 s with the cleaner up, followed by a 20 s short holding time without cleaning, and a 300 s counting period at 38 cm. This populates the energy band between 38 cm and 43 cm. After the counting period, the trap is unloaded using the trapdoor and not counted in the dagger. Counting at 38 cm ensures that only UCN with energies above the cleaning height will be measured. The results can be seen in Figure 12.6.

A large initial tail of UCN with energies  $> 43$  cm is seen. This population is both cleaned out by the detector and the raised cleaner. After this population leaves, then an exponential tail of UCN with energies  $38 \text{ cm} < E < 43 \text{ cm}$  is seen. This population was counted with a time constant of 386 s. By taking into account  $\beta$  decay and integrating the counting curve, 1,500 UCN are expected per run at energies above 38 cm. The population of UCN with  $E > 38$  cm can be used to predict the population with  $E < 38$  cm. If the UCN in Peak 1 are counted with high efficiency, then the predicted low-energy population should match the number of UCN in a short

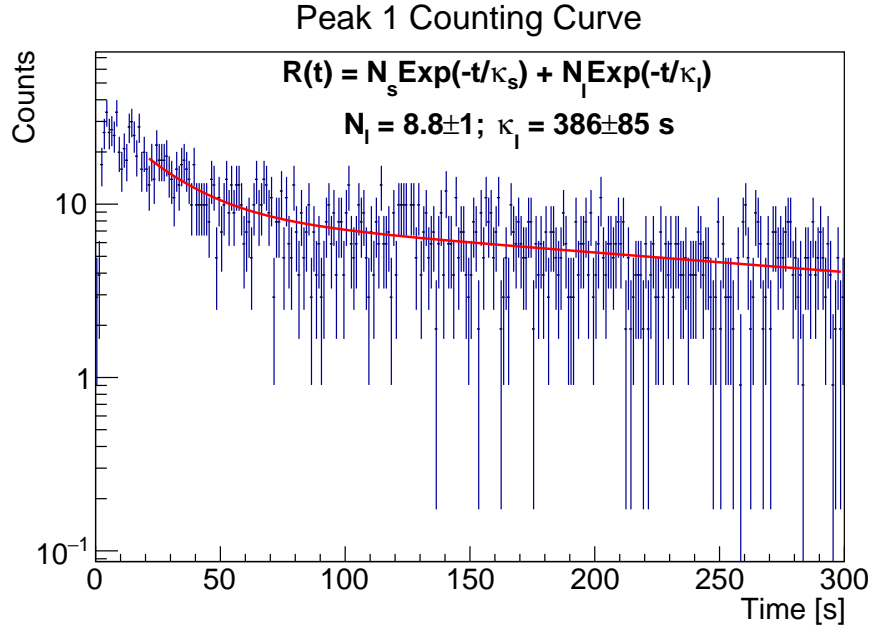


Figure 12.6: Arrival time for UCN with energy  $> 38 \text{ cm}$

lifetime run. Using the spectral model from Section 17.3, 4000 UCN would be expected in a short holding time run.

However, short holding time runs with the same gate valve rate and source performance yielded 16,500 UCN per run. Inserting the detector at 38 cm only counts  $24 \pm 10\%$  of the energetically available UCN in the trap. This likely means that the corrections from Section A.1 are incorrect by at least a factor of 4.

## CHAPTER 13

### OVERVIEW OF UCN $\tau$ SIMULATIONS

The detectors in UCN $\tau$  provide a wealth of information. However, detection of a UCN means destruction of that UCN. This means that no information about the history of a specific neutron can be gathered. The monitor detectors (which also destroy UCN) are the primary source of information about the neutron population coming from the source.

However, after the trapdoor is closed no information about UCN can be gathered during storage. Only the arrival times on the main detector can be used to estimate effects such as heating or phase space evolution. The main detector counts all UCN that can reach it regardless of energy, so information about specific energy bands is often mixed with other energy bands, making analysis of phase space effects difficult.

In addition, the UCN $\tau$  trap uses magnetic reflections during storage which do not diffusely reflect UCN. Sub-populations in phase space can have significantly long lifetimes in the trap, which lead to phase space effects.

These aspects of the experiment make Monte Carlo simulations an attractive prospect: they give the ability to have total knowledge of a UCN and its history while reproducing the experimental conditions. This total knowledge allows estimates of collection efficiencies and decoupling of different UCN populations. It also allows for sensitive estimates of losses inside the trap.

The goal of Monte Carlo simulations is to model the experiment in sufficient detail to both reproduce data and predict the size of systematic effects. First the geometry will be modeled to

reproduce the magnetic fields inside the trap. Then a detector will be simulated. Finally, a spectral model will be used to represent the population inside the trap.

The model will be tuned by varying parameters until the optimal agreement between data and simulation is reached. The tuned model will then be used to investigate systematic effects, efficiencies of detection, and model alternate scenarios to guide the development of future experiments.



## CHAPTER 14

### TOY MODELS OF THE $\text{UCN}_\tau$ TRAP

#### 14.1 MARKOV CHAIN MODEL OF HEATING

A toy model of the heating process can help drive intuitive understanding of the process and guide the interpretation of the results. The heating process is a kind of random walk. UCN gain or lose energy on every interaction with the wall and can eventually be evaporated out of the trap. Because the cleaners are raised by 5 cm after cleaning, there is a threshold below which heating will not significantly affect the lifetime. However, when the tail of the heated distribution begins arriving at the raised cleaner height, the shift in lifetime becomes significant.

The trap can be modeled using a Markov chain. A Markov chain is a system composed of a set of states where the next state is determined only by the current state. The transition probability from one level to another level is described by the Transition Matrix  $\mathbf{P}$  [47].  $P_{ij}$  describes the probability of state  $i$  transitioning to state  $j$  during the next step. A Markov chain can be absorbing if it contains a state  $a$  where all of the probabilities  $P_{aj}$  ( $a \neq j$ ) are 0.

The trap will be described by a Markov chain containing  $N$  states representing  $N$  energy levels in the trap between 0 and 43 cm. Additionally, there are 2 absorbing states: one for  $\beta$  decay which has a constant transition probability for every state, and one for absorption on the cleaner during storage. The cleaned absorbing state is reached by heating from the 43 cm energy level. Each step in the chain is a reflection on the wall, which occurs approximately every 1 s. During each wall bounce, a UCN will be modeled as having  $\frac{1}{2}$  probability of keeping its initial energy, and

$\frac{1}{4}$  probability of gaining or losing 1 energy level. This is expected to reproduce the microphonic heating behavior; it has  $\frac{1}{4}$  probability to be in phase or  $\pi$  out of phase, where it will get a positive or negative kick respectively. Otherwise, it will be out of phase and will not get kicked.

For each trapped UCN state above 0 energy, the entries in  $\mathbf{P}$  are  $\mathbf{P}_{i,i} = \frac{1}{2}(1 - p_\beta)$ ,  $\mathbf{P}_{i,i-1} = \frac{1}{4}(1 - p_\beta)$ ,  $\mathbf{P}_{i,i+1} = \frac{1}{4}(1 - p_\beta)$ ,  $\mathbf{P}_{i,\text{decay}} = p_\beta$ . The 0 energy level cannot lose energy, so instead it has  $\mathbf{P}_{0,0} = \frac{3}{4}(1 - p_\beta)$  and  $\mathbf{P}_{0,1} = \frac{1}{4}(1 - p_\beta)$ .

The matrix then reads

$$\begin{bmatrix} \frac{3}{4}(1 - p_\beta) & \frac{1}{4}(1 - p_\beta) & 0 & 0 & 0 & \dots & 0 & p_\beta \\ \frac{1}{4}(1 - p_\beta) & \frac{1}{2}(1 - p_\beta) & \frac{1}{4}(1 - p_\beta) & 0 & 0 & \dots & 0 & p_\beta \\ 0 & \frac{1}{4}(1 - p_\beta) & \frac{1}{2}(1 - p_\beta) & \frac{1}{4}(1 - p_\beta) & 0 & \dots & 0 & p_\beta \\ \vdots & \vdots & \vdots & \ddots & \vdots & \vdots & \vdots & \vdots \\ & \dots & & 0 & \frac{1}{4}(1 - p_\beta) & \frac{1}{2}(1 - p_\beta) & \frac{1}{4}(1 - p_\beta) & p_\beta \\ & & & \dots & & & 1 & 0 \\ & & & \dots & & & 0 & 1 \end{bmatrix}. \quad (14.1)$$

Given the transition matrix  $\mathbf{P}$  and an initial population vector  $\mathbf{u}$ , the population vector after  $n$  transitions is given by [47]

$$\mathbf{u}^{(n)} = \mathbf{u}\mathbf{P}^n, \quad (14.2)$$

where  $\mathbf{u}$  is a row vector and  $\mathbf{u}_i$  is the probability of being in state  $i$  at the beginning. To simulate the trap population,  $\mathbf{u}_i$  is  $\propto E$ , or 0 if  $E > 38$  cm.

Different heating scenarios can be simulated by expanding or shrinking the number of energy levels; since the UCN will only jump up or down one level, the level spacing describes the strength of heating. Short and long holding runs can be simulated using Equation 14.2 with  $n = 20$  steps for a short holding run and  $n = 1400$  steps for a long holding run. The lifetime is given by

$$\tau = \frac{n_{\text{long}} - n_{\text{short}}}{\log \left( \frac{1 - \mathbf{u}_{s,\text{lost}} - \mathbf{u}_{s,\beta}}{1 - \mathbf{u}_{l,\text{lost}} - \mathbf{u}_{l,\beta}} \right)}. \quad (14.3)$$

The lifetime as a function of energy transfer can be seen in Figure 14.1. The threshold nature

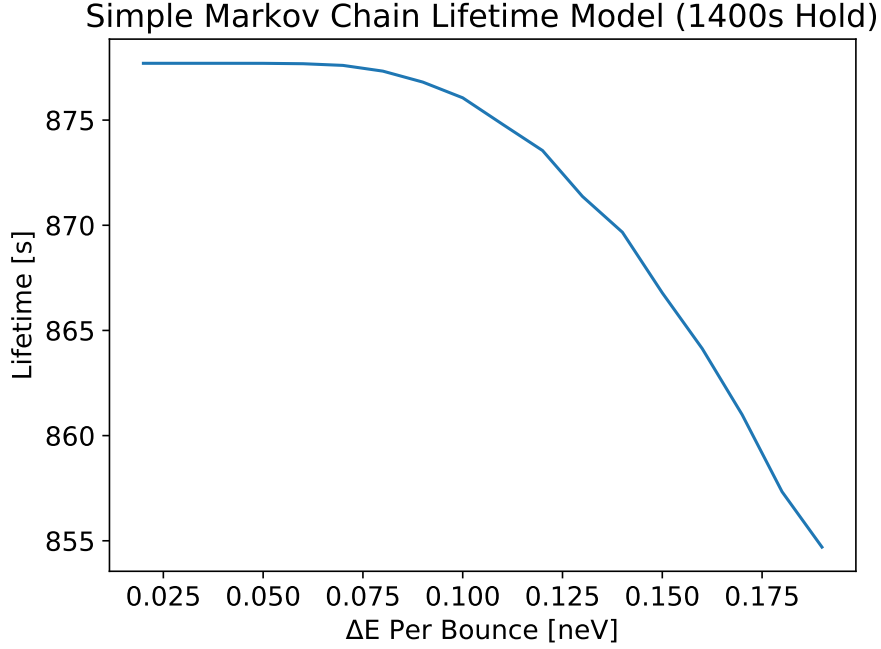


Figure 14.1: Trap Lifetime as a function of  $\Delta E$  per bounce in the toy model.

of the process is evident; below a certain amount of heating there is little effect. As the population between 38 and 43 cm is increased, the probability of being absorbed also increases. At some point, the tail of the heated distribution begins being eliminated during storage and the lifetime starts dropping dramatically. This means that there is a large amount of room to safely operate the trap, but it's not necessarily true that if heating is tolerable at one level that small increases in heating will also be tolerable.

## 14.2 PHASE SPACE EVOLUTION

The phase space evolution can be modeled as a simple counting process. Instead of counting UCN as a Poisson process, the arrival and death times are generated from exponential distributions. A 2-peaked run is modeled using 2 exponentials, one with time constant 100 s truncated at 20 s from the end of the holding time, and another one with time constant 7 s starting 20s after the end of the holding time. Additionally, random death times are generated at  $\tau = 877.7$  s. A UCN is

Measurement	Value
$\Delta T_{\text{hold}}$	-0.176 s
$\Delta\tau$ (using $\bar{T}$ )	<0.005 s
$\Delta\tau$ (using $T_{\text{hold}} = 1380$ )	-0.1 s

Table 14.1: Results of the phase space evolution toy model

counted if its exponentially distributed arrival time is less than its death time. UCN are counted for 120 s in total; UCN which arrive after 100 s into the 2nd dip are not counted.

A shift in the lifetime could be expected if a subset of the population is subject to more  $\beta$  decay during the counting period. This shift is due to the holding time no longer describing the real holding time.

Phase space evolution is modeled by modifying the population sizes in the long run. The population size of the 1st peak is decreased by 1% of the total and the population size of the 2nd peak is increased by 1% of the total. The short run has 10% of UCN in the 1st peak and 90% of UCN in the 2nd peak. A long run with phase space evolution will have 9% of the UCN in the 1st peak and 91% of the UCN in the 2nd peak.

The lifetime is calculated by taking the sum of counted UCN and using the mean arrival time of UCN ( $\bar{T}$ ). Comparing the lifetime of UCN with and without phase space evolution gives an estimate of the effectiveness of the phase space evolution correction. Results are given in Table 14.1. At least in the toy model, using the mean arrival time corrects for the effects of extra  $\beta$  decay due to phase space evolution.

## CHAPTER 15

### UCN<sub>τ</sub> MAGNETIC FIELD EXPANSION

The visible geometry of the trap for UCN is determined by the magnetic fields from the Halbach array. Summing the fields from all of the magnets in the trap is time consuming, so an expansion is used instead. The expansion treats the field as an ideal Halbach field which decays exponentially along the normal to the bowl surface. Additionally, there are sinusoidal ripples in the field due to the finite thickness of each magnetic stripe.

The magnetic field is given by [48]

$$\mathbf{B} = \frac{4B_{\text{rem}}}{\pi\sqrt{2}} \sum_{n=1}^{\infty} \frac{(-1)^{n-1}}{4n-3} (1 - e^{-k_n d}) e^{-k_n \zeta} (\sin k_n \eta \hat{\eta} + \cos k_n \eta \hat{\zeta}), \quad (15.1)$$

where  $B_{\text{rem}}$  is the remnant strength of the permanent magnets,  $k_n = 2\pi(4n-3)/L$ ,  $L$  is the period of the Halbach pattern, and  $d$  is the magnet thickness (1"). The sum is typically truncated after 3 terms.  $B_{\text{rem}}$  was taken to be 1.35 T (from empirical measurements), and  $L$  was taken to be 51.114 mm, which matches the falloff of the real Halbach array.

$\zeta$ ,  $\eta$ , and  $\xi$  are the local bowl surface coordinates.  $\zeta$  is the normal distance to the surface,  $\xi$  is the tangent in the direction of the holding field, and  $\eta$  is the other tangent. The bowl surface is made up of 2 torus patches of different radii joined at the bottom. The coordinates are then given by

$$\zeta(x, y, z) = r(x) - \sqrt{(\sqrt{z^2 + y^2} - R(x))^2 + x^2} \quad (15.2)$$

and

$$\eta(x, y, z) = r(x) \times \text{atan} \left( \frac{x}{\sqrt{z^2 + y^2} - R(x)} \right); \quad (15.3)$$

there is no dependence on  $\xi$  so it is not given.  $R(x)$  and  $r(x)$  are the major and minor radii of the tori, respectively. The major and minor radii are either 1.0 or 0.5 m on either side of the  $x = 0$  plane.

$R(x)$  and  $r(x)$  are defined using sigmoid functions

$$R = \frac{1}{2} + \frac{1}{2}/(1 + \exp(-\kappa x)) \quad (15.4)$$

and

$$r = 1 - \frac{1}{2}/(1 + \exp(-\kappa x)), \quad (15.5)$$

where  $\kappa = 1000$  is the transition region size, approximately 5 mm on either side of  $x = 0$ .  $R(x)$  and  $r(x)$  were chosen to be smooth functions of  $x$  to avoid step-functions at the  $x = 0$  plane. Additionally, the sum of  $r(x) + R(x)$  is constant. Using step functions deteriorated the energy conservation in the integrator by several orders of magnitude. Step functions caused large jumps in energy whenever a UCN traversed the  $x = 0$  region in high field.

The holding field is given by

$$B_\xi = B_0 \frac{r + R}{\rho} \hat{\xi}, \quad (15.6)$$

where  $\rho = \sqrt{z^2 + y^2}$ . The total field is

$$\mathbf{B} = B_\eta(\zeta, \eta) \hat{\eta} + B_\zeta(\zeta, \eta) \hat{\zeta} + B_\xi(y, z) \hat{\xi}. \quad (15.7)$$

The UCN are assumed to be in the adiabatic limit, so that their polarization is always maintained in the direction of the local  $B$ -field. In that limit, the potential is given by

$$U = -\mu \|\mathbf{B}\| + mgz = -\mu \sqrt{B_\eta^2 + B_\zeta^2 + B_\xi^2} + mgz, \quad (15.8)$$

where  $\mu$  is the neutron magnetic moment. The minimum potential energy was subtracted off and was found at

$$\mathbf{r}_{\min} = (0, 0, -1.46441366913). \quad (15.9)$$

The forces were found using Equation 15.8 by taking the gradient in Cartesian coordinates. The derivatives of the field strength are

$$\begin{aligned} \frac{\partial \|\mathbf{B}\|}{\partial [x, y, z]} = \frac{1}{\|\mathbf{B}\|} & \left( B_{\zeta} \left( \frac{\partial B_{\zeta}}{\partial \zeta} \frac{\partial \zeta}{\partial [x, y, z]} + \frac{\partial B_{\zeta}}{\partial \eta} \frac{\partial \eta}{\partial [x, y, z]} \right) \right. \\ & + B_{\eta} \left( \frac{\partial B_{\eta}}{\partial \zeta} \frac{\partial \zeta}{\partial [x, y, z]} + \frac{\partial B_{\eta}}{\partial \eta} \frac{\partial \eta}{\partial [x, y, z]} \right) \\ & \left. + B_{\xi} \left( \frac{\partial B_{\xi}}{\partial \zeta} \frac{\partial \zeta}{\partial [x, y, z]} + \frac{\partial B_{\xi}}{\partial \eta} \frac{\partial \eta}{\partial [x, y, z]} \right) \right). \end{aligned} \quad (15.10)$$

It is therefore easy to calculate both the total potential and force by summing the appropriate sine/cosine terms coming from Equation 15.1 and multiplying by the appropriate partial derivatives of the local coordinates.

## CHAPTER 16

### SYMPLECTIC INTEGRATION

#### 16.1 SYMPLECTIC INTEGRATION SCHEME

UCN are tracked in the magnetic field using a symplectic integrator. Symplectic integrators are believed to have good long-term stability in phase space due to their conservation of geometry [49]. UCN are tracked for 1500 s or more, so the stability of their distribution in phase space is important. An explicit, fourth order algorithm is used [50] (first published by Forest and Ruth [51]), which is reproduced in Table 16.1.

#### Symplectic Integration Scheme

$$t_0, \mathbf{x}_0, \mathbf{p}_0; H = T(\mathbf{p}_i) + V(\mathbf{x}_i)$$

**For i=1,2,3,4:**

$$\mathbf{p}_i = \mathbf{p}_{i-1} + b_i \delta t \times \mathbf{F}(\mathbf{x}_{i-1}, t_{i-1})$$

$$\mathbf{x}_i = \mathbf{x}_{i-1} + a_i \delta t \times \mathbf{P}(\mathbf{p}_{i-1})$$

$$t_i = t_{i-1} + a_i \delta t$$

Table 16.1: Symplectic integration scheme

The Hamiltonian is assumed to be of the form  $T(\mathbf{p}) + V(\mathbf{x})$ ,  $\mathbf{F}(\mathbf{x}, t) = -\nabla_{\mathbf{x}} V(\mathbf{x})$  is the force at  $\mathbf{x}$  and time  $t$ , and  $\mathbf{P}(\mathbf{p}) = \nabla_{\mathbf{p}} T(\mathbf{p})$ . The constants  $a_i, b_i$  are chosen to give a symplectic map; both Forest and Candy give the same analytic coefficients. In principle there are many (thousands) of solutions for the  $a$ 's and  $b$ 's that give symplectic integration [52]. McLachlan and Atela give numerically optimized  $a$ 's and  $b$ 's that are observed to conserve energy better than the analytic



constants. Those  $a$ 's and  $b$ 's are used in this work and are optimized to more digits than double precision, so are sufficiently precise.

Higher order integration schemes ( $N$  even) can be constructed using the coefficients of the  $N-2$  order scheme [53]. However, only the optimized coefficients for the 4th order symplectic scheme were used.

## 16.2 TEST OF SYMPLECTIC INTEGRATOR ON FIELD EXPANSION

Convergence of energy conservation of UCN trajectories can be seen in Figure 16.1. Three general features can be observed: 1) convergence in  $\Delta E$  as some power in  $\delta t$ , 2) local deviations in energy near array bounces, 3) and long-term shifts in energy.

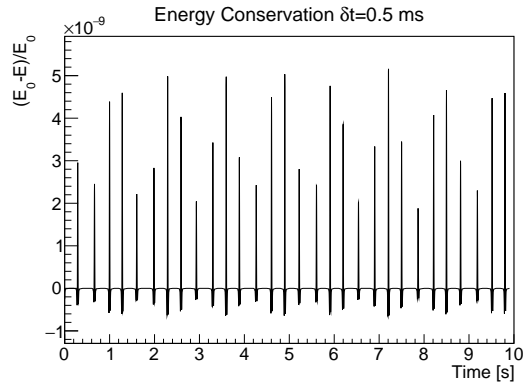
The first behavior is expected from a symplectic integration scheme; the error of the integrator is  $\mathcal{O}(\delta t^{n+1})$  [50]. The actual convergence for the Halbach array potential is slightly faster; this is possibly due to the effect of feature 3.

Local deviations in energy conservation in high-field regions are also expected. The symplectic integration does not solve the given Hamiltonian exactly, but is an exact solution to a nearby Hamiltonian [54, Chapter 9]. This gives it good long-term stability since it is an exact solution, but the solutions may be more different in regions of large gradients.

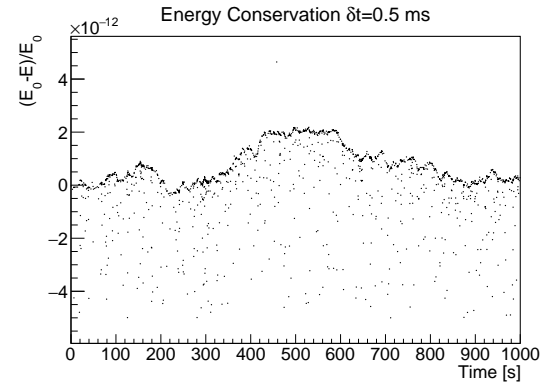
The third behavior is possibly due to numerical instabilities of the forces and potential in high-field regions. Steps in the energy are associated with wall collisions and were seen to be worse when the field was modeled using a step function for the major/minor radius change at  $x = 0$ . These steps at collisions give the drift from the mean value.

## 16.3 CONVERGENCE STUDIES

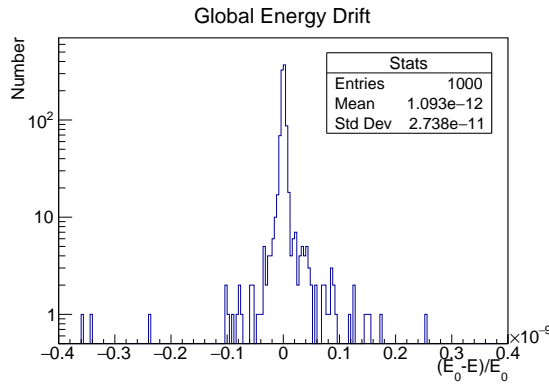
Due to the chaotic nature of the trap, convergence is difficult to study. Other neutron traps have had similar issues where the escape time of a given neutron does not converge with step size [55]. This means that an observable of any given UCN may not converge with step size. However, an



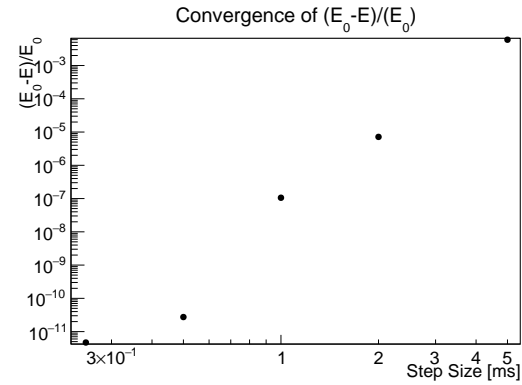
(a)  $E(t)$  over 10 s



(b)  $E(t)$  over 1000 s



(c)  $(E_0 - E)/E_0$  for 1000 UCN, 1000s,  $\delta t=0.5$  ms



(d) Standard Deviation of  $(E_0 - E)/E_0$  for different  $\delta t$

Figure 16.1: Energy Conservation of the symplectic integrator for UCN trajectories

$\delta t$ [ms]	Number of Terms					
	1	2	3	4	5	6
0.25			383445			
0.5	142465	383397	383249	383422	383220	383636
1.0			383452			
2.0			383439			

Table 16.2: Convergence using % of chaotic trajectories

ensemble average may be expected to converge with step size. The average energy conservation is at or better than 1 part per billion for a timestep of 0.5 ms. Estimates of the systematic effects in UCN $\tau$  used a timestep of 0.5 ms and took 3 terms in the field expansion.

Lyapunov characteristic exponents (LCE, defined in Section 20.1) were used as a coarse quantity to study convergence. Lyapunov exponents measure the chaotic nature of trajectories. The timestep and number of terms in the field expansion were varied and the distribution of Lyapunov exponents were studied. Changing the timestep changes the nearby Hamiltonian that is solved, which affects the exact evolution of a given initial condition. However, if the distribution does not qualitatively change then the behavior of the trap is converged at some level. The number of UCN with Lyapunov exponent  $> 0.75$  (considered chaotic trajectories) was calculated as a function of either  $\delta t$  or number of terms in the field expansion. Results are given in Table 16.2.

The only significant difference is the change from 1 term to more than 1. With only one term in the field expansion, the number of chaotic trajectories is more than halved. Otherwise, the number of chaotic trajectories is within error (assuming Poisson statistics). This can be seen in Figure 16.2 where the histograms of LCE for simulations with  $N \geq 2$  lie on top of each other.

Another way to look at this data is to histogram the Lyapunov exponents of the most precise simulation with lower-precision simulations. If the qualitative shape changes then the system is not yet converged. Results can be seen in Figure 16.3 and Figure 16.4. Qualitatively, the regular trajectories (near 0) are unperturbed, and the chaotic trajectories tend to get mixed up. However,

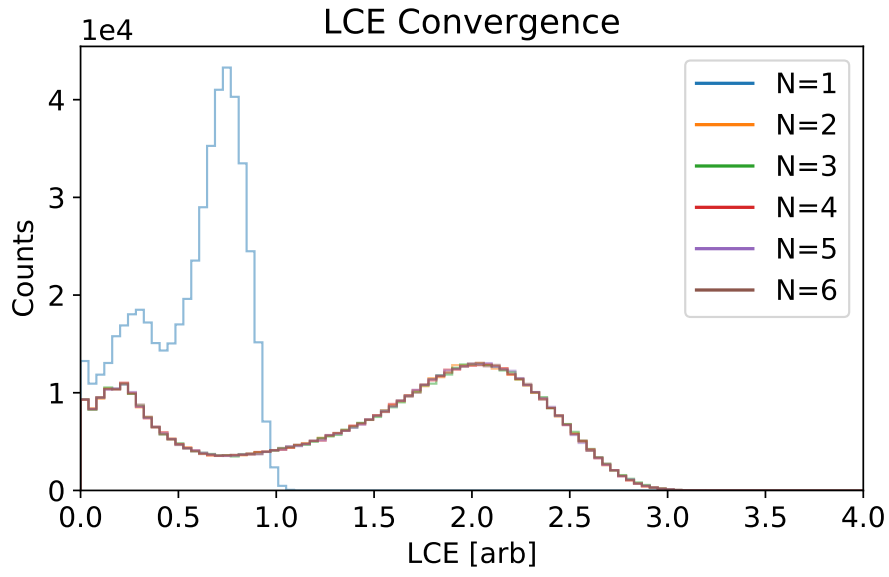


Figure 16.2: Convergence of results in  $N$

the shape of the distribution does not change significantly by adding more terms or by reducing the step size. Only going to 2 terms in the expansion changes significantly. The chaotic behavior of UCN inside the trap is converged at large time steps and at low numbers of terms.

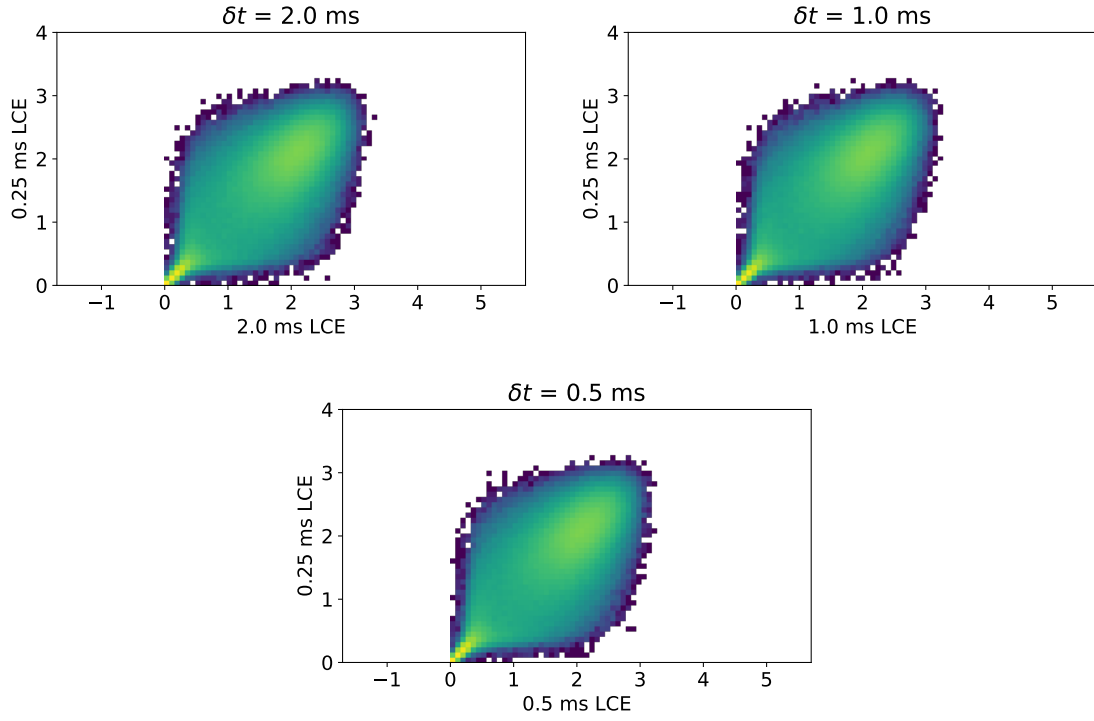


Figure 16.3: Convergence of trap in  $\delta t$

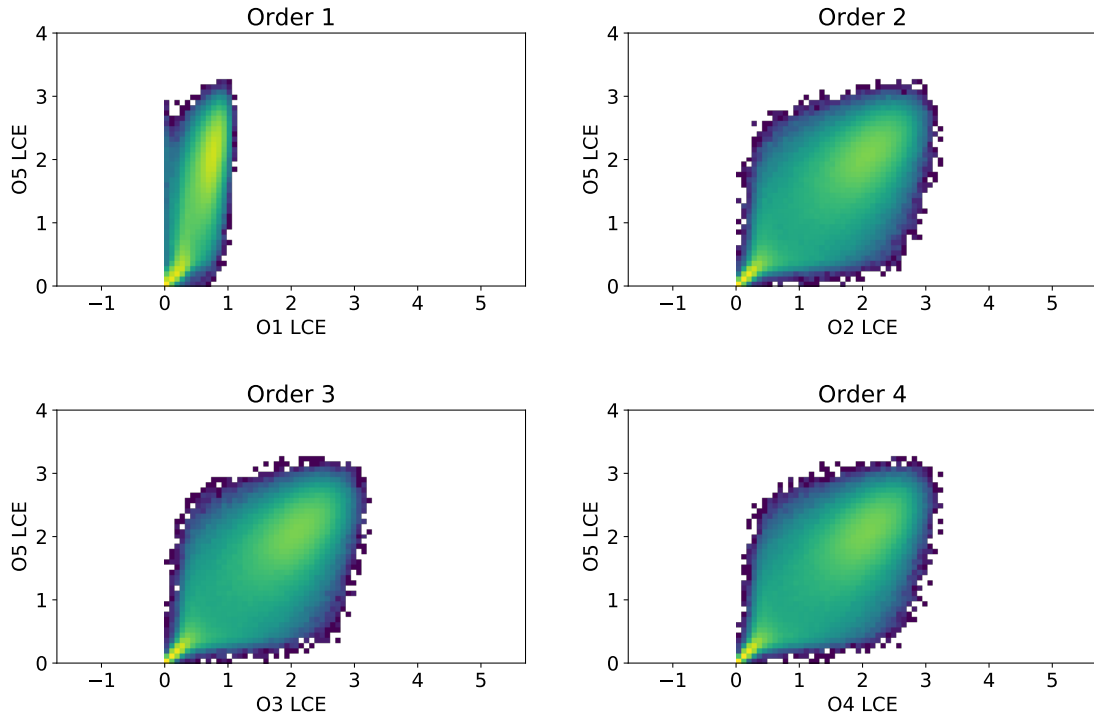


Figure 16.4: Convergence of trap in number of terms in field expansion

## CHAPTER 17

### SIMULATION OF 9-STEP DATA

#### 17.1 SIMULATION SCHEMATIC

The UCN $\tau$  experiment will be simulated by tracking UCN trajectories inside of the trap from an initial birth time to their death either due to  $\beta$  decay, absorption on a cleaner, or absorption on the detector. UCN will be created inside the trap due to the inability to simulate the trapdoor region accurately using the field expansion. They will be created using an effective spectrum which describes their distribution in energy and phase space. The geometry of the cleaners and detectors will be taken from the apparatus. The cleaners will be simplified to have a uniform efficiency (defaulting to 100% efficient). The detector will be modeled using a quantum multilayer formula.

The simulation parameters will first be tuned using a large dataset, then validated on an independent dataset. After tuning, phase space evolution, heating, and cleaning will be simulated.

#### 17.2 DETECTOR SETUP

The detector is modeled as being in the  $y = 0$  plane. The profile of the detector is bounded from below by the shape of the array, in the  $\pm x$  direction as a box and in the  $+z$  direction as a box. The bottom of the dagger is defined by  $\zeta' = 0$  where  $\zeta'$  is the local bowl coordinate  $\zeta$  offset in  $z$  by the position of the dagger detector above the array. The midline of the detector is offset at  $x = -15.24$  cm. The side edges of the detector are located at 20 cm from this line, giving a total width of 40 cm. The upper edge of the detector is 20 cm from the lowest point on the  $\zeta' = 0$  curve

at  $x = 0$ .

The aluminum housing of the detector is also simulated. The aluminum housing is modeled as a 100% diffusive reflecting surface. The housing begins at the top edge of the active detector area. The housing is composed of a trapezoidal bottom section and a rectangular top section. The height of the bottom trapezoid is 14.478 cm with a bottom width of 40 cm and upper width of 69.215 cm. The upper section has width 69.215 cm and height 12.192 cm.

The dagger was simulated to move with a velocity of  $\frac{49}{13} \text{ cm s}^{-1}$ , which is the approximate mean velocity of dagger actuation. The actual detector has acceleration and deceleration profiles which were not simulated.

Every time a tracked UCN passes the  $y = 0$  plane, the approximate  $x$  and  $z$  crossing position is calculated from the current and previous simulation step. The  $\zeta'$  is calculated and checked against the profile of the dagger. Absorption or reflection is then simulated if the UCN is detected crossing the profile of the detector or the housing.

Reflection is modeled as being 100% diffusive. The new UCN momentum direction is distributed as in Lambertian reflection. The distribution of momentum direction is  $\propto \sin(\theta)\cos(\theta)$ .

The detector surface is modeled as a multilayer surface. A UCN interacting with an absorbing multilayer surface is treated in Golub [23, Appendix 4]. The absorption probability  $\mu(E_\perp)$  is given by

$$\mu(E_\perp) = 1 - |R|^2. \quad (17.1)$$

$R$  is

$$R = \frac{-\bar{M}_{21}}{\bar{M}_{22}} \quad (17.2)$$

and  $\bar{M} = \bar{M}_N \dots \bar{M}_2 \bar{M}_1$  is the product of the matrices  $\bar{M}_n$  for each boundary:

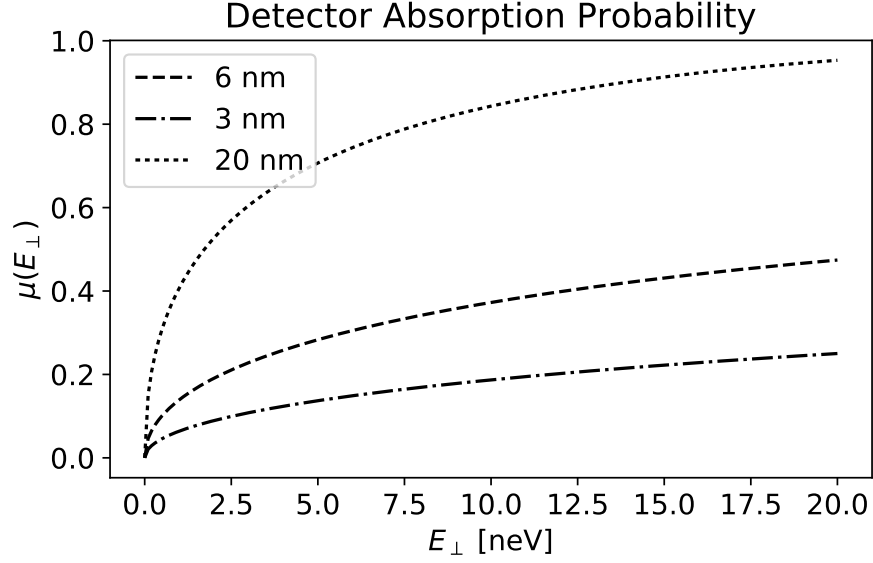


Figure 17.1: Loss probability on the detector as a function of perpendicular energy. UCN typically have  $E_{\perp} < 10$  neV.

$$\bar{M}_n = \frac{1}{2} \begin{bmatrix} (1 + \gamma_n)e^{i(k_{n-1}-k_n)z_n} & (1 - \gamma_n)e^{-i(k_{n-1}+k_n)z_n} \\ (1 - \gamma_n)e^{i(k_{n-1}-k_n)z_n} & (1 + \gamma_n)e^{-i(k_{n-1}+k_n)z_n} \end{bmatrix}, \quad (17.3)$$

where  $k_n = \sqrt{\frac{2m}{\hbar^2}(E_{\perp} - U_n)}$ ,  $\gamma_n = k_{n-1}/k_n$ ,  $z_n$  is the location of the  $n$ th boundary, and  $U_n = V + iW$  is the complex potential of the material. The imaginary part of the potential encodes the loss probability. The detector is modeled as a surface with a layer of  $^{10}\text{B}$  with thickness  $L_{10B}$  (approximately 5-10 nm) followed by a layer of ZnS with thickness  $10\mu\text{m}$ . The loss probability as a function of energy is given in Figure 17.1.

If a UCN is not absorbed, it is reflected 100% diffusively. The ZnS crystals on the detector surface are a polycrystalline powder with a particle size of approximately  $10\mu\text{m}$  [32]. The polycrystalline nature is expected to give totally diffusive scattering.

The detector was damaged in the experiment after dropping it onto the array several times. An additional modification of the loss probability  $\mu$  was added to account for the damage. The absorption probability is scaled linearly with  $\zeta'$ , so that at  $\zeta' = 0, \mu = 0$  (the bottom of the



detector), and at  $\zeta' = \zeta_{\text{cut}}, \mu = \mu(E_{\perp})$ . The absorption probability is

$$P(E_{\perp}, \zeta') = \begin{cases} \frac{\zeta'}{\zeta_{\text{cut}}} \times \mu(E_{\perp}) & 0 \leq \zeta' < \zeta_{\text{cut}} \\ \mu(E_{\perp}) & \zeta' \geq \zeta_{\text{cut}} \end{cases}. \quad (17.4)$$

The two cleaners in the trap are defined as shapes in the  $z = z_{\text{clean}}$  plane.  $z_{\text{clean}}$  is either 38 cm for cleaning or 43 cm for storage. For the large cleaner, the active area is the half-plane  $y > 0$ . For the active cleaner, the area is a rectangle  $-0.3897945 < x < 0.2706055; -0.7997415 < y < -0.4441415$ . The active cleaner was not simulated for the majority of studies; the smaller area was assumed to not contribute significant cleaning. If a UCN transits the  $z = z_{\text{clean}}$  plane, the  $x, y$  position is checked against the cleaners. If the cleaners were hit, then the UCN was absorbed.

### 17.3 SPECTRUM SETUP

UCN are created inside the trap near the trapdoor. They are created at the minimum potential height ( $z = -1.46441366913$ ) in a 15 cm×15 cm box centered at the origin.

A superthermal UCN source is expected to create UCN with density  $\propto E$  [23]. The conditioning of the guides is expected to weight the population towards higher energies. The density of UCN as a function of energy is assumed to be a power law,  $\rho \propto E^x$ .

The angular distribution of UCN exiting the open trapdoor is unknown. The magnetic fields and combination of specular and diffuse scattering inside the transition region is not simulated. The highest portions of the transition region are largely diffuse, so the phase space density was assumed to look like a lambertian which gives equal brightness in every direction. The cosine term in the distribution was additionally weighted by a power  $y$  to give the spectrum more forward-directedness.

Low-energy UCN can possibly escape the trap quicker than high-energy UCN. Low energy UCN spend more time closer to the trapdoor, so potentially have a higher chance to escape each time they cross the trapdoor. An energy cutoff was added to the spectrum to account for this

possibility.

The phase space density is given by

$$\rho(E, \theta_0) \propto \Theta(E - E_{\text{cut}}) E^x \sin(\theta_0) \cos^{1+y}(\theta_0), \quad (17.5)$$

where  $\Theta$  is the Heaviside step function,  $E$  is the energy of created UCN,  $E_{\text{cut}}$  is the low-energy cutoff,  $x$  is the power scaling of the spectral density,  $\theta_0$  is the angle with respect to  $+\hat{z}$ , and  $y$  is the forward-directedness scaling. Because the loading process is not simulated, this phase space distribution is expected to match the distribution of UCN inside the trap after the trapdoor is closed.

To simulate the effects of loading, UCN were created with the truncated exponentially distributed loading time found in Section 12.2. After birth, they were tracked for their filling time before the experiment time began at  $t = 0$ , corresponding to the trapdoor closing time. During this time they can evolve in phase space and be cleaned.

## 17.4 $\chi^2$ COMPARISON OF HISTOGRAMS

The 5 parameters ( $L_{10B}$ ,  $\zeta_{\text{cut}}$ ,  $E_{\text{cut}}$ ,  $x$ ,  $y$ ) were varied to minimize the  $\chi^2$  between data and simulation histograms. Histograms of the rate in the 9-step runs were used to tune the simulation. In order to avoid expensive simulations, the data was re-weighted from an initial, general dataset. The initial dataset used  $x = 1$ ,  $y = 0$ ,  $E_{\text{cut}} = 0.5$  neV. Each UCN was weighted with an additional factor to obtain the phase space density in Equation 17.5.

The simulation output contained the first 50 arrival times and perpendicular energies on the dagger for each UCN. Each UCN was tracked, and every time it hit the dagger the time, location, and perpendicular energy was stored. The UCN was then reflected diffusely and tracked until the next dagger hit.

The raw data produced in this way can be used to simulate different detector surface models. During post processing, the absorption process is simulated and the first hit to be successfully

absorbed is recorded into an arrival time histogram. In this way, the results can be re-used and the  $\chi^2$  space mapped out quickly.

The  $\chi^2$  was calculated on a bin-by-bin basis comparing a weighted histogram from the simulation and an unweighted data histogram [56]. This method is used in the ROOT data analysis framework to compare histograms.

The minimum  $\chi^2$  was found using the Covariance Matrix Adaptation Evolutionary Strategy (CMA-ES) minimization technique [57]. This technique is expected to perform well on noisy objective functions with many local minima. The  $\chi^2$  of 2 histograms is likely to be noisy and with many minima because the underlying data is discrete. Changing the parameters of the model will change the contents of the bins in discrete steps, so small local maxima and minima may be present.

The minimum search was conducted in 47 trials. The lowest  $\chi^2$  value of all the trials was chosen as the best fit. Approximately 2/3 of trials converged to a distinct point with a  $\chi^2$  0.01 higher. Each trial had a population size of  $\lambda = 8$  and terminated at a relative difference of  $1 \times 10^{-6}$  in  $\chi^2$ . The minimum was found at  $L_{10B} = 5.8$  nm,  $\zeta_{\text{cut}} = 1.6$  cm,  $E_{\text{cut}} = 7.6$  neV,  $x = 1.3$ ,  $y = 0.26$  at a value of  $\chi^2/\text{NDF} = 17.3$ . A comparison of the data and Monte Carlo simulations can be seen in Figure 17.2.

The  $\chi^2$  contours were explored by varying a pair of parameters around the minimum and mapping out the  $\chi^2_{\text{min}} + 1$  boundaries in a grid search. The results can be seen in Figure 17.3. Most parameters are seen to be correlated, especially with parameters of like type (spectrum to spectrum or detector to detector). The largest correlation is between  $L_{10B}$  and  $\zeta_{\text{cut}}$ . As the Boron thickness increases, the cutoff decreases so that the time constant is not changed significantly during the middle counting steps. The scaling of forward-directedness  $y$  and  $E_{\text{cut}}$  is also seen to be about as correlated. This is likely due to the last peak. A lower population in the last peak due to a higher cutoff can be counteracted by more UCN at shallow angles. These high  $\theta_0$  orbits are more likely to be counted during the last step than orbits with low  $\theta_0$ .

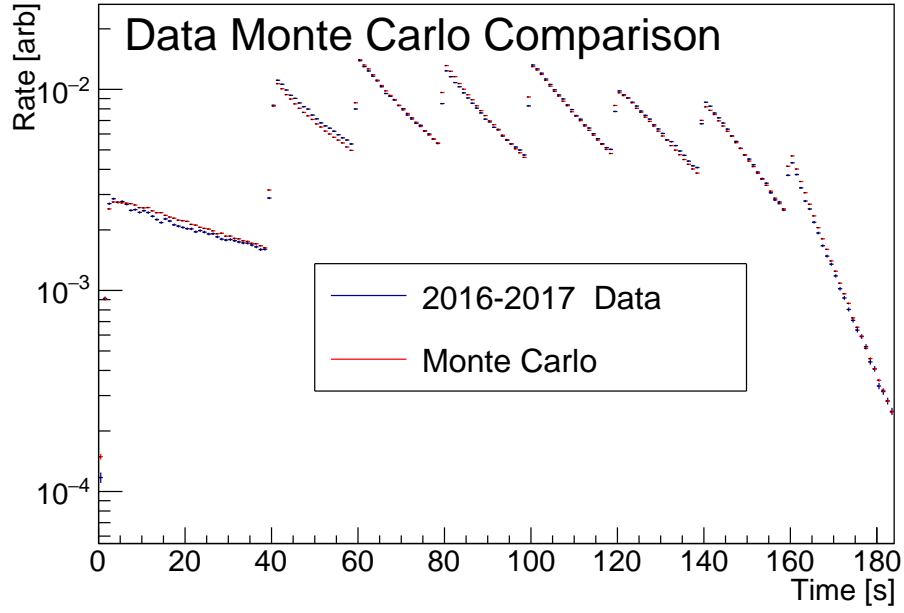


Figure 17.2: Comparison of 2016-2017 data with best-fit Monte Carlo simulations

The simulation is seen to prefer a high-energy enhanced spectrum ( $x > 1$ ) that's forward-directed ( $y > 0$ ). It also prefers a thin layer (the nominal thickness was approximately 10 nm), and a damaged region that's roughly consistent with the damage to the detector of  $\sim 1$ -2 cm.

The optimum values of the 5 parameters were additionally used on 3-step data for validation. The 3-step data was simulated without further optimization and qualitatively agrees with the data. Initial trials of the 3-step data revealed the time constant of the final step being too slow. This prompted the inclusion of the damaged portion of the detector. UCN strike the detector at a higher  $\zeta'$  during the final step, so the damaged portion allows UCN to be drained slower during the higher steps and faster on the last step. However, no optimization was done on this dataset. The results can be seen in Figure 17.4

The  $\chi^2/\text{NDF}$  is  $\sim 76$  for the 3-step data. The Monte Carlo simulation lags behind the data, hinting at timing differences driving deviations. Additionally, the data histogram is a composite of 153 runs taken over several weeks. Spectral variations are expected between runs due to degradation or source rebuilding. The detector actuator may have been reset which can subtly change the

# $\chi^2$ Contours

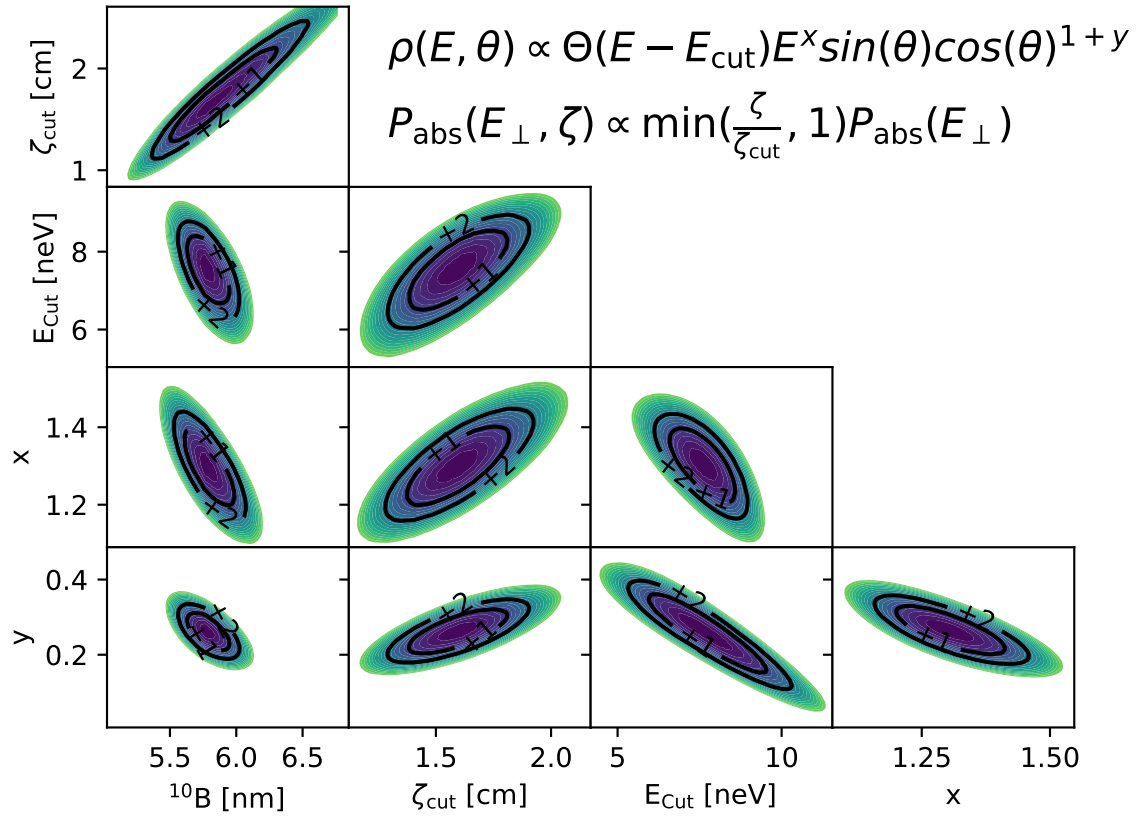


Figure 17.3: Contours of  $\chi^2$ .

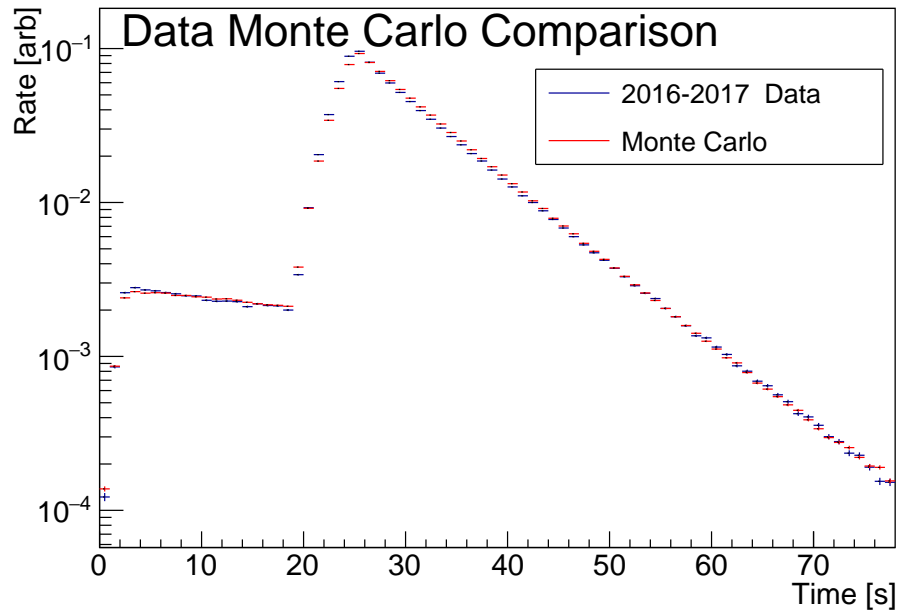


Figure 17.4: Comparison of 2016-2017 data with Monte Carlo simulations using optimum 9-step parameters.

position. Additionally, any timing variations or friction in the actuation can cause non repeatability of actuation. These factors may compound together and cause difficulty in matching the data well. However, qualitatively the simulation matches the draining time constants and population sizes of the data and also captures the draining time constants and population sizes when the latter 7 steps are compressed into one.

## CHAPTER 18

### SIMULATION OF HEATING AND CLEANING EFFECT ON $\tau$

#### 18.1 LIFETIME MEASUREMENT SETUP

Simulation of a 0.7 s precision dataset takes approximately 2000 CPU hours. Simulating higher precision ( $<0.1$  s) becomes computationally expensive quickly. However, Monte Carlo techniques allow complete knowledge of UCN history and therefore a quicker calculation of the shift in lifetime. The shift in lifetime can be estimated by measuring the number of UCN which are lost during storage. Because the number of UCN being lost is measured, the statistical uncertainty comes from the size of the lost population and not the measurement of  $\tau$ . The effect of uncleaned UCN or heated UCN is estimated using the lost population.

Heating was studied by simulating a full lifetime run with comparable statistics to the 2016-2017 dataset (approximately 5 million UCN in the short run). The shift in lifetime is given by

$$\delta\tau = \tau - \tau' = \left[ \Delta T / \log \left( \frac{N_{\text{short}}}{N_{\text{long}}} \right) \right] - \left[ \Delta T / \log \left( \frac{N_{\text{short}}}{N_{\text{long}} + N_{\text{lost}}} \right) \right], \quad (18.1)$$

where  $N_{\text{short}}$  is the sum of counted UCN in the short run,  $N_{\text{long}}$  is the sum of counted UCN in the long run, and  $N_{\text{lost}}$  is the number of UCN lost during storage which would not  $\beta$  decay before the beginning of the counting period. The  $\beta$  decay time for each UCN is determined at the beginning of the run so it is easy to determine which UCN would have otherwise decayed. The uncertainty in  $\delta\tau$  can be found via typical Gaussian propagation techniques.

Cleaning was studied by simulating only UCN above cleaning height and counting the number of

UCN which were destroyed during storage. In this simulation  $\beta$  decay was turned off to increase the number of neutrons that can be simulated per CPU-hour. The number of UCN lost during storage is then interpreted as a shift in the initial population. The shift in lifetime for this simulation is given by

$$\delta\tau = \tau - \Delta t / \log \left( \frac{1}{\exp(-\Delta t/\tau)(1-f)} \right), \quad (18.2)$$

where  $f$  is the fraction of the initial population lost during storage and is given by

$$f = \frac{N_{\text{lost}}}{N_{\text{counted}}} \simeq \frac{N_{\text{lost}}}{N_{\text{simulated}}} \times \frac{N_{\text{cleanable}}}{N_{\text{trappable}}}, \quad (18.3)$$

where  $N_{\text{lost}}$  is the sum of UCN lost during storage on the cleaner,  $N_{\text{counted}}$  is the number of UCN which would be counted in a short storage run given the simulated population size,  $N_{\text{simulated}}$  is the total number of cleanable UCN simulated, and the fraction  $\frac{N_{\text{cleanable}}}{N_{\text{trappable}}}$  is the sum of the spectrum that is cleanable over the sum of the spectrum that is trappable. Only cleanable UCN are simulated, so the fraction  $\frac{N_{\text{cleanable}}}{N_{\text{trappable}}}$  is taken from integrals of the spectrum (Equation 17.5).

## 18.2 HEATING MODEL

One possible source of heating is microphonic vibrations of the array. Heating via microphonic vibrations is added to the simulation by using a time-dependent wall potential. Time dependence is added to the symplectic integrator by adding time into an extended phase space. For some potentials, this simplifies to stepping time like the  $x, y, z$  coordinates during each integration step [50]. To simulate vibration, the  $x, y, z$  coordinates are shifted as a function of time, becoming  $x_0 + \delta x(t), y_0 + \delta y(t), z_0 + \delta z(t)$ . The gravitational  $z$  coordinate is not shifted.

The vibrations  $\delta x(t), \delta y(t), \delta z(t)$  are obtained from accelerometer data on the vacuum vessel. A 40 s long trace of  $a_x(t), a_y(t), a_z(t)$  was used to calculate the displacements. The accelerometer data was taken by a third party in 3 configurations: one background and 2 foreground (with different pieces of equipment on). The Fourier Transform of the accelerometer data was taken. The phase of



a strong background line (29.575 Hz) was determined in each trace. The phase for each trace was then adjusted so that the phase of the 30 Hz line agreed between datasets. Then the low-frequency components ( $<5$  Hz) were filtered out by setting their frequency bins to 0 amplitude. Then a double time integration was performed in the frequency domain. A time window was defined between the lowest observed total displacement and the last instance of a total displacement less than 30 nm. A windowing function was then applied so that vibrations gradually fade in and out at the beginning and end of the time window. An approximately 28 s long  $x, y, z$  displacement trace was obtained. The displacements  $\delta x(t), \delta y(t), \delta z(t)$  were then linearly interpolated between sampling points and cyclically sampled during the simulation. The largest displacements are approximately  $1 \mu\text{m}$ .

The coupling of vibration of the magnetic fields to UCN heating depends on the perpendicular momentum of an incident UCN, the vibration phase, and frequency. The heating response was measured by dropping UCN from a defined height at  $(0, 0, z_{\text{drop}})$  and varying the height, phase, and frequency. The highest  $\Delta E$  for each height and frequency gives the response. The largest response is at  $\sim 30$  Hz; the maximal frequency is lower as the UCN energy is lower. There is also a smaller lobe due to multiple oscillations during transit at 150 Hz. In general, frequencies higher than 100 Hz are unimportant to the heating. Low frequency vibrations are problematic. The results can be seen in Figure 18.1.

### 18.3 CLEANING AND HEATING RESULTS

The cleaning was simulated using 4 different scenarios: 50s cleaning with 100% absorption per bounce on the cleaner or 50% absorption per bounce on the cleaner, 200s cleaning at 100% absorption, and 50s where the lowered cleaner height was 3 cm lower than nominal (with the same 43 cm raised height).

Heating was simulated using the measured accelerometer data, measured accelerometer data amplified by 40 times, and accelerometer data amplified by 80 times. Results are given in Table 18.1.

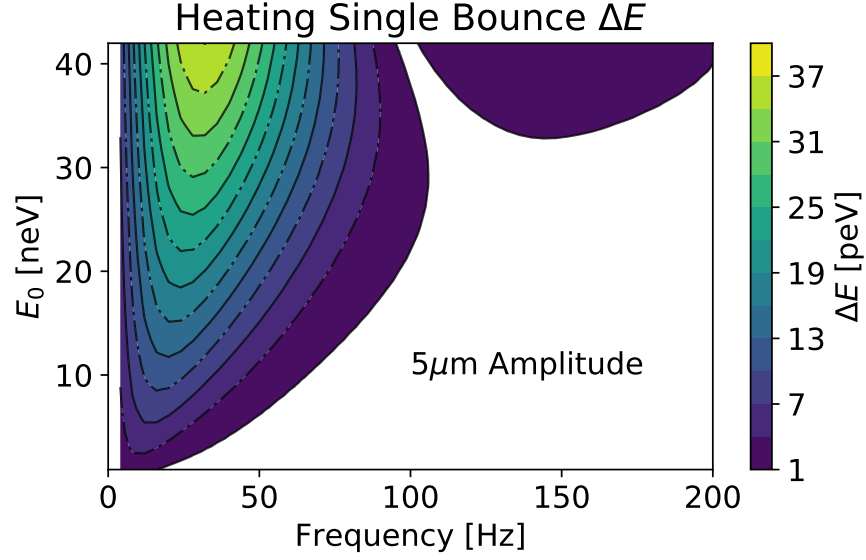


Figure 18.1: Maximum energy gain during one bounce with a 5 $\mu$ m sinusoidal vibration

Set	$\delta\tau$ [s]	Statistical Uncertainty [s]
<b>Cleaning</b>		
100% Absorption	0.034	0.0006
50% Absorption	0.050	0.0007
200 s Cleaning	0.0017	0.0001
35 cm Cleaning	$8 \times 10^{-5}$	$3 \times 10^{-5}$
<b>Heating</b>		
Accelerometer	0.031	0.005
x40 ( $\sim 40\mu$ m)	0.151	0.009
x80	7.68	0.06

Table 18.1: Shift in  $\tau$  due to insufficient cleaning or heating during storage

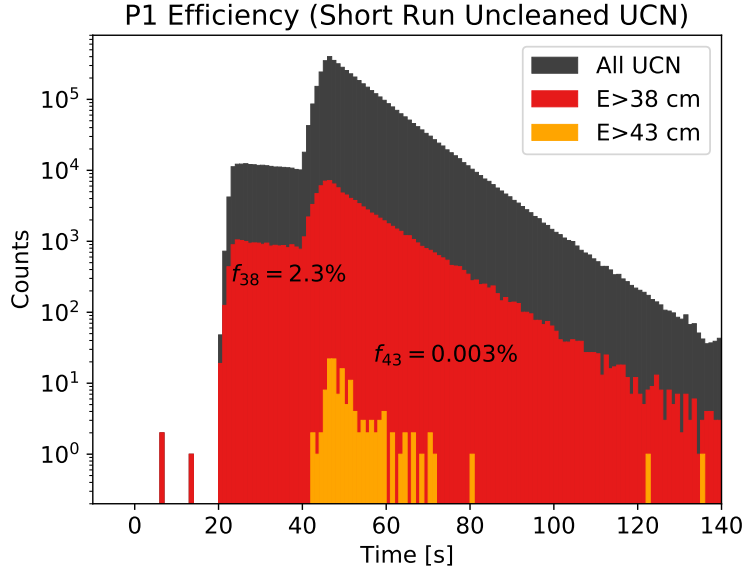
The shift in  $\tau$  is small for nominal cleaning; it is most likely less than  $\sim 0.05$  s. The cleaner is fairly thick and made of polyethylene (which has a slightly negative potential). The efficiency of a polyethylene absorber is expected to be close to unity for UCN  $E > 5$  neV [58]. The exact efficiency depends on details of the surface (contamination and geometry) and is unknown for the cleaner. UCN with energy above the raised cleaner have 5 neV of total kinetic energy at the cleaning height. Their perpendicular energy is  $< 5$  neV which may cause a slightly lower than unity absorption efficiency.

Increasing the cleaning time to 200 s reduces the loss of UCN during storage by a factor of 20. Maintaining the cleaning time of 50 s and lowering the cleaning height to 35 cm reduces by another factor of 20.

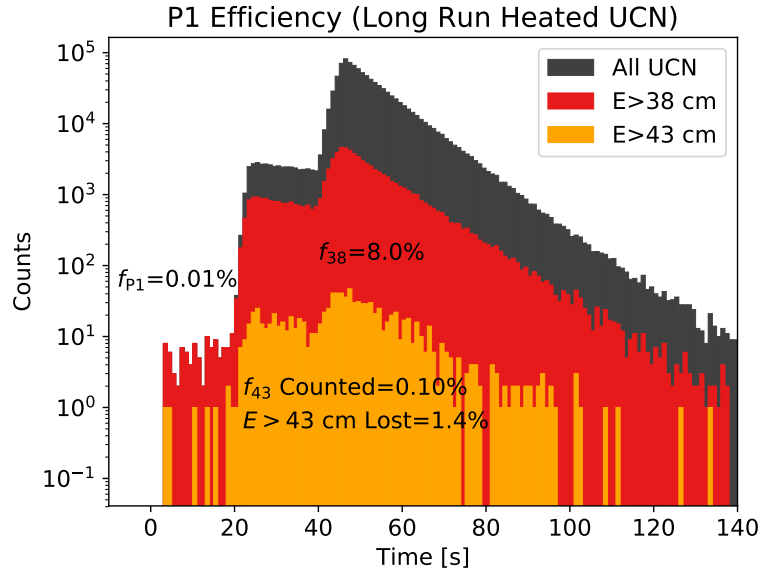
The effect of heating is also small. The measurements were taken on the vacuum jacket so there is a possibility of larger vibrations on the array itself, or alternate modes such as rotations. Further accelerometer data needs to be taken across the array in a variety of conditions in order to make a more precise estimate of the effect of microphonic heating. Regardless of the uncertainties in cleaning efficiency or heating amplitude, the effects are expected to be small compared to the statistical uncertainty.

## 18.4 HEATED UCN DETECTION EFFICIENCY

The results in Section A.3 rely on the estimate of the total number of high-energy UCN in the trap using the number of UCN counted above the cleaning height. The Monte Carlo simulations can determine whether or not this correction works. The effectiveness of this correction is tested by comparing the sum of counted uncleaned or heated UCN between the simulations and data. The statistical uncertainty of the 2016-2017 dataset was 0.7 s and the statistical uncertainty of the simulated 80x heating was 0.6 s. An additional no heating simulation was done with a precision of 0.4 s. The arrival time of uncleaned UCN can be seen in Figure 18.2a and the arrival time of heated UCN can be seen in Figure 18.2b.



(a) Arrival time of UCN on the detector split by energy group for uncleaned UCN.



(b) Arrival time of UCN on the detector split by energy group for heated UCN. 1.4% of UCN are lost due to heating.

Figure 18.2: Efficiency of counting UCN in Peak 1.  $f_{38}$ ,  $f_{43}$ , and  $f_{P1}$  are the number of UCN counted with  $E > 38$  cm,  $E > 43$  cm, and in Peak 1 normalized to the total population (gray).

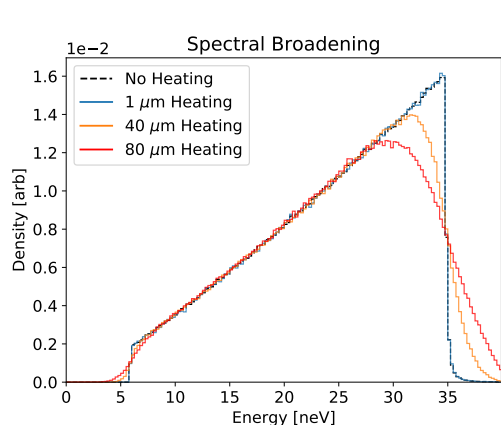
The arrival time of UCN is split between  $E > 43$  cm (orange),  $E > 38$  cm (red), and all UCN (gray). For uncleaned UCN, no neutrons are counted at the cleaning height. Almost all  $E > 43$  cm UCN are lost during storage, leading to the 0.03 s shift. UCN with  $E > 43$  cm are also missing from the 2nd step. These UCN are likely high- $\theta_0$  UCN which are associated with periodic orbits that have long cleaning times. These orbits are also more likely to be counted during the last step than during steps 1 or 2.

For the 80x heating scenario, the sum of UCN counted in the first step is 96. This is consistent within uncertainty with the number measured in Section A.3. However, the shift in lifetime for this scenario is 7.68 s, significantly larger than the estimate from the 2016-2017 data. The simulation gives a scenario where the observed number of counts in peak 1 is small, but the shift in lifetime is large. These simulations suggest that measuring the population of UCN at the cleaning height does not give enough information about the number of high-energy UCN in the trap.

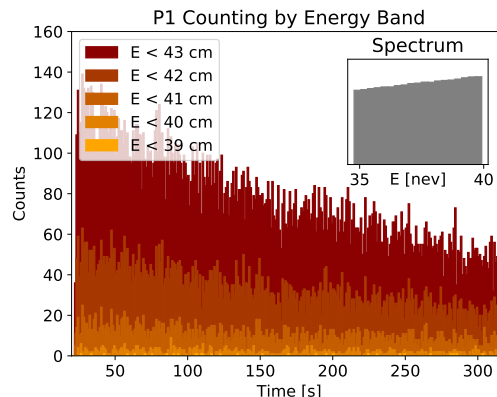
Regular orbits which skim on the bottom of the trap and do not deviate far in  $\zeta$  may cause part of the difficulty in detecting high-energy UCN. These orbits are approximately half the orbits in the trap at high energies, causing at least half of the trajectories to not be counted. Additionally, spectral broadening as seen in Figure 18.3a can also help explain difficulties in measurement. Half of the heated UCN are within 1.5 cm of the lowered cleaner height after significant heating. This is approximately the width damaged portion of the detector, which will count significantly fewer neutrons than the higher portions.

The reduced counting efficiency as a function of energy can also be seen by splitting the arrival time by energy band. A simulation of the data in Section 12.6 was performed. The counting period was then split up into different energy bands seen in Figure 18.3b

The lowest energy group ( $E < 39$  cm) contributes only a few counts; The next highest group ( $E < 40$  cm) contributes  $< 5\%$  of the counts. If the detection efficiency is the same across energy bands, then these two populations should contribute  $\sim 40\%$  of the counts. Because the density of heated UCN linearly drops with height, the efficiency of counting them will be significantly



(a) Effects of heating on the spectrum of UCN



(b) Efficiency of counting UCN at the cleaning height by energy

Figure 18.3: Effects of heating on the UCN spectrum and spectrum on counting efficiency.

reduced.

This result indicates that the assumptions in Section A.3 are incorrect. The high-energy population cannot be measured at the cleaning height to determine the heated or uncleaned population. The results using this detection method are therefore discarded in the lifetime result. However, the size of the shift in  $\tau$  due to heating is still expected to be small for nominal vibrations in the trap.

## 18.5 ARRIVAL LOCATION OF UCN ON CLEANER AND DAGGER

The arrival location of UCN on the cleaner and detectors was also studied. The arrival position on the cleaner shows a large amount of structure. The arrival location of UCN with low  $\theta_0$  is significantly different than that of UCN with high  $\theta_0$ . High  $\theta_0$  was defined as  $\theta_0 > 0.9$  and low as  $\theta_0 < 0.6$ . The arrival location of late-time UCN is also significantly different than the arrival location of short-time UCN. The simulation results can be seen in Figure 18.4.

The high  $\theta_0$  and low  $\theta_0$  are qualitatively different. There is significant structure in high  $\theta_0$ , possibly due to the prevalence of periodic orbits in that part of phase space. The hot spots from

low  $\theta_0$  are not understood. These orbits may take longer to be absorbed if the cleaner edge was significantly far from  $y = 0$ . However, these orbits are typically associated with chaotic orbits as seen in Section 20.2 so they may be cleaned quickly regardless.

The late arrival UCN are also different from early UCN. The late UCN show more structure, indicating a higher presence of periodic orbits. Additionally, the hot spots on the cleaner are not present at long times, indicating that they are associated with quickly cleaned UCN.

The arrival profile on the dagger detector for the 3-dip data can be seen in Figure 18.5. The  $x, z$  coordinates are a sum of the 2 dips and the dips are separated in the secondary histogram. The arrival  $\zeta'$  for the 2nd dip is peaked at 1.6 cm, corresponding with the detector damage  $\zeta_{\text{cut}}$  value. Here UCN preferentially absorb as close to the edge as possible, but are mitigated by the damage. During the last dip, the peak  $\zeta'$  is around 2.5 cm which is the height of the trap's minimum potential on the dagger. Below this  $\zeta'$ , UCN lose energy to the magnetic field and so are most likely to be absorbed at the minimum potential point.

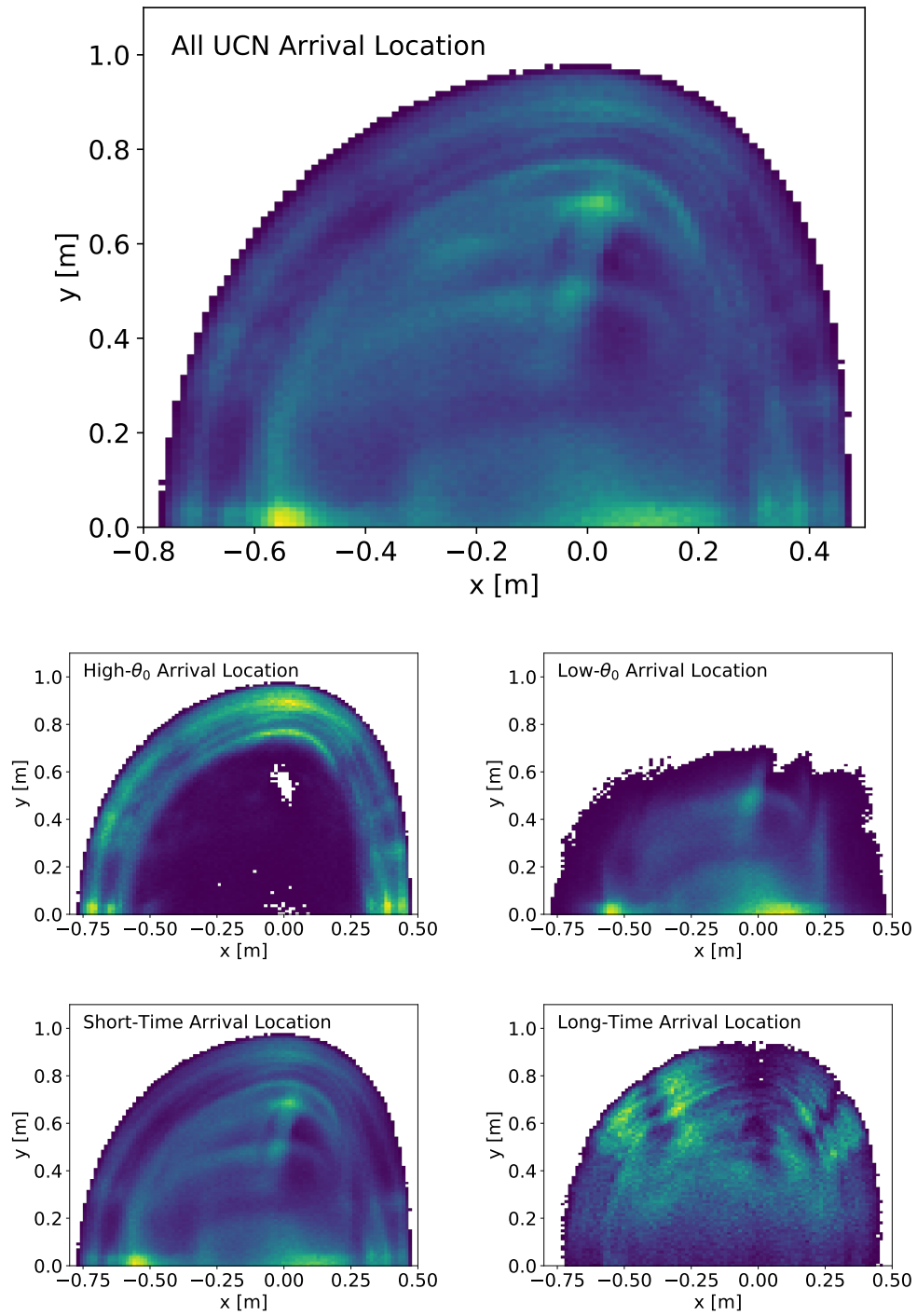


Figure 18.4: Arrival location of UCN on the large cleaner



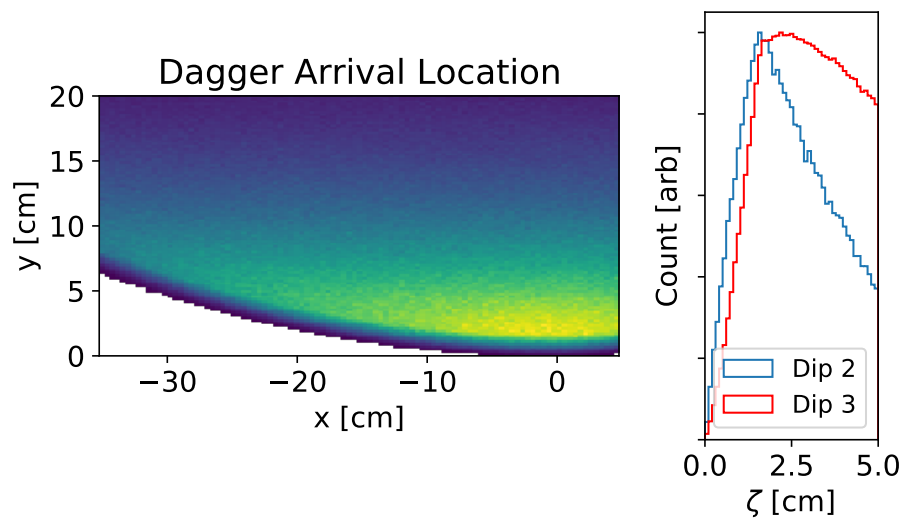


Figure 18.5: Arrival location of UCN on the dagger detector

## CHAPTER 19

### SIMULATION OF PHASE SPACE EVOLUTION

#### 19.1 PHASE SPACE EVOLUTION DATA

Several phase space evolution (PSE) runs were taken during the 2016-2017 run cycle. One set of dedicated PSE runs were studied. Additionally, a set of counting time constant runs were studied. If the trap simulation captures the physics of the experiment, the phase space evolution should be recovered. The run configuration can be seen in Figure 19.1.

The PSE runs inserted the dagger 13 cm below the cleaner during the cleaning process. This eliminates a large number of trappable UCN. Only a subset of UCN in the trap are eliminated; some UCN are in orbits that do not intersect the dagger when it is 13 cm below the cleaner. This creates a hole in phase space. When the dagger is re-inserted during the counting period, the population in the 2nd peak is diminished due to the cleaning. However, during the storage period

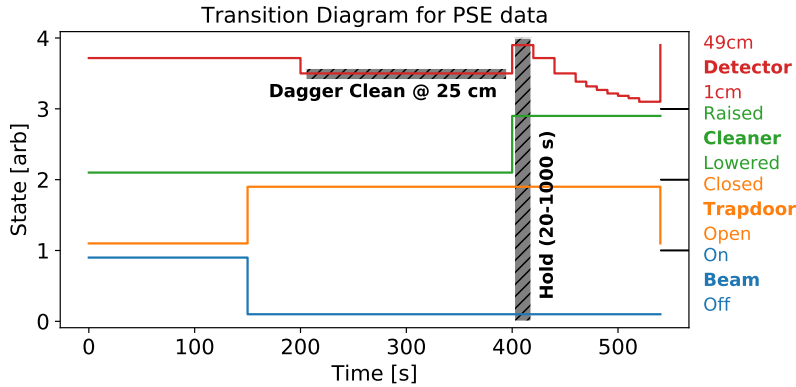


Figure 19.1: Run configuration for phase space evolution Data

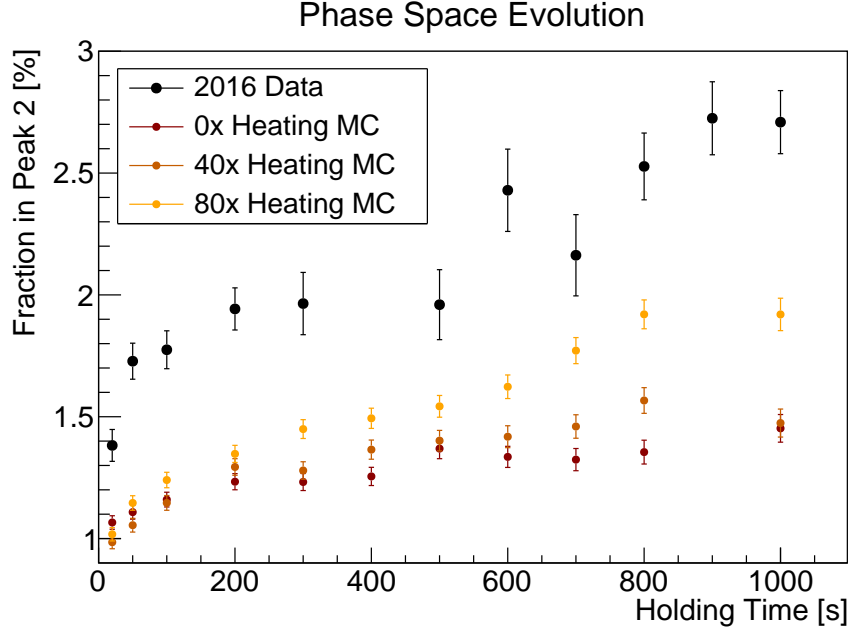


Figure 19.2: Phase space evolution data/Monte Carlo simulation comparison

UCN can evolve into orbits which do intersect the dagger and the population in the 2nd peak will increase as a function of storage time. This can be seen in Figure 19.2.

The fraction of UCN in peak 2 increases by almost double as storage time is increased. However, the simulation does not capture the relative population sizes seen in the data. The growth over time is also significantly smaller. Heating was also added into the simulation to see if heating UCN to higher orbits will introduce the needed growth over time. Heating adds in a significant amount of growth, but the relative population sizes are still low. The mismatch in the population sizes and growth over time suggest that there is some mechanism that mixes orbits in the physical trap that is not present in the simulation.

## 19.2 PHASE SPACE EVOLUTION IN LIFETIME DATA

Phase space evolution can also be tested for in production lifetime data. One way to test PSE in lifetime data is to separate the lifetime measurement by dip. By calculating  $\tau_n$  from the 2nd dip and 3rd dip, differences in the fraction of UCN counted at each height cause shifts in the lifetime.

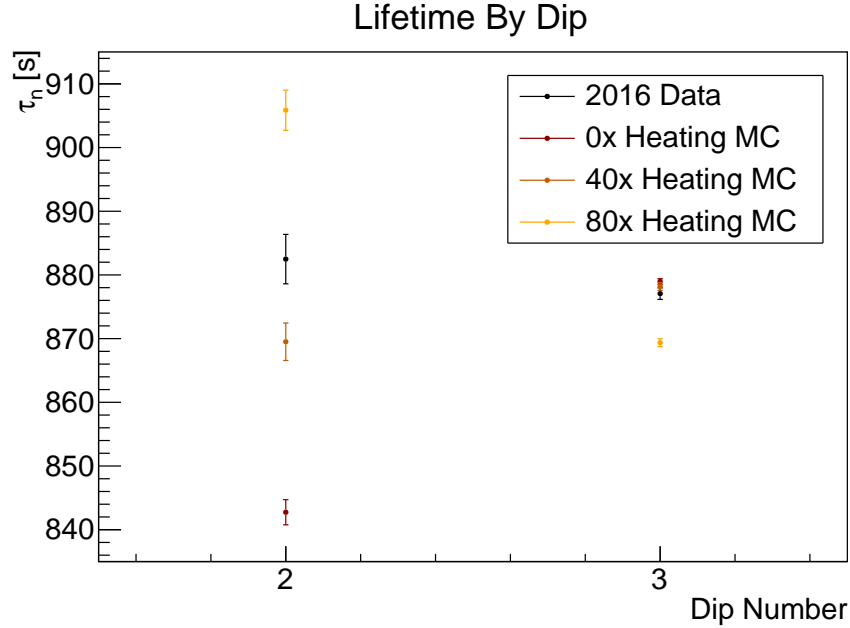


Figure 19.3: Lifetime By Dip for data/Monte Carlo simulations

The lifetime separated by dip can be seen in Figure 19.3.

The simulation has a significantly different lifetime in the 2nd dip than the data. In the simulation, the lifetime is significantly shorter, indicating a higher efficiency for counting at short times compared to long times. Heating tends to redistribute UCN to higher peaks, and this masks the PSE signal. At a level of 40x heating, the lifetimes are almost the same between the 2nd and 3rd peaks. This is additional evidence that the phase space evolution or initial phase space distribution is not accurate in the simulation.

### 19.3 COUNTING TIME CONSTANT

Another manifestation of phase space evolution and the initial distribution of UCN in Phase space is the counting time constants. Several dedicated time constant measurements were made during the 2016-2017 run cycle. The basic configuration was a 9-dip measurement where the counting was paused at one height to measure the time constant for several hundred seconds. The timing diagram is given in Figure 19.4

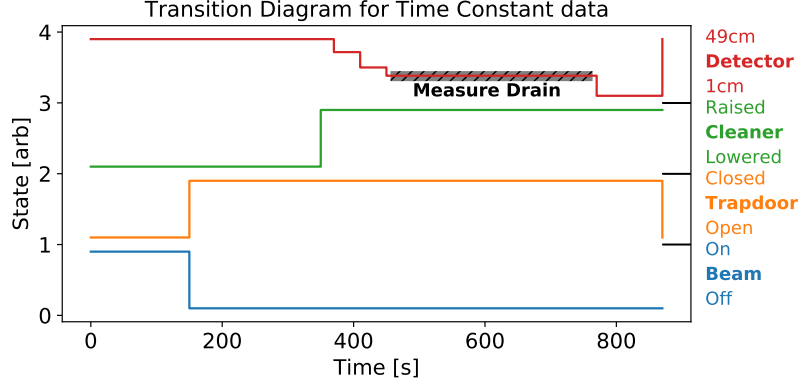


Figure 19.4: Run configuration for Time Constant Data

The time constants were measured in Section 12.3 to be between 40 s at the longest to 7 s at the shortest. Comparison of the time constant at each height in the trap can be found in Figure 19.5. The simulations shows two significant differences from the data: 1) a missing long-time component and 2) an excess of counts during the last step. The first could be evidence for missing phase space evolution in the data and the latter could be an indication of an excess of UCN at high  $\theta_0$ . The UCN counted during the last step are associated with high  $\theta_0$ . When these UCN are filtered out, the last step in the simulation disappears, which is consistent with the data. This can be seen in Figure 19.6.

A process which takes high- $\theta_0$  orbits and mixes them into the normal trap population during the storage period could also cause this effect. Irregularities in the actual trap potential may drive these transitions and cause the other phase space evolution effects needed to make the simulation match the 2016 dataset.

## Time Constant Data

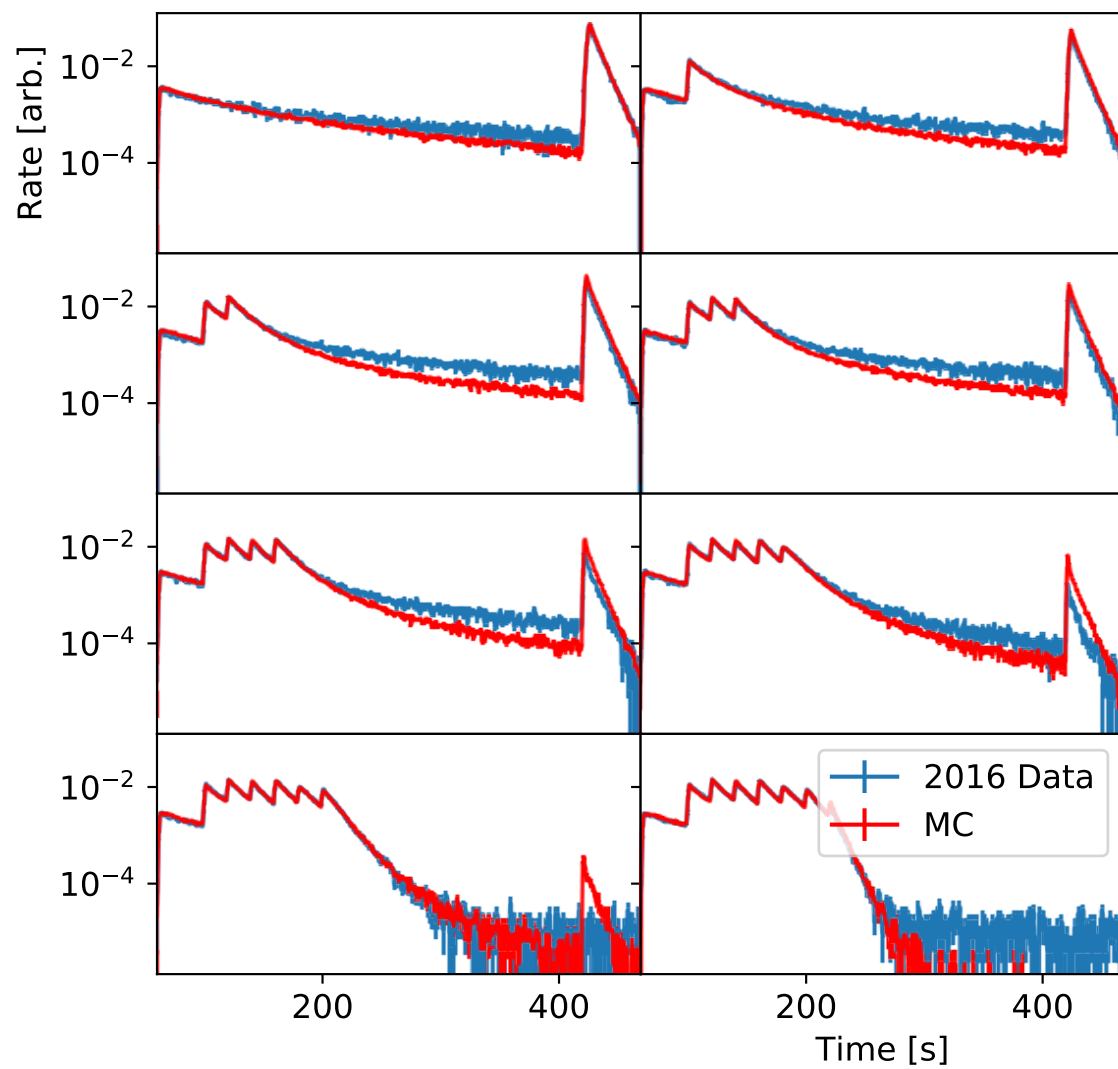


Figure 19.5: Comparison of data to Monte Carlo simulations with time constant dataset

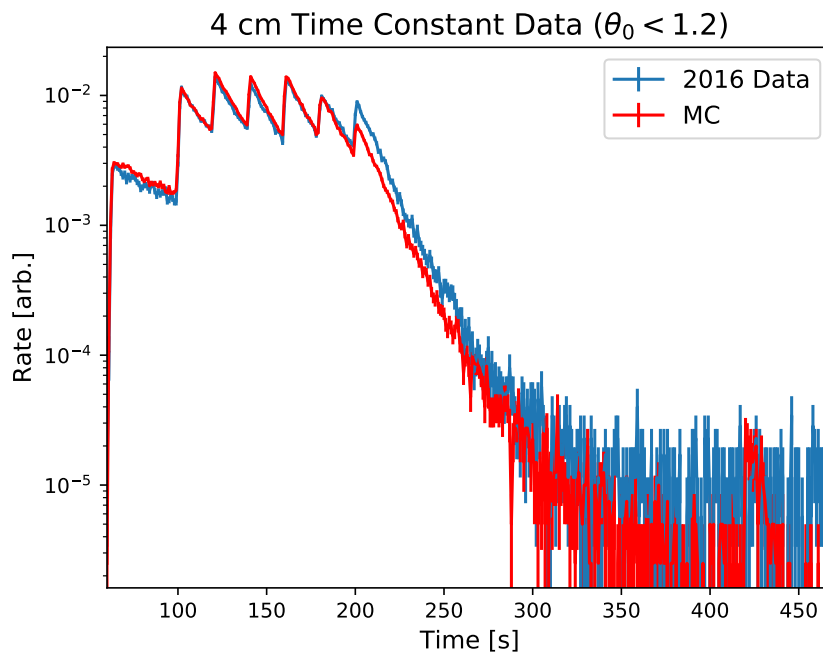


Figure 19.6: Comparison of data to Monte Carlo simulations with time constant at 4 cm and  $\theta_0 < 1.2$

## CHAPTER 20

### LYAPUNOV EXPONENTS

#### 20.1 LYAPUNOV EXPONENTS

In strongly chaotic systems, trajectories are ergodic and have the property that they fill phase space (they come arbitrarily close to any point in phase space) and nearby trajectories exponentially diverge. In the context of  $\text{UCN}\tau$ , arrival on the cleaner can be considered a point in phase space. Chaotic trajectories are then guaranteed to eventually interact with the cleaner and be lost. A trajectory on a periodic orbit may never visit the cleaner and therefore not be cleaned.

In mixed dynamics systems, chaotic trajectories can exist close to (but outside of) regular tori and the rate of escape can be limited [59]. These trajectories will still fill phase space however. In the context of  $\text{UCN}\tau$  these trajectories can exist close to the regular tori in phase space during the cleaning time but then reach the cleaner during storage.

It is therefore possible to gain insight into the cleaning process by studying the chaotic behavior of the system. If the fraction of chaotic UCN trajectories in the trap is sufficiently high, then every trajectory is guaranteed to be cleaned. If the fraction of semi-periodic (regular) orbits is high, then some trajectories may become problematic during storage.

Some superconducting lifetime traps contain radially symmetric potentials [60], which potentially can have long-lived regular orbits. High-energy UCN with sufficient energy in angular momentum about the axis of symmetry could be trapped for long periods of time. The  $\text{UCN}\tau$  apparatus was given asymmetry in an attempt to mediate this effect.



Lyapunov characteristic exponents (LCE) were used to study the chaotic nature of trajectories. LCE can be measured in numerical simulations by tracking perturbed trajectories and measuring their divergence [61]. The procedure to measure the LCE is to start with an initial trajectory, perturb it by a small distance  $\epsilon$  in phase space, track both trajectories independently for a time  $\Delta t$ , then measure the distance between them  $\delta$ . The quantity associated with the LCE is given by

$$k = \frac{1}{N\Delta t} \sum_{i=1}^N \ln \left( \frac{|\vec{\delta}_i|}{\epsilon} \right), \quad (20.1)$$

where  $N$  trials are done.

After each trial, the partner trajectory is reset to a distance  $\epsilon$  from the reference trajectory.  $\delta$  was measured by scaling the distance of each coordinate by the region of allowed phase space (for example,  $\delta y$  was scaled by 35 cm, roughly scale of phase space available in  $y$ ). This normalization allows the momentum and distance coordinates to contribute equally. As  $N\Delta t$  approaches  $\infty$  and  $\epsilon$  approaches 0,  $k$  approaches the LCE. Values of  $k$  near zero are considered regular and values of  $k > 0$  are considered chaotic.

Initial partner trajectories were defined by adding a small amount of momentum in the direction perpendicular to the initial momentum and subtracting a small amount of momentum parallel so that both energy is conserved and the distance is  $\epsilon$ . After the initial separation is tracked for  $\Delta t$ , the partner trajectory is reset by shrinking the separation along  $\vec{\delta}$  so that it is separation is  $\epsilon$ .

UCN were tracked with an initial separation of  $\epsilon = 1 \times 10^{-9}$ ,  $\Delta t = 5$  s, and  $N = 100$ . Qualitatively, the distribution of  $k$  did not change with increasing  $\Delta t$ ,  $N$ , or  $\epsilon$ , indicating stable characterization of trajectories. The value of  $k$  was unstable for a given trajectory as noted in Section 16.3, but trial trajectories did not change from regular to chaotic or vice-versa.

## 20.2 LYAPUNOV RESULTS

The LCE of 2 million trajectories was calculated. The UCN were created in the trapdoor box with a flat energy distribution and isotropic  $\theta_0$  distribution. Data was later weighted to match the input

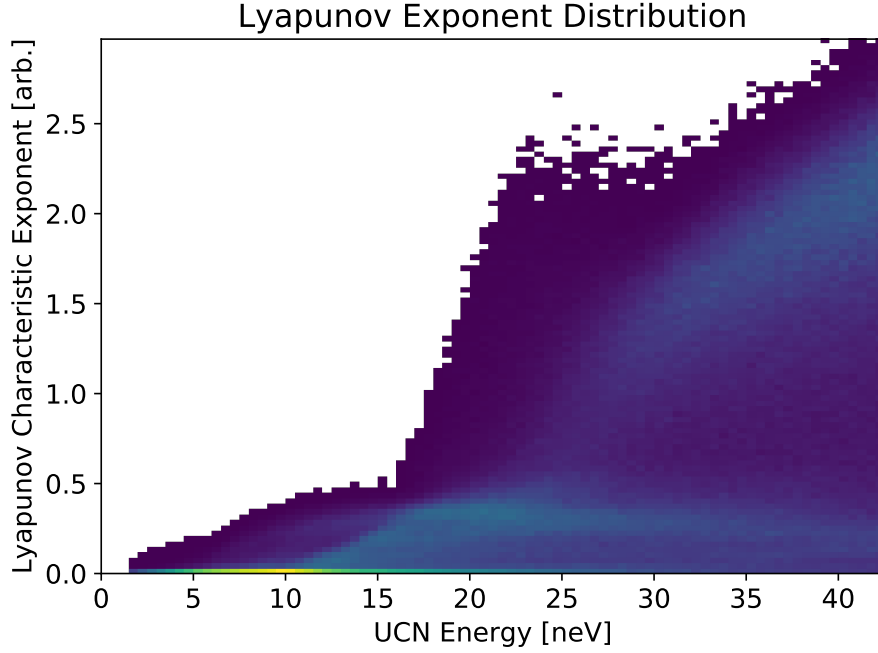


Figure 20.1: 2D histogram of LCE and energy inside the trap

spectrum found from the  $\chi^2$  minimization. Trajectories with  $E > E_{\text{clean}}$  were later re-simulated on a personal computer to measure the cleaning time. The overall distribution of LCE in the trap can be seen in Figure 20.1.

Three important features of the distribution are that 1) chaotic behavior begins at an energy of approximately 25 neV, 2) about half of the trajectories in the trap at cleaning energies are chaotic, and 3) there is a region of mixed dynamics where chaotic trajectories are close to regular ones.

The rise in  $k$  as a function of energy can be explained by high-energy trajectories having more phase space available. The separations  $\delta$  can be larger and therefore the normalization is not exact.

Regular trajectories can be cleaned quickly if their orbits intersect the cleaner. For orbits which do not, their cleaning time can possibly be very long. The cleaning time can be seen in Figure 20.2.

The important feature to note is that regular trajectories are associated with a long time constant. Trajectories that remain uncleaned in the trap are significantly more periodic than the

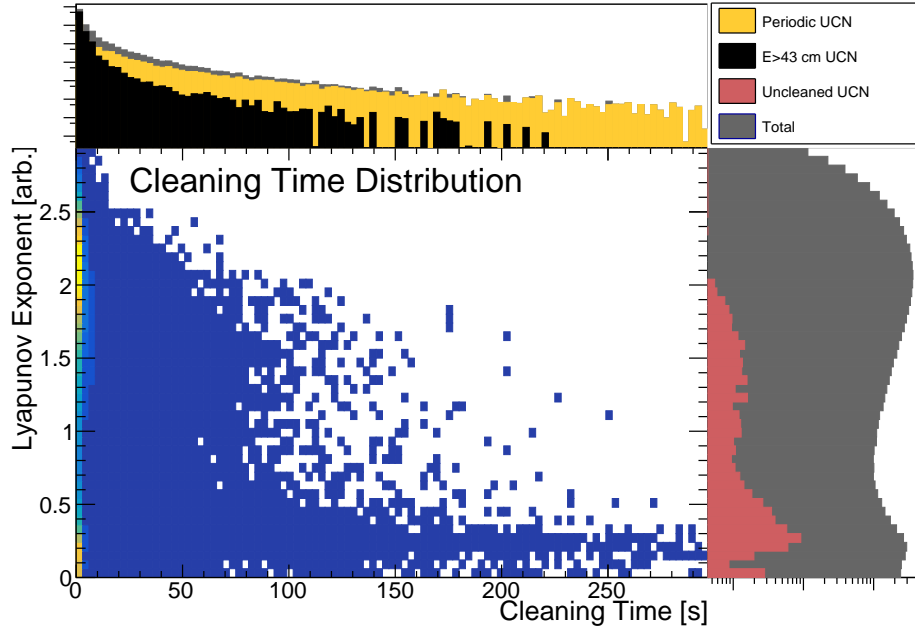


Figure 20.2: 2D Histogram of Cleaning Time and LCE in the trap

initial distribution. Regardless of this effect, high-energy UCN which could reach the cleaner during storage are still cleaned efficiently.

Regular trajectories are also associated with low  $\theta_0$  initial conditions as can be seen in Figure 20.3. This explains the prevalence of structure in the cleaner arrival positions found in Section 18.5.

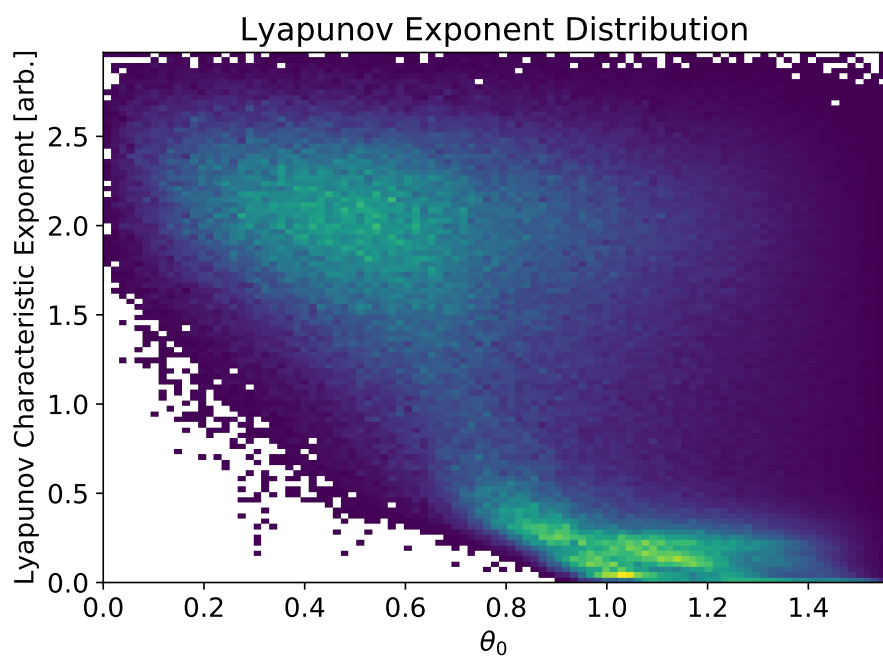


Figure 20.3: 2D Histogram of LCE and  $\theta_0$  inside the trap for  $E > 38$  cm

## CHAPTER 21

### SUPERCONDUCTING UCN TRAPS

#### 21.1 SUPERCONDUCTING TRAP GEOMETRY

LCE can be used to study new superconducting traps. Simple geometries will be used to determine whether a superconducting trap can be made where the cleanable orbits are overwhelmingly chaotic. The basic building blocks of these traps will be superconducting loops which can be solved analytically. The field of a superconducting ring in cylindrical coordinates is given by [62]

$$\begin{aligned} B_z &= \frac{c}{2\alpha^2\beta}((a^2 - r^2 - z^2)E(k) + \alpha^2 K(k)) \\ B_r &= \frac{cz}{2\alpha^2\beta r}((a^2 - r^2 - z^2)E(k) - \alpha^2 K(k)), \end{aligned} \tag{21.1}$$

where  $c$  is the current strength,  $a$  is the loop radius,  $\alpha^2 = (a - r)^2 + z^2$ ,  $\beta = \sqrt{a^2 + r^2 + z^2 + 2ar}$ ,  $k = 1 - \alpha^2/\beta^2$ ,  $E(k)$  is the complete elliptic integral of the 2nd kind and  $K(k)$  is the complete elliptic integral of the 1st kind. The derivatives are given in the technical report from Simpson *et. al.* [62] and are not reproduced here. The elliptic integrals are computed using the arithmetic geometric mean method [63].

The basic structure of the traps studied are large tori where superconducting rings share the toroidal axis of rotation. The minor radius  $r$  was allowed to change by varying the number of coils but keeping their spacing approximately 15 cm apart. The major radius  $R$  was fixed at 1 m. Additionally, a toroidal holding field was added with strength 2 kG at the center of the torus. UCN are filled up  $\frac{3}{4}$  of the height of the trap. The field strength was varied until escape at the bottom

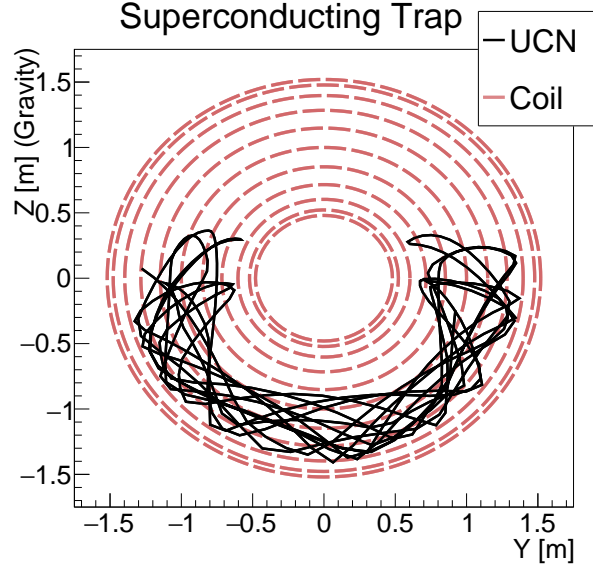


Figure 21.1: Drawing of superconducting trap with UCN trajectory. 22 coils;  $r = 0.525$  m

of the trap was not possible for UCN of energy  $\frac{3}{4}$  trap height. This corresponds to a trapping strength of approximately 150 neV. The geometry can be seen in Figure 21.1.

No feasibility studies were done on the trap geometries. The current strengths/densities in the superconductors, the holding field, and the experimental apparatus were never considered. The aim of this study is to demonstrate that a trap of this type is possible, not that a given realizable trap design will perform well.

The same symplectic integrator used in Section 16.1 was used to integrate the UCN trajectories inside the trap. Qualitatively, the behavior was similar, however the trajectories were not subject to the long-term drift seen in the UCN $\tau$  field expansion.

Trajectories were created at a single energy at the cleaning height. The phase space distribution was filled uniformly by rejection sampling on the available phase space in the momentum shell for each trajectory. This was accomplished by rejecting on  $p^2/(p_{\max}^2)$ .

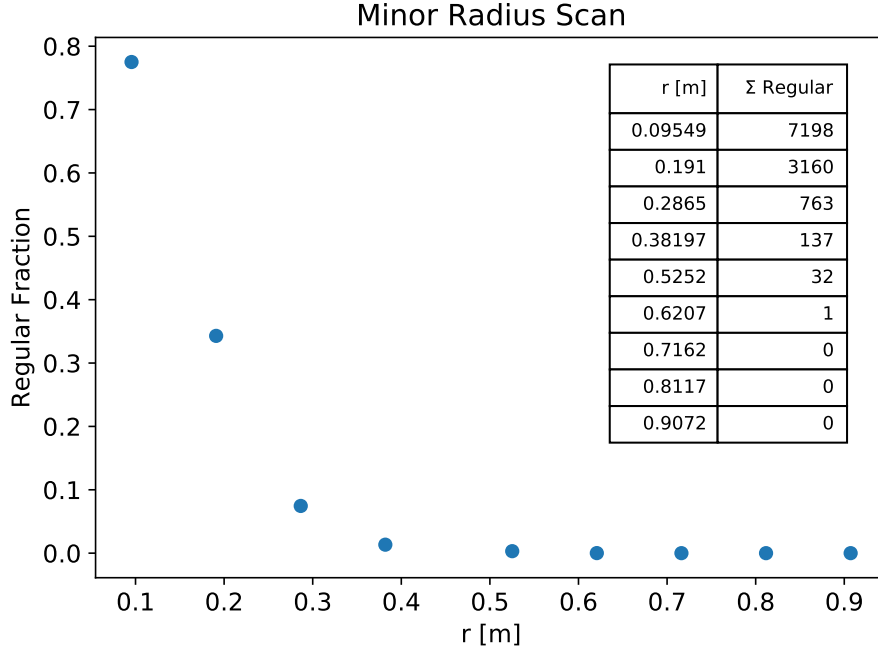


Figure 21.2: Scan of regular fraction as a function of  $r$

## 21.2 SUPERCONDUCTING TRAP RESULTS

A scan over the trap parameters  $N_{\text{wires}}, r, R$  was conducted to identify which traps had the fewest periodic orbits. The results of a fine scan over a wide range of minor radii at  $R=1$  m can be seen in Figure 21.2.

The regular fraction tends to be lower at higher  $r$ . At above  $r = 62.07$  cm, the fraction is 0 (out of 10240 trajectories). The near-chaotic region was explored with varying  $R$  as well. The ratio of minor to major radius ( $r/R$ ) is the important size parameter. The results can be seen in Figure 21.3. The chaotic nature of the trap is most important in  $r/R$  and less important in  $N_{\text{wires}}$ .

The cleaning time can also be measured. This is a quicker computation; only tens of seconds of tracking is needed per UCN instead of the hundreds for the LCE measurement. The cleaner was set at 90% of the trappable energy and was assumed to cover the entire trap surface. A neutron is considered cleaned when it rose above the cleaning height; the cleaning time for each UCN was recorded. For a highly chaotic configuration ( $r = 81.17$  cm), the cleaning time can be found in





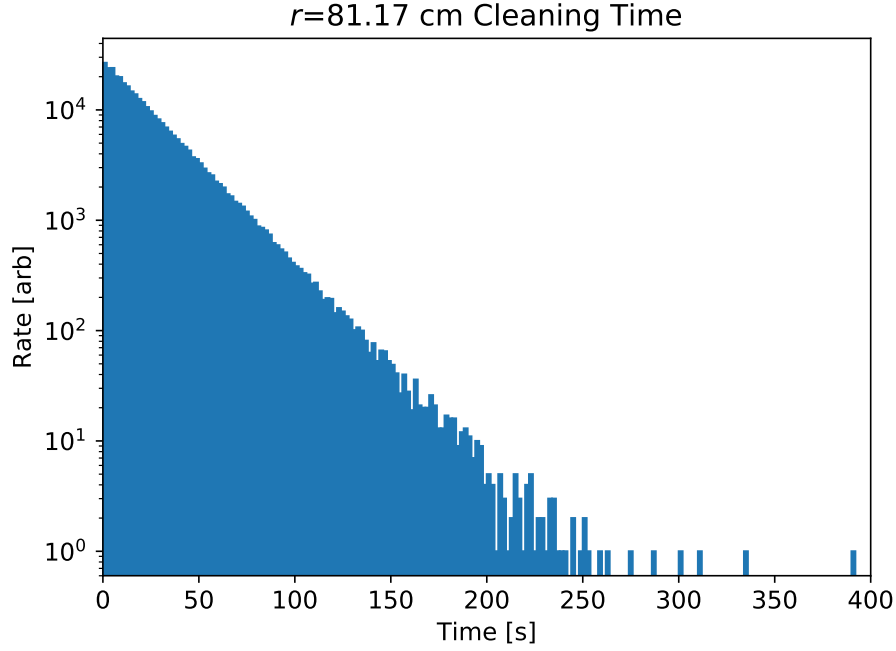


Figure 21.4: Cleaning time of  $r = 81.17$  cm trap.

where  $\rho' < r$  indicates a point inside of the torus.

The distribution of  $\rho'$  can be seen in Figure 21.5. The trap walls are evident at 15 cm. Some high-energy UCN are still near the walls of the trap, but most UCN are either inside or outside of the volume. For the UCN inside the trap, the energy gain during ramping was between 10-25 neV with an average of 17 neV. The trapping potential was approximately 150 neV; UCN did not gain so much energy that they were driven out of trapping energy. However, any cleaning procedure needs to account for this heating of UCN during ramping.

After ramping, 5% of UCN were inside the torus. The torus is approximately 10% of the volume of the containing box, so no large losses occurred during trapping. The fiducial volume of the torus is smaller due to the large field near the coils, so 5% is consistent with high-efficiency trapping during ramping.

A simple toroidal trap with overwhelmingly chaotic behavior is possible. In these simulations, traps which have a large minor radius tend to perform better. Additionally, the cleaning behavior

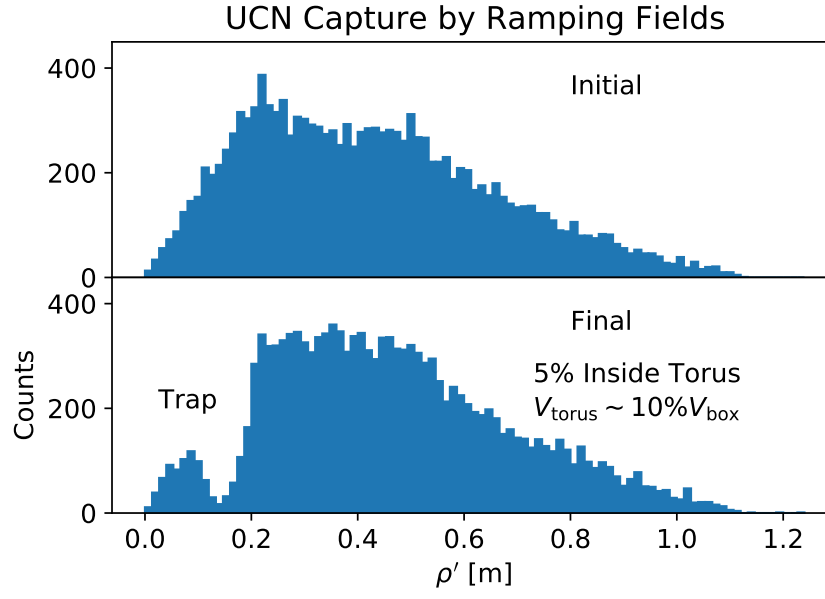


Figure 21.5: Ramping study of a superconducting UCN trap. Ramping occurred over 30 s

is seen to be exponential as expected from ergodic trajectories, and roughly comparable to the cleaning performance of UCN $\tau$ . There is not a fundamental problem with superconducting traps with respect to cleaning UCN trajectories in a lifetime experiment.

## CHAPTER 22

## CONCLUSION

### 22.1 SUMMARY OF METHODS AND RESULTS

The neutron Lifetime has implications from cosmology to beyond the Standard Model physics. The recent history of  $\tau_n$  measurements is in tension. UCN $\tau$  is a neutron lifetime experiment using trapped ultracold neutrons; it is subject to different systematics than other lifetime experiments and serves as an important check on the field. UCN $\tau$  can make a measurement with no corrections (other than background) larger than the statistical uncertainty. It does this by using a large-area spectral cleaner which rapidly eliminates overthreshold UCN, trapping neutrons with a magnetic field which avoids upscattering losses, and measuring UCN with a *in situ* detector which allows for prompt detection and spectral monitoring.

A dataset with a statistical uncertainty of 0.7 s was taken in 2016-2017. This data was analyzed to extract  $\tau_n$  by summing the neutron population at 2 separate holding times and forming  $\tau_n$  for each pair of long and short runs. Two separate analysis schemes were presented - one which relies on identifying distinct UCN events (which suffers from large pileup and deadtime corrections) and one which integrates the total light level of the scintillating detector (which suffers from large background corrections). The properties of the UCN identification algorithm were studied and a set of optimal cuts identified. The two analyses agreed within their uncertainty.

Data-driven estimates of systematic effects were made. Limits were placed on shifts due to depolarization during holding, position-dependent backgrounds, phase space evolution, and dead-

time. The size of these effects was estimated to be small ( $< 0.2$  s).

A simulation of the UCN $\tau$  experiment was constructed. A spectral and detector model was constructed using 5 free parameters and tuned on a large dataset. This model was used to estimate the effects of heating and cleaning. Heating was added by inserting vibrational profiles measured on the apparatus. The simulations estimate the combined effect of uncleaned and heated UCN is  $\sim 0.03$  s. Adjusting the vibration amplitude to 4000% of observations caused the combined effect to be  $\sim 0.15$  s. However, simulations of measuring the high-energy population of UCN in the trap show that UCN $\tau$  may not be able to directly detect uncleaned or heated UCN with sufficient precision.

Lyapunov exponents were used to characterize UCN traps. UCN traps made of superconducting loops arranged in a torus were studied for their feasibility as a neutron lifetime experiment. Trap geometry was optimized so that chaotic orbits were almost all of the orbits present. Chaotic orbits guarantee cleaning because their trajectories are ergodic. The cleaning time in such a trap was studied and shown to be acceptably fast. Additionally, the method of filling an exterior volume with UCN and ramping the superconducting coils in the trap was studied. The fraction of UCN in the trapped volume after ramping was approximately the fraction of the volume of the trap to the volume of the container. UCN were heated by approximately 17 neV during the ramping which should not be catastrophic to loading the trap.

UCN $\tau$  has made a measurement of  $877.9 \pm 0.68$  s(stat.) $\pm 0.3$  s(sys.). No systematic effects larger than the statistical uncertainty were identified and especially none which can explain the beam-bottle discrepancy. Simulations show that UCN $\tau$  (or another magneto-gravitational experiment like it) can reach a precision of 0.1 s or better in the future.

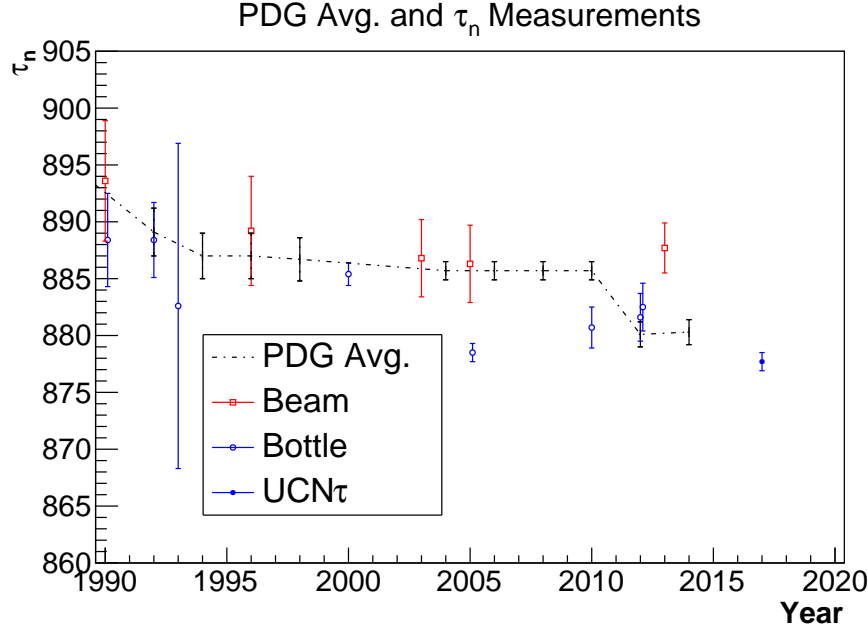


Figure 22.1: Lifetime Measurements through the ages.

## 22.2 IMPLICATIONS OF UCN $\tau$ RESULTS FOR PRECISION $\beta$ DECAY MEASUREMENTS

The measurement from UCN $\tau$  confirms the previous bottle measurements, while making no corrections (other than backgrounds) larger than the statistical uncertainty. The previous bottle measurements can be seen in Figure 22.1; UCN $\tau$  is the last measurement shown.

UCN $\tau$  is a novel lifetime experiment because of its small corrections. The use of magnetic fields to trap UCN eliminates the largest correction of previous experiments. To reiterate the estimated upper limit of the corrections, pairing runs causes the spectral variation from the source to only affect the lifetime by 0.2 s. The magnetic field configuration provides an environment largely free from depolarization, giving an upper limit of  $0.17 \pm 0.15$  s. The use of *in situ* detectors allows for the checking of phase space evolution to be performed, which is seen to be  $< 0.1$  s (under the assumption of uniform detector efficiency). Simulations of the cleaning estimate an upper limit of 0.05 s when accounting for an only 50% efficient cleaner. Nominal simulations of microphonic vibrations show no significant effect; shifts of  $> 0.1$  s occur only when the amplitude is increased to

40 times the *in situ* measured amplitudes. With these estimates, the trap operates in a relatively safe space with room for error.

Shifts large enough to explain the discrepancy between beam and bottle measurements are significantly larger than the upper limits estimated in this work. The discrepancy lies at 10 s currently, and bringing the UCN $\tau$  results within  $3\sigma$  of the beam result would require a shift of 4 s. The only systematic capable of producing shifts that large is heating at an amplitude of  $> 40 \mu\text{m}$ .

Confirmation of the bottle lifetime measurement is not yet significant in comparison of BBN helium abundances to observational values. The central value of the beam lifetime shifts the predicted  $Y_p$  at the  $+1\sigma$  bound of the currently most precise observations [16]. However, future more precise observations could shed light on this discrepancy.

Modern precision measurements of nuclear  $\beta$  decay and neutron decay can discriminate between the beam and bottle measurements however. The lower bottle lifetime and modern precision  $\beta$  decay measurements form a consistent picture in terms of  $V_{ud}$  and  $\lambda$  [64]. Figure 22.2 shows the current state of the precision  $\beta$  decay measurement field. The  $\lambda$  result from Brown *et. al.* and the  $\tau_n$  measurements from Pattie *et. al.* were blinded, reducing the possibility of biasing the results towards artificial consistency. If the modern  $\lambda$  measurements are accepted at face value, beam  $\tau_n$  measurements are an outlier at  $\sim 3\sigma$ .

Overall there remains significant unexplained tension in the neutron  $\beta$  decay field. However, using modern blinded neutron  $\beta$  decay measurements yields a consistent picture of the standard model.

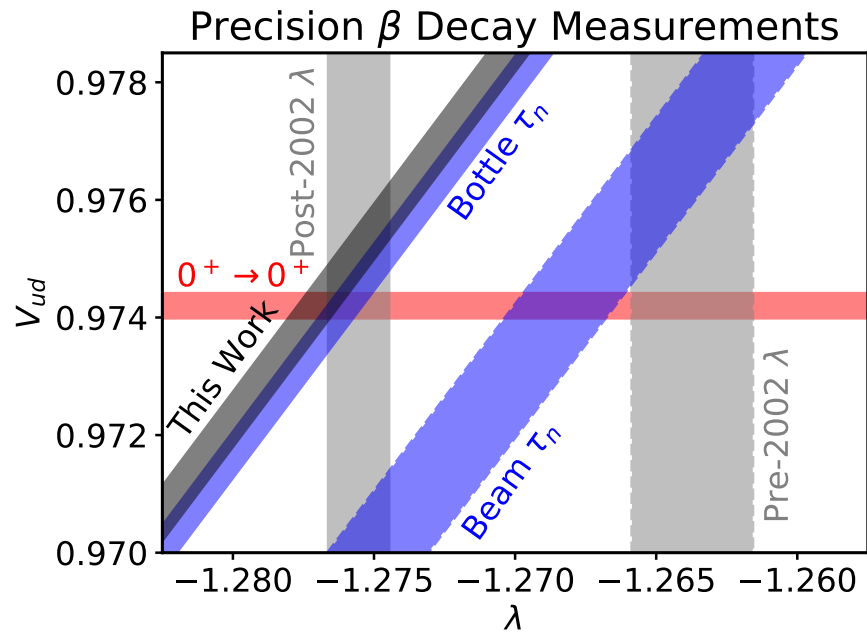


Figure 22.2: Current status of precision  $\beta$  decay measurement field showing data from nuclear  $\beta$  decay, free neutron lifetime, and neutron decay correlations.

## BIBLIOGRAPHY

- [1] C. Stewart, V. Welch, B. Plale, *et al.* *The Indiana University Pervasive Technology Institute*. Technical report, Indiana University Pervasive Technology Institute, 2017. URL <http://dx.doi.org/10.5967/K8G44NGB>.
- [2] J. Chadwick. *Nature*, 129, 1932. URL <http://dx.doi.org/10.1038/129312a0>.
- [3] H. Snell and L. C. Miller. *Phys. Rev.*, 74 p. 1217, 1948. URL <http://dx.doi.org/10.1103/PhysRev.74.1201>.
- [4] M. Tanabashi, K. Hagiwara, K. Hikasa, *et al.* *Physical Review D*, 98, 2018. URL <http://pdg.lbl.gov>.
- [5] A. Serebrov, V. Varlamov, A. Kharitonov, *et al.* *Physics Letters B*, 605(1) pp. 72 – 78, 2005. ISSN 0370-2693. URL <http://dx.doi.org/10.1016/j.physletb.2004.11.013>.
- [6] S. Arzumanov, L. Bondarenko, S. Chernyavsky, *et al.* *Physics Letters B*, 745 pp. 79 – 89, 2015. ISSN 0370-2693. URL <http://dx.doi.org/10.1016/j.physletb.2015.04.021>.
- [7] A. Steyerl, J. M. Pendlebury, C. Kaufman, *et al.* *Phys. Rev. C*, 85 p. 065503, 2012. URL <http://dx.doi.org/10.1103/PhysRevC.85.065503>.
- [8] A. Pichlmaier, V. Varlamov, K. Schreckenbach, *et al.* *Physics Letters B*, 693(3) pp. 221 – 226, 2010. ISSN 0370-2693. URL <http://dx.doi.org/10.1016/j.physletb.2010.08.032>.
- [9] A. T. Yue, M. S. Dewey, D. M. Gilliam, *et al.* *Phys. Rev. Lett.*, 111 p. 222501, 2013. URL <http://dx.doi.org/10.1103/PhysRevLett.111.222501>.
- [10] J. Byrne, P. G. Dawber, C. G. Habeck, *et al.* *EPL (Europhysics Letters)*, 33(3) p. 187, 1996. URL <http://stacks.iop.org/0295-5075/33/i=3/a=187>.



- [11] A. Serebrov, V. Varlamov, A. Kharitonov, *et al.* *Measurement of the neutron lifetime using a gravitational trap and a low-temperature Fomblin coating*. Technical report, Petersburg Nuclear Physics Institute, 2004. URL <https://arxiv.org/abs/nuc1-ex/0408009>. ArXiv:nuc1-ex/0408009.
- [12] J. S. Nico, M. S. Dewey, D. M. Gilliam, *et al.* *Phys. Rev. C*, 71 p. 055502, 2005. URL <http://dx.doi.org/10.1103/PhysRevC.71.055502>.
- [13] V. Vladimiskii. *Sov. Phys. JETP*, 12 pp. 740–746, 1961.
- [14] V. F. Ezhov, A. Z. Andreev, G. Ban, *et al.* *JETP Letters*, 107(11) pp. 671–675, 2018. ISSN 1090-6487. URL <http://dx.doi.org/10.1134/S0021364018110024>.
- [15] D. Dubbers and M. G. Schmidt. *Rev. Mod. Phys.*, 83 pp. 1111–1171, 2011. URL <http://dx.doi.org/10.1103/RevModPhys.83.1111>.
- [16] C. Pitrou, A. Coc, J.-P. Uzan, *et al.* *Physics Reports*, 2018. ISSN 0370-1573. URL <http://dx.doi.org/10.1016/j.physrep.2018.04.005>.
- [17] F. Iocco, G. Mangano, G. Miele, *et al.* *Physics Reports*, 472(1) pp. 1 – 76, 2009. ISSN 0370-1573. URL <http://dx.doi.org/10.1016/j.physrep.2009.02.002>.
- [18] M. Peimbert, V. Luridiana, and A. Peimbert. *The Astrophysical Journal*, 666(2) p. 636, 2007. URL <http://dx.doi.org/10.1086/520571>.
- [19] E. Aver, K. A. Olive, and E. D. Skillman. *Journal of Cosmology and Astroparticle Physics*, 2015(07) p. 011, 2015. URL <http://stacks.iop.org/1475-7516/2015/i=07/a=011>.
- [20] W. J. Marciano and A. Sirlin. *Phys. Rev. Lett.*, 96 p. 032002, 2006. URL <http://dx.doi.org/10.1103/PhysRevLett.96.032002>.

- [21] V. Cirigliano, S. Gardner, and B. R. Holstein. *Progress in Particle and Nuclear Physics*, 71 pp. 93 – 118, 2013. ISSN 0146-6410. URL <http://dx.doi.org/10.1016/j.ppnp.2013.03.005>.  
Fundamental Symmetries in the Era of the LHC.
- [22] I. S. Towner and J. C. Hardy. *Reports on Progress in Physics*, 73(4) p. 046301, 2010. URL <http://stacks.iop.org/0034-4885/73/i=4/a=046301>.
- [23] R. Golub. *Ultra-Cold Neutrons*. Taylor & Francis, 1991.
- [24] R. Golub and K. Böning. *Zeitschrift für Physik B Condensed Matter*, 51(2) pp. 95–98, 1983. ISSN 1431-584X. URL <http://dx.doi.org/10.1007/BF01308763>.
- [25] Z.-C. Yu, S. S. Malik, and R. Golub. *Zeitschrift für Physik B Condensed Matter*, 62(2) pp. 137–142, 1986. ISSN 1431-584X. URL <http://dx.doi.org/10.1007/BF01323423>.
- [26] Y. Pokotilovski. *Nuclear Instruments and Methods in Physics Research Section A: Accelerators, Spectrometers, Detectors and Associated Equipment*, 356(2) pp. 412 – 414, 1995. ISSN 0168-9002. URL [http://dx.doi.org/10.1016/0168-9002\(94\)01325-X](http://dx.doi.org/10.1016/0168-9002(94)01325-X).
- [27] T. M. Ito, E. R. Adamek, N. B. Callahan, *et al.* *Phys. Rev. C*, 97 p. 012501, 2018. URL <http://dx.doi.org/10.1103/PhysRevC.97.012501>.
- [28] A. Saunders, M. Makela, Y. Bagdasarova, *et al.* *Review of Scientific Instruments*, 84(1) p. 013304, 2013. URL <http://dx.doi.org/10.1063/1.4770063>.
- [29] R. Pattie, E. Adamek, T. Brenner, *et al.* *Nuclear Instruments and Methods in Physics Research Section A: Accelerators, Spectrometers, Detectors and Associated Equipment*, 872 pp. 64 – 73, 2017. ISSN 0168-9002. URL <http://dx.doi.org/10.1016/j.nima.2017.07.051>.
- [30] A. T. Holley, L. J. Broussard, J. L. Davis, *et al.* *Review of Scientific Instruments*, 83(7) p. 073505, 2012. URL <http://dx.doi.org/10.1063/1.4732822>.

- [31] R. W. Pattie, N. B. Callahan, C. Cude-Woods, *et al.* *Science*, 360(6389) pp. 627–632, 2018. ISSN 0036-8075. URL <http://dx.doi.org/10.1126/science.aan8895>. <http://science.sciencemag.org/content/360/6389/627.full.pdf>.
- [32] Z. Wang, M. Hoffbauer, C. Morris, *et al.* *Nuclear Instruments and Methods in Physics Research Section A: Accelerators, Spectrometers, Detectors and Associated Equipment*, 798 pp. 30 – 35, 2015. ISSN 0168-9002. URL <http://dx.doi.org/10.1016/j.nima.2015.07.010>.
- [33] C. L. Morris, E. R. Adamek, L. J. Broussard, *et al.* *Review of Scientific Instruments*, 88(5) p. 053508, 2017. URL <http://dx.doi.org/10.1063/1.4983578>.
- [34] V. F. Sears. *Neutron News*, 3(3) pp. 26–37, 1992. URL <http://dx.doi.org/10.1080/10448639208218770>.
- [35] Eljen Technology. *ALPHA DETECTION EJ-440, EJ-442*, 2016. URL [http://www.eljentechnology.com/images/products/data\\_sheets/EJ-440\\_EJ-442.pdf](http://www.eljentechnology.com/images/products/data_sheets/EJ-440_EJ-442.pdf).
- [36] G. F. Knoll. *Radiation Detection and Measurement*. Wiley, 4 edition, 2010.
- [37] Applied Motion Products. *ST Hardware Manual*, 2014. URL <https://www.applied-motion.com/support/manuals>.
- [38] P. A. W. Lewis and G. S. Shedler. *Naval Research Logistics Quarterly*, 26(3) pp. 403–413, 1979. URL <http://dx.doi.org/10.1002/nav.3800260304>. <https://onlinelibrary.wiley.com/doi/pdf/10.1002/nav.3800260304>.
- [39] NIST/SEMATECH. *e-Handbook of Statistical Methods*, 2013. URL <http://www.itl.nist.gov/div898/handbook/>.
- [40] R. M. Price and D. G. Bonett. *Computational Statistics & Data Analysis*, 34(3) pp. 345 – 356, 2000. ISSN 0167-9473. URL [http://dx.doi.org/10.1016/S0167-9473\(99\)00100-0](http://dx.doi.org/10.1016/S0167-9473(99)00100-0).

- [41] R. D. Cousins, K. E. Hymes, and J. Tucker. *Nuclear Instruments and Methods in Physics Research Section A: Accelerators, Spectrometers, Detectors and Associated Equipment*, 612(2) pp. 388 – 398, 2010. ISSN 0168-9002. URL <http://dx.doi.org/10.1016/j.nima.2009.10.156>.
- [42] D. G. Chapman. *Annals of the Institute of Statistical Mathematics*, 4(1) pp. 45–49, 1952.
- [43] A. Steyerl, K. K. H. Leung, C. Kaufman, *et al.* *Phys. Rev. C*, 95 p. 035502, 2017. URL <http://dx.doi.org/10.1103/PhysRevC.95.035502>.
- [44] S. J. Seestrom, E. R. Adamek, D. Barlow, *et al.* *Phys. Rev. C*, 92 p. 065501, 2015. URL <http://dx.doi.org/10.1103/PhysRevC.92.065501>.
- [45] S. J. Seestrom, E. R. Adamek, D. Barlow, *et al.* *Phys. Rev. C*, 95 p. 015501, 2017. URL <http://dx.doi.org/10.1103/PhysRevC.95.015501>.
- [46] V. Luschikov and Y. Taran. *Nuclear Instruments and Methods in Physics Research Section A: Accelerators, Spectrometers, Detectors and Associated Equipment*, 228(1) pp. 159 – 160, 1984. ISSN 0168-9002. URL [http://dx.doi.org/10.1016/0168-9002\(84\)90025-1](http://dx.doi.org/10.1016/0168-9002(84)90025-1).
- [47] C. M. Grinstead and J. L. Snell. *Introduction to Probability*. American Mathematical Society, 2003.
- [48] P. Walstrom, J. Bowman, S. Penttila, *et al.* *Nuclear Instruments and Methods in Physics Research Section A: Accelerators, Spectrometers, Detectors and Associated Equipment*, 599(1) pp. 82 – 92, 2009. ISSN 0168-9002. URL <http://dx.doi.org/10.1016/j.nima.2008.11.010>.
- [49] P. J. Channell and C. Scovel. *Nonlinearity*, 3(2) p. 231, 1990. URL <http://stacks.iop.org/0951-7715/3/i=2/a=001>.
- [50] J. Candy and W. Rozmus. *Journal of Computational Physics*, 92(1) pp. 230 – 256, 1991. ISSN 0021-9991. URL [http://dx.doi.org/10.1016/0021-9991\(91\)90299-Z](http://dx.doi.org/10.1016/0021-9991(91)90299-Z).

- [51] E. Forest and R. D. Ruth. *Physica D: Nonlinear Phenomena*, 43(1) pp. 105 – 117, 1990. ISSN 0167-2789. URL [http://dx.doi.org/10.1016/0167-2789\(90\)90019-L](http://dx.doi.org/10.1016/0167-2789(90)90019-L).
- [52] R. I. McLachlan and P. Atela. *Nonlinearity*, 5(2) p. 541, 1992. URL <http://dx.doi.org/10.1088/0951-7715/5/2/011>.
- [53] H. Yoshida. *Physics Letters A*, 150(5) pp. 262 – 268, 1990. ISSN 0375-9601. URL [http://dx.doi.org/10.1016/0375-9601\(90\)90092-3](http://dx.doi.org/10.1016/0375-9601(90)90092-3).
- [54] E. Hairer, C. Lubich, and G. Wanner. *Geometric Numerical Integration*. Springer, 2 edition, 2006.
- [55] K. J. Coakley, J. Doyle, S. Dzhosyuk, *et al.* *Journal of Research of the National Institute of Standards and Technology*, 110(4) p. 367, 2005.
- [56] N. D. Gagunashvili. *ArXiv Physics e-prints*, 2006. URL <https://arxiv.org/abs/physics/0605123>.
- [57] N. Hansen, S. Muller, and P. Koumoutsakos. *Evolutionary Computation*, 11(1) pp. 1–18, 2003. Code obtained from <https://www.lri.fr/~hansen/cmaesintro.html>.
- [58] E. I. Sharapov, C. L. Morris, M. Makela, *et al.* *Phys. Rev. C*, 88 p. 037601, 2013. URL <http://dx.doi.org/10.1103/PhysRevC.88.037601>.
- [59] S. Tomsovic and A. Lakshminarayan. *Phys. Rev. E*, 76 p. 036207, 2007. URL <http://dx.doi.org/10.1103/PhysRevE.76.036207>.
- [60] S. Materne, R. Picker, I. Altarev, *et al.* *Nuclear Instruments and Methods in Physics Research Section A: Accelerators, Spectrometers, Detectors and Associated Equipment*, 611(2) pp. 176 – 180, 2009. ISSN 0168-9002. URL <http://dx.doi.org/10.1016/j.nima.2009.07.055>. Particle Physics with Slow Neutrons.

- [61] G. Benettin, L. Galgani, and J.-M. Strelcyn. *Phys. Rev. A*, 14 pp. 2338–2345, 1976. URL <http://dx.doi.org/10.1103/PhysRevA.14.2338>.
- [62] J. C. Simpson, J. E. Lane, C. D. Immer, *et al.* *Simple analytic expressions for the magnetic field of a circular current loop*. Technical report, NASA, 2001. URL <https://ntrs.nasa.gov/search.jsp?R=20140002333>.
- [63] G. Almkvist and B. Berndt. *The American Mathematical Monthly*, 95(7) pp. 585–608, 1988. ISSN 00029890, 19300972. URL <http://dx.doi.org/10.2307/2323302>.
- [64] M. A.-P. Brown, E. B. Dees, E. Adamek, *et al.* *Phys. Rev. C*, 97 p. 035505, 2018. URL <http://dx.doi.org/10.1103/PhysRevC.97.035505>.
- [65] JCGM Working Group 1. *Evaluation of measurement data Supplement 1 to the Guide to the expression of uncertainty in measurement Propagation of distributions using a Monte Carlo method*. Technical report, Bureau International des Poids et Mesures, 2008. URL <https://www.bipm.org/en/publications/guides/gum.html>.
- [66] D. J. Salvat. *A Magneto-Gravitational Neutron Trap for the Measurement Of The Neutron Lifetime*. Ph.D. thesis, Indiana University, 2015.

## APPENDIX A

### UNCLEANED AND HEATED UCN EXTRAPOLATION

#### A.1 UNCLEANED UCN CORRECTION

The *in situ* UCN detector allows measurement of UCN population at different spectral heights. By inserting the detector only partially to a height  $h$ , only UCN with an energy of  $E(h) \simeq h \times 1 \frac{\text{neV}}{\text{cm}}$  can reach the detector and be counted. This allows for a measurement of UCN at energies above the cleaning height from either insufficient cleaning or heating

When there is insufficient cleaning, UCN can escape the trap on similar timescales to  $\tau_n$ . This is a competing loss mechanism that lowers the measured lifetime. If the UCN signal from above the cleaning height can be subtracted, then uncleaned UCN can be corrected for.

Figure A.1 shows the correction schematically. The time constant,  $\kappa_{\text{count}}$  was measured from dedicated runs in a single cleaning condition where the detector was left in place at the cleaning height for hundreds of seconds. This signal is called the "first peak" or P1. The runs were fit to a single exponential (there is both short and long time behavior, but insufficient statistics to do a detailed fit).  $\kappa_{\text{count}}$  was measured to be  $180 \pm 50$  s. No other cleaning condition was measured this way, so the time constant is assumed to not change significantly and to be the same between long and short runs.

If UCN are present in the first peak where they could have been lost, the total number of UCN predicted needs to be subtracted in order to measure the neutron lifetime. The rate seen in the detector ( $\kappa_{\text{obs}}^{-1} = R_{\text{obs}}$ ) is a combination of the counting rate ( $\kappa_{\text{count}}^{-1}$ ) and the neutron lifetime

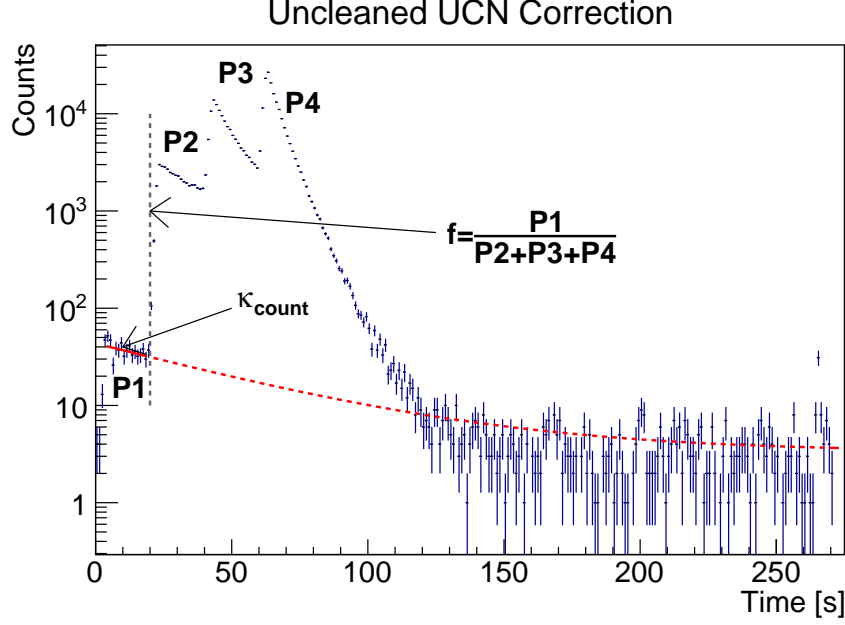


Figure A.1: Diagram of uncleaned UCN correction. The red curve is what the counting curve would look like if the detector had been left at the cleaning height until all UCN were counted. The area under the red curve (minus the background) needs to be subtracted from the sum in the subsequent peaks to make the correction.

( $\tau_n^{-1} = R_\beta$ ). The number of UCN counted in any given interval should then be

$$\begin{aligned}
 N_{\text{obs}} &= \frac{R_{\text{drain}}}{R_{\text{drain}} + R_\beta} \times N_{\text{total}} \\
 R_{\text{drain}} &= R_{\text{obs}} - R_\beta \\
 N_{\text{total}} &= N_{\text{obs}} \times \frac{R_{\text{obs}}}{R_{\text{obs}} - R_\beta}
 \end{aligned} \tag{A.1}$$

The fraction of UCN at the cleaning height (P1) over the fraction at subsequent heights (P2, P3, and P4) is measured for each cleaning condition and for short and long runs separately. UCN are lost at high energies so  $f$  depends on holding time. The P1 counting curve needs to be extrapolated out to infinity, corrected for  $\beta$  decay and subtracted. Given a number of counts observed in the first  $T_1$  s of the P1 counting curve, the expected number of UCN in the remaining part of the tail



Run Set	$f_s$	$f_t$
300s Clean 4 Dip NoGC AC DC	$0.00272 \pm 0.00009$	$0.0014 \pm 0.0002$
100s Clean 4 Dip GC AC NoDC	$0.00212 \pm 0.00008$	$0.0011 \pm 0.0002$
200s Clean 4 Dip GC AC NoDC	$0.00173 \pm 0.00008$	$0.0012 \pm 0.0002$

Table A.1: Measured uncleaned UCN fraction for cleaning conditions where the uncleaned UCN correction is needed. Note that the fraction above the cleaning height is lower for long runs.

is given by:

$$\begin{aligned}
N_{\text{uncleaned}} &= \int_{T_1}^{\infty} N_0 \exp(-t/\kappa) dt = \kappa N_0 \exp(-T_1/\kappa) \\
N_{P1} &= f \times N_{P2,P3,P4} = \int_0^{T_1} N_0 \exp(-t/\kappa) dt = \kappa N_0 (1 - \exp(-T_1/\kappa)) \\
N_{\text{uncleaned}} &= f \times N_{P2,P3,P4} \frac{\exp(-T_1/\kappa)}{1 - \exp(-T_1/\kappa)} \\
N_{\text{uncleaned,total}} &= N_{\text{uncleaned}} \times \frac{1/\kappa}{1/\kappa - 1/\tau_n} \tag{A.2}
\end{aligned}$$

During analysis of the 2015-2016 data that had insufficient cleaning,  $N_{\text{uncleaned}}$  is subtracted from the sum of P2-P4 and the corrected sum is used for the lifetime calculation. This is expected to correct for uncleaned UCN but due to uncertainty in time constant, this data was not used to report a central value. Data with the cleaning correction was used purely as a cross-check.

## A.2 UNCLENED UCN UNCERTAINTY ESTIMATE

The data taken in 2016-2017 had a significantly larger cleaner which was very effective at removing high-energy UCN. The population at the cleaning height was observed to be consistent with zero as seen in Figure A.2. All multi-step runs in 2016-2017 had a cleaning check step where the UCN population was measured at the cleaning height.

The background was subtracted by adjusting background rates observed during the holding time for height-dependence. The position dependence was determined using a set of 9-step background

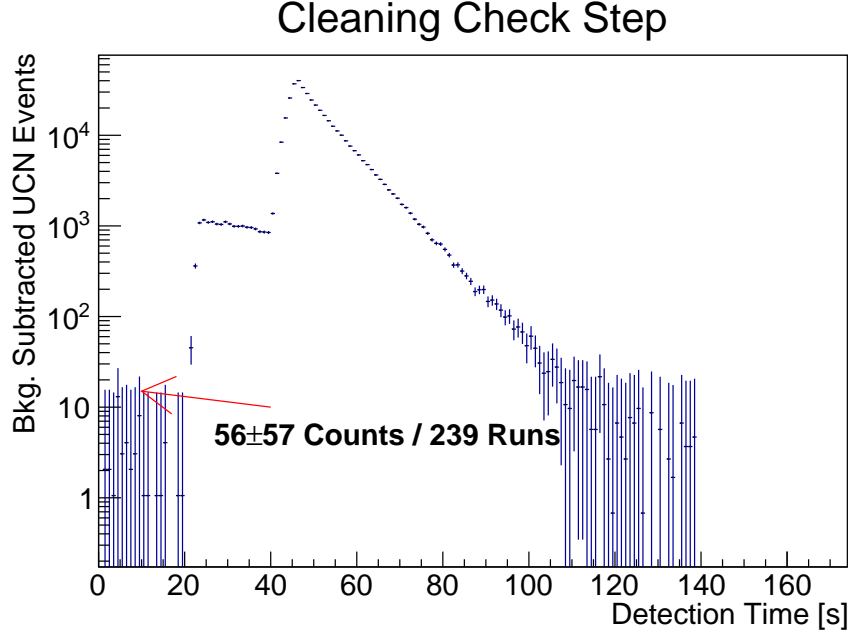


Figure A.2: Arrival time histogram for short storage time runs. The first 20s is the detector at 380 mm, at the cleaning height.

runs. The background at 9 different heights in the trap was measured and this was fit to a linear function. Insufficient high-quality background runs caused the position-dependent effect to be measured only once for the 2016-2017 data set.

For 2016-2017, the number of counts was observed to be consistent with  $56 \pm 57$  counts out of 239 runs with cleaning check steps.

A Monte Carlo technique is used to estimate the systematic uncertainty associated with these counts [65]. First the total number of foreground counts is modeled as a Poisson distributed number with expected value equal to the observed sum. The total background observed for both the production and position-dependent parts are modeled the same way. Independent foreground and background counts are randomly generated. Then the background is subtracted from the signal to generate a sample of uncleaned UCN.

The same correction used in 2015-2016 was used with each sampled uncleaned UCN density. For each sample, a total population is extrapolated and the same total population is used in a separate

analysis to generate a lifetime. The uncleaned fraction is subtracted from the short run and that population is assumed to disappear during storage, corresponding to the worst case scenario. The uncertainty is then the endpoints of the 68% coverage interval of the resulting  $\tau$  distribution.

The effect associated with uncleaned UCN was found to be  $+0.07 \pm 0.07$  s.

### A.3 HEATED UCN UNCERTAINTY ESTIMATE

A similar calculation can be made by observing counts at cleaning height for long storage runs. Heating from vibration of the trap is expected to produce a continuous increase in the UCN spectrum [66]. Further simulations in a 3D trap model also showed similar results. These simulations are detailed in Section 18.4. A lack of UCN measured at the cleaning height is evidence for lack of significant vibrational heating of UCN during storage.

For 2016-2017, the number of counts was observed to be consistent with  $51 \pm 57$  counts out of 239 runs with cleaning check steps. Figure A.3 shows the distribution of heated UCN assumed for propagating the uncertainty.

Each sample of total heated UCN population is corrected using the 2015-2016 method. However, in this case the total number of expected UCN in the first peak is added to the signal in the long runs. This corresponds to the worst case scenario where initially the heated population is trappable but the heated population is entirely lost during storage.

The effect associated with vibrationally heated UCN was found to be  $+0.27 \pm 0.3$  s. Figure A.4 shows the resultant distribution in  $\tau$  when the distribution from Figure A.3 is used.

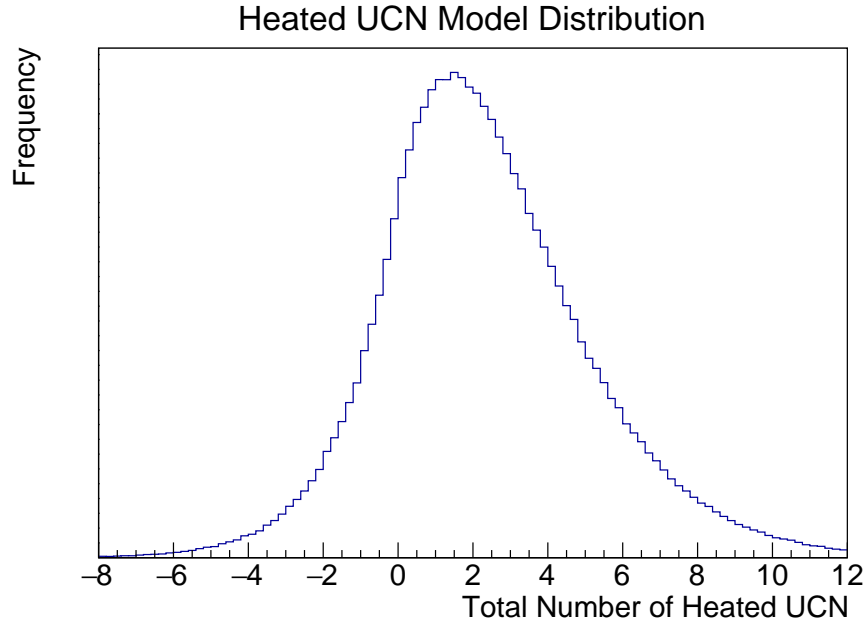


Figure A.3: Distribution of heated UCN. Foreground and background counts were randomly generated using Poisson statistics.

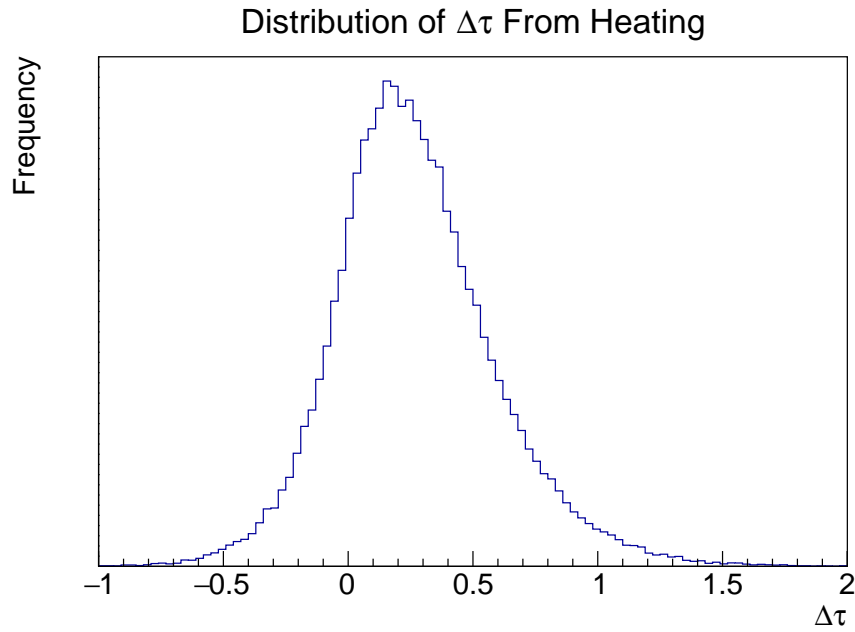


Figure A.4: Distribution of  $\tau$ . Each sample from Figure A.3 was used to calculate a  $\tau$  value to build this distribution.

# Nathan B. Callahan

---

## CONTACT INFORMATION

*Email:* nbcallah@indiana.edu

## PERSONAL STATEMENT

I am an experimental nuclear physicist at Indiana University specializing in data analysis, Monte Carlo simulations, and experimental hardware in high precision measurements. My career goal is to attain a research position focusing on analysis of precision experiments testing the Standard Model and Cosmology.

## EDUCATION

<b>Ph.D., Physics</b>	Indiana University, Bloomington	Sep. 2018
Advisor: Chen-Yu Liu		
Dissertation: Measurement of the Neutron Lifetime using Trapped Ultracold Neutrons		
<b>M.S., Physics</b>	Indiana University, Bloomington	Aug. 2014
<b>B.S., Physics</b>	Purdue University	May 2012
Minor: <b>Computer Science</b>		

## EXPERIENCE

<b>Nuclear Physics Ph.D.</b> , Indiana University/Los Alamos National Laboratory	2012-2018
--	-----------

### DATA ANALYSIS

- Co-lead of analysis for *Science* publication (0.1% precision measurement)
- Wrote independent analysis program in C++/Python
- Analyzed 100GB+ of raw ROOT binary data into histograms
- Wrote algorithm to identify neutron signals from raw photoelectron counts
  - Identified and corrected 0.1% systematic bias in algorithm
- Fit theoretical model to data to correct for neutron loss

### MONTÉ CARLO SIMULATIONS

- Developed simulation software using symplectic integration techniques
- Simulated full experiment (magnetic fields and detectors) to match data
- Tuned Monte Carlo model to analysis histograms with  $\chi^2$  minimization
  - Extracted detector characteristics from tuned parameters
- Used output of Monte Carlo model to predict systematic effects
- Deployed parallelized simulation on Indiana's Supercomputer

## DETECTOR DEVELOPMENT

- Investigated electron beam evaporation of  $^{10}\text{B}$  onto ZnS scintillators
- Used NIM electronics to shape and discriminate signals
- Set up Data Acquisition to measure position-dependent response of detector
- Simulated detector optics to understand position-dependence and efficiency

## EXPERIMENTAL SHIFT LEAD

- Collaborated with Los Alamos personnel and graduate students to prepare experiment
- Lead experimental shifts for majority of data taking ( $\sim 6$  months)
- Responsible for data quality, experimental operation, and run planning

## HARDWARE DEVELOPMENT

- Constructed linear actuators for UCN $\tau$  apparatus
- Developed control electronics for actuators
- Wrote software to communicate with stepper and servo motors

## **Nonlinear Dynamics Simulations**, Oak Ridge National Laboratory

2016

- Awarded Department of Energy Office of Science Graduate Student Research Grant
- Developed code for tracking neutrons inside superconducting solenoid
- Measured degree of chaos in trap using Lyapunov Exponents
- Optimized trapping geometry to obtain 100% ergodic traps
- Studied methods to fill traps with Ultracold Neutrons
- Deployed parallelized simulation on Indiana's Supercomputer

## **Condensed Matter Simulations**, University of Toledo REU

2011

- Selected for Research Experience for Undergraduates program
- Studied Brownian motion of simulated nanoparticle clusters to measure diffusion constant
- Simulated metallic crystal lattices in Molecular Dynamics simulations
- Measured performance increase when using Temperature Accelerated Dynamics
- Deployed simulations at the Ohio Supercomputer Center

## TEACHING

**Teaching Assistant**, Indiana University

2012-2013

- Taught 3 semesters of undergraduate Laboratory courses
- One to Two sections with  $\sim 30$  students each
- Basic instruction on experiment, uncertainties, and physics
- Graded laboratory reports
- One-on-one instruction during weekly departmental help sessions

## TECHNICAL SKILLS

### ANALYSIS

<b>General:</b>	Data Reduction, Frequentist Estimation
<b>Monte Carlo:</b>	Numerical Integration, Nonhomogeneous Poisson Processes, Markov Chains
<b>Fitting:</b>	$\chi^2$ Minimization, Bayesian (MCMC)

### SOFTWARE

<b>Programming Languages:</b>	C/C++, Python, Javascript, Fortran
<b>Software Packages:</b>	ROOT, NumPy, SciPy
<b>Databases:</b>	MySQL, InfluxDB
<b>Environments:</b>	Linux, Supercomputing Systems (Portable Batch System)

### HARDWARE

<b>Detectors:</b>	Photomultipliers, Scintillation
<b>Electronics:</b>	Microcontrollers, NIM Electronics, DAQ Hardware
<b>Vacuum:</b>	Leak Checking, Construction, Residual Gas Analysis
<b>Actuators:</b>	Stepper Motors, Servo Motors, PLCs, Software

## GRANTS AND AWARDS

<b>DOE Office of Science Graduate Student Research (SCGSR) Award</b> \$18000 Stipend Awarded for Research Proposal	2016
<b>APS Group on Precision Measurement &amp; Fundamental Constants Travel Award</b>	2015

## PUBLICATIONS

2018 **N. B. Callahan**, C.-Y. Liu, F. Gonzalez et. al. **Monte Carlo Simulations of Trapped Ultracold Neutrons in the UCN $\tau$  Experiment**, in preparation for submission to *Physical Review C*. Preprint available on request.

- 2018 R. W. Pattie, **N. B. Callahan**, C. Cude-Woods et. al., **Measurement of the neutron lifetime using a magneto-gravitational trap and in situ detection**, *Science* 360, 627 (2018).
- 2018 T. M. Ito, E. R. Adamek, **N. B. Callahan** et. al., **Performance of the upgraded ultracold neutron source at Los Alamos National Laboratory and its implication for a possible neutron electric dipole moment experiment**, *Physical Review C* 97, 012501 (2018).
- 2017 R. Pattie, E. Adamek, T. Brenner et. al., **Evaluation of commercial nickelphosphorus coating for ultracold neutron guides using a pinhole bottling method**, *Nuclear Instruments and Methods in Physics Research Section A: Accelerators, Spectrometers, Detectors and Associated Equipment* 872, 64 (2017).
- 2017 C. L. Morris, E. R. Adamek, L. J. Broussard et. al., **A new method for measuring the neutron lifetime using an in situ neutron detector**, *Review of Scientific Instruments* 88, 053508 (2017).
- 2017 L. Broussard, B. Zeck, E. Adamek et. al., **Detection system for neutron decay correlations in the UCNB and Nab experiments**, *Nuclear Instruments and Methods in Physics Research Section A: Accelerators, Spectrometers, Detectors and Associated Equipment* 849, 83 (2017).
- 2017 S. J. Seestrom, E. R. Adamek, D. Barlow et. al., **Total cross sections for ultracold neutrons scattered from gases**, *Physical Review C* 95, 015501 (2017).
- 2016 Z. Tang, E. Adamek, A. Brandt et. al., **Measurement of spin-flip probabilities for ultracold neutrons interacting with nickel phosphorus coated surfaces**, *Nuclear Instruments and Methods in Physics Research Section A: Accelerators, Spectrometers, Detectors and Associated Equipment* 827, 32 (2016).
- 2015 S. J. Seestrom, E. R. Adamek, D. Barlow et. al., **Upscattering of ultracold neutrons from gases**, *Physical Review C* 92, 065501 (2015).
- 2015 Z. Wang, M. Hoffbauer, C. Morris et. al., **A multilayer surface detector for ultracold neutrons**, *Nuclear Instruments and Methods in Physics Research Section A: Accelerators, Spectrometers, Detectors and Associated Equipment* 798, 30 (2015).
- 2014 D. J. Salvat, E. R. Adamek, D. Barlow et. al., **Storage of ultracold neutrons in the magneto-gravitational trap of the UCN $\tau$  experiment**, *Physical Review C* 89, 052501 (2014).
- 2013 Y. Shim, **N. B. Callahan**, and J. G. Amar, **Localized saddle-point search and application to temperature-accelerated dynamics**, *The Journal of Chemical Physics* 138, 094101 (2013).



## PRESENTATIONS

### CONFERENCE

- 2018 (Invited 20m) **Measurement of the neutron lifetime using a magneto-gravitational trap**, Thirteenth Conference on the Intersections of Particle and Nuclear Physics, Palm Springs, California
- 2017 (Oral 12m) **Measurement of Systematic effects in the UCN tau neutron lifetime experiment**, APS Division of Nuclear Physics October Meeting, Pittsburgh, Pennsylvania
- 2016 (Oral 12m) **Overview of progress on the UCNtau Experiment**, APS Division of Nuclear Physics October Meeting, Vancouver, British Columbia
- 2015 (Oral 10m) **Developments in Ultracold Neutron Measurement for the UCN $\tau$  experiment**, APS April Meeting, Baltimore, Maryland
- 2014 (Oral 12m) **In Situ Detection of Trapped Ultracold Neutrons Using a Vanadium Foil**, APS Division of Nuclear Physics and Physical Society of Japan October Meeting, Waikoloa, Hawaii

### DEPARTMENTAL

- 2016 (Oral 1h) **Measuring the Neutron Lifetime with the UCN $\tau$  Magneto-Gravitational Trap**, ORNL Lunch Talk, Oak Ridge, Tennessee